Biochemical Reactions in Confined Space

Thesis by

Yu Liu

In Partial Fulfillment of the Requirements

for the Degree of

Doctor of Philosophy

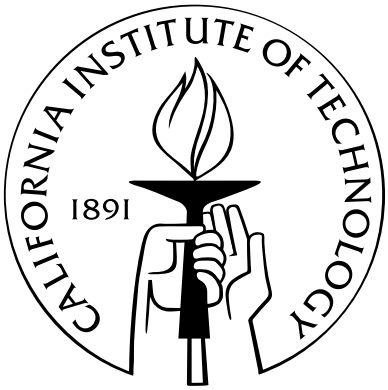

California Institute of Technology

Pasadena, California

2010

(Defended June 17, 2009)

To

Yang Fan and Liu Yun-cong

Acknowledgements

I would like to take this opportunity to thank my advisor, Dr. C. Patrick Collier, for his support during the past five years. He treated me as an equal colleague from the first day I was in his lab, which I had not expected at all. My PhD committee, composed of Drs. William A. Goddard, Jesse L. Beauchamp, and Robert B. Phillips, have been kind enough to offer tremendous help, sometimes unsolicited, along my way toward graduation. Not only was my research improved by their insightful questions posed during committee meetings, but I was fortunate enough to have conversations with them about the general practice of science as well. I will always be motivated by their devotion to science and education, which I witnessed as a student in and outside the classroom and lab.

My labmates have always been a great source of reliable help. Ian Shapiro is always ready to help me with optics. Yoshie Narui taught me how to use the stopped-flow instrument and volunteered to take a lot of public responsibility in the lab. Jason Gamba showed me the operation of the confocal microscope and cheered on the progress we made in research. Chen Jinyu generously offered me a ride the first week he moved to Pasadena, and shared his experience without reservation. Garrett Bittner was the first one I met in the group and helped me with the first thing I did—obtaining the group account. As a SURF student, Raman Shah left impeccable lab notes which saved us a lot of time when we had to reconstruct his setup later. Dr. Hyun-gil Jung showed me the first experiment I learned at Caltech and impressed me with his perseverance and industry. It was also nice talking with Dr. Maria Espandiu who never hesitated to encourage my research. Dr. Donato Ceres was kind enough to loan me his fancy Canon SLR camera for imaging experiments and was always ready to offer his opinion when I had a question. I had many pleasant conversations on various topics with Dr. Tai-hwan Ha who appeared to be in the lab all the time; he also showed me how to use the Olympus microscope. Although I did not have a lot of interaction with Dr. Jongwon

Kim, I learned the importance of being well organized from his presentation in which every literature reference was followed by an apparently universal index number. Among all the labmates, I owe the most to Dr. Seung-yong Jung. We have been working closely on the same projects, which would be impossible without his devotion of time and effort. He was always willing to share his valuable experience and increase his own workload. I wish him the best of luck in his new position and future endeavors.

My colleagues are definitely not limited to the group. I spent a considerable amount of time in the Micro–Nanofabrication Lab in Watson, managed by Alireza Ghaffari. As the master of the public facility, Ali kept it running 24/7 for researchers with a wide array of projects and backgrounds. He is the person I turn to first whenever there is a technical issue. It would take forever to list all the help I got from him. I am also grateful to the colleagues I have been working with in the facility for their kind tolerance of my mistakes and generous suggestions on my research. Heng Xin showed me the protocol of the thermal evaporator. Christina Morales and Dr. Saurabh Vyawahare shared both their reagents and protocols, helping me get started as soon as possible. Chiu Hsin-Ying and Hareem Tariq provided valuable tips for working with the e-beam writer. I also had enjoyable conversations with Cui Xiquan, Zhang Kechun, Lee Lapman, Robert X. Bao and others in the noisy environment of a clean room. I am also indebted to the Molecular Materials Resource Center, directed by Dr. Bruce S. Brunschwig, for freely using their instruments. The Beckman Imaging Center at Caltech was also essential in providing access to confocal microscopes. Additionally, the Phillips lab was willing to squeeze microscope time to give me a chance to do my experiments, which I greatly appreciate.

Caltech is a great place for graduate students. All the staff members I talked to are willing to help. Dian Buchness, Laura Howe, Agnes Tong, and Anne Penney in chemistry department provided continuous support to me from orientation to graduation. Friends in Braun House taught me how to cook decent Chinese food when I did not even know how to make steamed rice. The senior Chinese students—Pang Changlin, Ouyang Xiaoxi, Wu Jian, Zhang Chengzhong, Jin Zhipu and Shi Ling—took me out for dinner and shopping in Chinese neighborhoods every week until I got my own car, since I was not able to get used to either American or Mexican cuisine. The house representative Valarie Norton devoted her own time to set up the computer room where I could work on my code

any time I wished. I also benefited from lectures offered by various departments. Some of my TAs, including David Wu, Effrosyni Seitaridou and Liu Jian, continued to provide valuable input to my research. As a TA myself, I had the privilege to work with Drs. Douglas Rees, Vicent McKoy and Sunney Chan and was given the opportunities to practice teaching with the bright undergraduates at Caltech. Outside the classroom, I enjoyed fine dinners with Dr. McKoy and Dr. Chan, and illuminating conversations on career issues with Dr. Rees and Dr. Chan.

I was not able to spend enough time with my parents during these years, but they always support my decision. My wife, Yang Fan, and her family also understand my busy schedule. I am extremely fortunate to have Fan at my side to share all the laughter and tears. Facing a problem, she is the one sitting with me to work out a solution. With her support, I cannot imagine anything that is impossible. Fan's advisor, Dr. Pamela Björkman, and her group members were kind enough to tolerate my use of their facility.

Finally, I am dedicating this thesis to Fan and our son, who are collectively extending my horizon everyday.

Abstract

The understanding of biological systems relies on the accurate description of the interaction among biomolecules. This knowledge can be obtained by in vitro assays involving interacting partners with well-defined compositional, spatial, and temporal constraints. The distinguishing features of living systems, namely, low copy number, crowded environment, and spatial compartmentalization, are usually absent in most in vitro experiments reported in the literature. This thesis discusses the implications of low copy number and spatial constraints using theoretical and computational methods in some model systems. Furthermore, two experimental platforms, based on the recent development of microfluidic techniques, are described in detail. In the first implementation, micron-sized chambers fabricated using soft lithography provide a high-throughput reactor array whose size and composition can be configured to mimic the in vivo environment. The second design reports the generation and manipulation of femtoliter-volume water-in-oil droplets. A model biochemical reaction catalyzed by β-galactosidase is observed in both reactors with precisely defined initiation time, opening the way to monitor transient kinetics in addition to steady-state behavior. Additionally, the enzymatic activity exhibits a negative correlation with the size of water-in-oil droplets when the nominal concentrations of reagents are kept the same. This surprising result is analyzed in detail by carefully designed control experiments, and attributed to the shear-induced redistribution of surfactant employed to stabilize the water–oil interface. Specifically, smaller droplets experience bigger shear stress, which change the surface concentration of surfactant and allow for the nonspecific binding of proteins to the interface. Surface-bound enzymes are denatured, leading to reduced catalytic activity. This highly dynamic process is hardly detectable by other methods such as tensiometry or direct fluorescence imaging of the interface.

Contents

List of Figures

List of Tables

Chapter 1

Introduction

As the basis of all life phenomena, the interaction of biomolecules has been under the scrutiny of scientists and cataloged meticulously [2]. The recent advent of systems biology represents a natural development from this collection of knowledge: it is more reliable to predict the property of a biological system by taking appropriate account of all the underlying components and their interaction. Unfortunately, the knowledge, which systems biology relies on as the starting point, was usually accumulated by in vitro studies of only a small subset of the system of interest under fundamentally different conditions from its in vivo counterpart. In particular, molecules in a living cell normally find themselves in an extremely crowded environment with a small copy number and significant spatial localization.

Molecular crowding is caused by the existence of a high concentration of macromolecules. On average, each protein occupies a volume of about 10^3 nm^3 in *E. coli* [106]. This is far smaller than that in the dilute solution one would have in a typical in vitro assay. In another word, the free space associated with each macromolecule is comparable to the physical size of the molecule itself. This picture is artistically illustrated in figure 1.1. The diffusion coefficients of biomolecules in such a crowded environment are expected to be smaller than their values in a dilute solution, but the existence of concentrated solute effectively exerts an attracting potential between binding partners [122]. These two effects oppose each other in their influence on bimolecular reaction kinetics, making it difficult to predict the overall consequence of crowding.

It is also very common to find only a handful of each type of molecule in a cell [110]. For example,

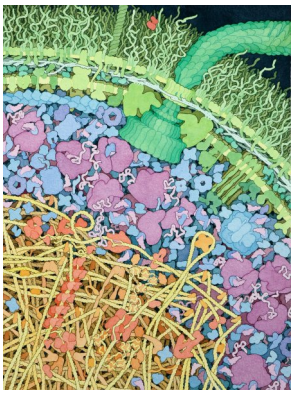

Figure 1.1. The crowded environment in an *E. coli* cell depicted by professor Goodsell (`http://mgl.scripps.edu/people/goodsell`).

there are at most two copies of genetic material and the numbers of regulators are also limited. As a result, the kinetics of chemical reactions is under the influence of stochastic noise and normally different quantitatively or even qualitatively from the prediction of law of mass action [117]. A notable example is the lysis–lysogeny switch of *E. coli*. The seemingly random choice between the two possible fates can be explained by taking into account the stochasticity of chemical reactions when the copy numbers are small (reference [6] and figure 1.2). Finally, real cells are highly compartmentalized. Chemical reactions take place with a well-defined boundary rather than in an infinite space. The boundary effect is more important when system dimension is decreased because surface-to-volume ratio inversely scales as its size. Reaction in a test tube is hardly affected by the presence of boundary, whereas spatial confinement may have important implications in the reaction kinetics in highly localized cellular environments.

Recognizing the important features of in vivo biochemical reactions, it is imperative to study the interaction among biomolecules in a cell-mimetic environment. This thesis summarizes some results of both theoretical and experimental investigations. In chapter 2, the effect of low copy number is exemplified by analyzing the dynamics of a classic chemical oscillator (section 2.1.1) and a well-known biological oscillator (section 2.1.2). In both cases, stochastic noise in chemical reactions adds significant perturbation to the system dynamics, and law of mass action is shown to be insufficient in some regime. Gillespie algorithm is used to simulate the dynamics, and the strength

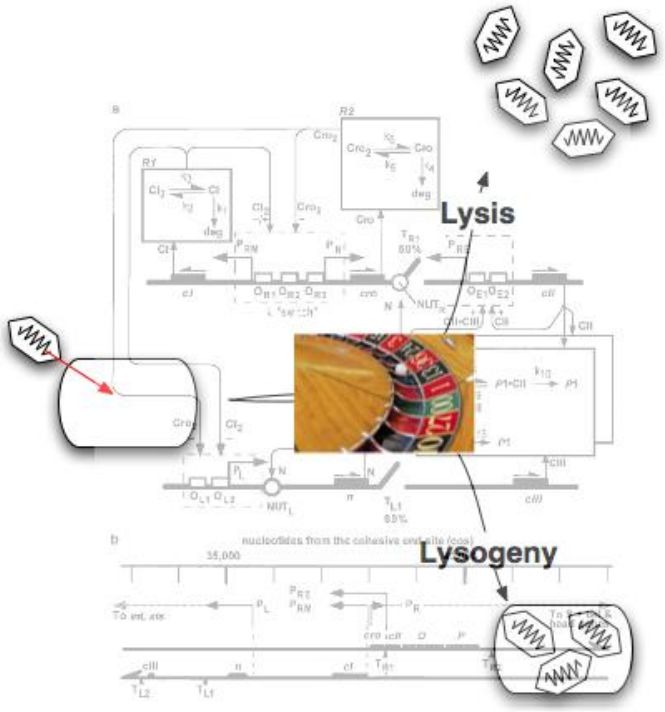

Figure 1.2. *E. coli* cells infected by phage-λ have two possible fates: lysogeny or lysis. The choice is randomly made by the inherent stochasticity of the underlying biochemical reaction network. The reaction scheme in the background is taken from reference [6].

of noise is tuned by changing system volume. In section 2.1.1, a variant of Belousov–Zhabotinsky system is shown to exhibit persistent oscillation close to the bifurcation point where deterministic simulation predicts steady-state behavior. The regularity of the oscillation, as a function of system volume, may have a maximum, indicating the existence of stochastic resonance. In section 2.1.2, the dynamical behavior of peroxidase–oxidase oscillator is investigated as a function of initial conditions. Around the bifurcation point, the system chooses its fate randomly in a way conceptually similar to the lysogeny–lysis decision process (figure 1.2). The effect of confinement is then the topic of section 2.2, which relies on scaling analysis and stochastic simulation. The spatial confinement leads to the synchronization of a group of enzymes coupled by rapid diffusion of small molecules. A more fundamental discussion of molecular diffusion in confined space follows in section 2.3 with the help

of both analytical solution and numerical simulation. Here special attention is paid to the statistical property of molecular collisions during diffusion and the clustering of these events in space and time. Methods of spatial stochastic simulation are also briefly discussed.

The development of microfluidic platforms for the investigation of biochemical reactions with configurable constraints is the subject of chapters 3 and 4. Both platforms provide convenient methods to initiate enzymatic reactions with tunable crowding and spatial confinement, a crucial requirement for simulating intracellular environment. The design of the devices also allows for experimental observation over a wide range of timescale from hundreds of milliseconds to dozens of minutes after the reaction starts. As a result, both transient and steady-state behavior are accessible using the same setup. As a proof of concept, chapter 3 reports the application in the observation of the catalytic activity of single β-Galactosidase (β-Gal) restricted in femtoliter-sized microchamber arrays. Repetitive observation of the chemical reactions in the array can be carried out in the same device to get statistically significant results. The dimension of each chamber is less than 10 μm and can be further reduced to increase throughput. Chapter 4 is based on the generation and manipulation of water-in-oil droplets with well-defined and tunable diameter smaller than 10 μm, comparable in size with cellular compartments. Details of the experimental setup to control the microfluidic device are included in this chapter. As the most important finding of this work, the history of droplet formation has a significant effect on the interfacial property of the droplets and leads to a decrease of apparent enzyme activity with decreasing droplet size. This observation is expected to motivate more discussion in microfluidic literature as devices with ever-smaller characteristic size are to be utilized.

The effort devoted to the design and optimization of these microfluidic networks also has practical significance in detecting biomolecules. Many popular detection schemes are based on the generation of fluorescent products catalyzed by the molecule to be detected [7, 74, 91, 113]. For qualitative analysis, the accumulated fluorescence signal crossing the detection threshold is used as evidence for the existence of a certain molecule. Although reducing the volume of the reactor, one of the advantages offered by microfluidics, does not change the sample concentration, the following analysis will show that under the condition of extreme dilution, the detection time may be reduced by using

microreactors. In bulk assay, the fluorescent product concentration c_{P} is expected to be proportional to the concentration c_{E} of the enzyme to be detected, or $c_{\mathrm{P}} = c_{\mathrm{E}}t/\tau_{\mathrm{E}}$ where τ_{E} is the turnover time. If a detection threshold is set to be c_0, one has to wait for at least $t_{\mathrm{bulk}} \sim c_0\tau_{\mathrm{E}}/c_{\mathrm{E}}$ to get the measurement result. In order to reduce t_{bulk} for a certain enzyme, one has to increase c_{E}. In practice, however, it is not always feasible to concentrate the sample as much as one wishes due to practical or economical reasons. This expression of t_{bulk} also seems to suggest that reducing reactor size does not accelerate the detection process. This conclusion, however, is not true when the average number of the enzyme in a reactor is fewer than one due to the reduction of volume, concentration, or both. In fact, for a reactor of volume V, when $c_{\mathrm{E}}V \ll 1$, there is at most one enzyme present and the product concentration can be written as $c_{\mathrm{P}} = t/(V\tau_{\mathrm{E}})$. The time it takes to cross the threshold c_0 is thus $t_{\mathrm{micro}} \sim c_0V\tau_{\mathrm{E}}$. It is obvious to see that reducing system volume will reduce the time consumption linearly. Of course, when the enzyme solution is diluted, one has to carry out a large number N of repeated measurements to get reliable result. Normally, one would require $Nc_{\mathrm{E}}V > 1$. If these repetitive experiments were done sequentially, the total time consumption $Nt_{\mathrm{micro}} \gg t_{\mathrm{bulk}}$, meaning that there is no benefit of system-size reduction. Fortunately microfluidic techniques provide an opportunity of large-scale parallelization [159], which makes it possible to make ensemble measurement with little added time consumption. For example, a large array of microreactors may be observed simultaneously (section 3 and references [113] and [116]). If M reactors can be fabricated in an array, the time required would be reduced by M-fold, or $t^{\mathrm{P}}_{\mathrm{micro}} \sim Nt_{\mathrm{micro}}/M$. In order for $t^{\mathrm{P}}_{\mathrm{micro}} < t_{\mathrm{bulk}}$, one has to have a large enough M such that $M > Nc_{\mathrm{E}}V$. As another example, if water-in-oil droplets are generated as in chapter 4, the enzymatic reaction is initiated once the droplet is formed, and one makes observation at a downstream location to allow for sufficient product generation if any. Because the droplets are flowing in a continuous fashion [134], the detection time is thus asymptotically proportional to the product of the number of droplets to be monitored and their generation time as $t^{\mathrm{P}}_{\mathrm{micro}} \sim Nt_{\mathrm{drop}}$ where t_{drop} is the droplet-formation time. To gain an advantage over traditional method, one just needs $t_{\mathrm{drop}} < t_{\mathrm{bulk}}/N$. Additionally, by simply counting the number of reactors showing high enough fluorescence signal, one can easily calculate the concentration of the enzyme for quantiative purpose [113]. The above analysis

establishes the practical movitation of contriving a microfluidic platform with reduced reactor size.

Finally, the thesis concludes with a summary of the lessons learned from these studies and an outline of future directions.

Chapter 2

Effects of Spatial Confinements on Biochemical Reactions

2.1 Chemical Reactions of Low Copy Number

2.1.1 System-size Resonance of a Reduced Model of Belousov–Zhabotinsky Reaction

Introduction

Belousov–Zhabotinsky (BZ) reaction is arguably the most famous example of oscillatory chemical reactions and nonlinear chemistry in general. Variants of BZ reactions are still attracting the interests of scientists even 50 years after its first publication [8]. Nonlinear phenomena may be more sensitive to the stochastic nature of chemical reactions. It is thus natural to subject BZ reactions to low copy number conditions and investigate the influence of noise on the behavior of the system. In addition, the recent development of microfluidic techniques [23] offers unprecedented access to femtoliter-sized reactors where the stochastic effect is expected to be more pronounced than in bulk conditions. This advancement enables the direct comparison between theoretical prediction and experimental observation.

Only a subset of nonlinear chemical reactions can be conveniently used in a microfluidic device for interrogation. Due to the complexity of world-to-chip integration, the content of a microreactor is

normally isolated from the environment. For example, a continuously stirred tank reactor with constant supply and removal of chemicals is not trivial to scale down to femtoliter range. This limits our choice of candidate systems to batch reactions. Furthermore, a convenient method, preferably based on an optical signal, should be available to record the kinetics of the reaction. Finally, it is extremely useful if the reaction mechanism of the reaction is known. On the basis of these consideration, we will focus on a variant of BZ reaction whose core elements are bromate and 1,4-cyclohexanedione (bromate–CHD system). It supports oscillation in bulk mode. Its reaction mechanism has been elucidated at various levels [148–151]. And optical signal, from fluorescence [150] or absorbance [42], is available to facilitate experimental observation. In addition, during the reaction CHD does not release carbon dioxide, which tends to form bubbles and disturbs the system. Figure 2.1 shows the spatial pattern formed by a bromate–CHD system in a Petri dish.

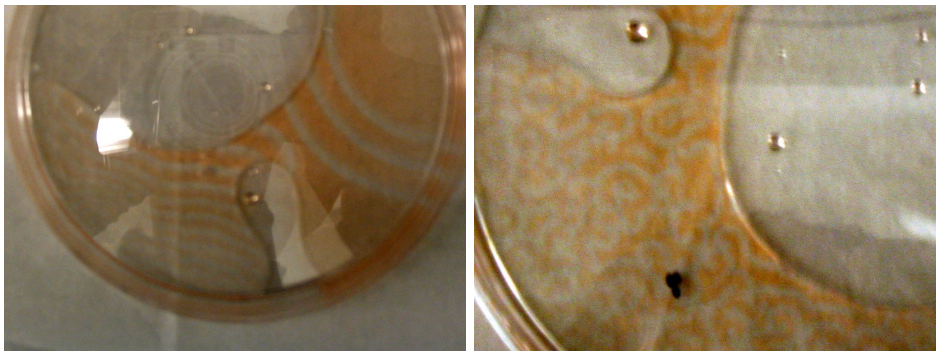

(a) (b)

Figure 2.1. Ribbon (a) and spiral (b) patterns formed by bromate–CHD system in a Petri dish. The initial concentrations were [CHD] = 0.1 M, [$KBrO_3$] = 0.1 M, and [H_2SO_4] = 1.0 M. Ferroin (0.1 mM) was used as indicator, and 0.01 M KBr was added to reduce induction time.

Bromate–CHD system was used in microfluidic channels to generate obstacle-mediated spiral waves [42–44, 90]. The same system was also the subject of a recent experiment showing the effect of stirring rate on the reaction kinetics [172]. The effect of reactor size on this system is yet to be explored in theory or experiments. In this section, we report the effect of stochastic chemical reactions on the dynamical behavior of this system by using Gillespie algorithm and a reduced model of bromate–CHD system (Table 2.1). In particular, we studied the effect of system volume when

Table 2.1. Reduced model of bromate–CHD system [149]

Reaction[a]	Reaction rate expression	Rate constant
$X + Y \rightarrow$ sink	$k_1[X][Y]$	$k_1 = 3.225 \times 10^6$ M^{-1} s^{-1}
$Y \rightarrow X$	$k_2[Y]$	$k_2 = 0.158$ s^{-1}
$2X \rightarrow$ sink	$k_3[X]^2$	$k_3 = 4.386 \times 10^3$ M^{-1} s^{-1}
$X + Z \rightarrow 2X$	$k_4[Z][X]^{1/2}$	$k_4 = 86.7$ $M^{-3/2}$ s^{-1}
source $\rightarrow fZ + Y$	k_5	$k_5 = 1.32 \times 10^{-6}$ M s^{-1}
$Z \rightarrow X$	$k_6[Z]$	$k_6 = 2.04 \times 10^{-3}$ s^{-1}

[a] $X \equiv HBrO_2$, Y ≡ bromide and Z ≡ 1,4-dihydroxybenzene

the system was configured close to the bifurcation point and observed the existence of an optimal volume to support oscillation. The simulation results are expected to motivate the corresponding experiments in microreactors defined using microfluidic techniques (chapters 3 and 4).

Deterministic model

The full model of bromate–CHD system consists of 17 species and 25 reactions [148]. As shown in Table 2.1, it can be reduced to a three-variable model [149] using quasi-steady-state assumption and pool-component approximation. The bifurcation parameter f is essentially the ratio of 1,4-dihydroxybenzene production rate and bromide production rate, and it can be tuned by the initial species concentration.

It is straightforward to obtain the bifurcation diagram according to the deterministic model (Table 2.1). The concentration of X as a function of time reaches either a steady state or an oscillatory state after a short transient period (figure 2.3, black). By plotting the maximum and minimum values of [X] as a function of f, we obtained a phase diagram (figure 2.2) illustrating the Hopt bifurcation between the two possible dynamical behaviors.

Stochastic simulation and system-size resonance

In this section, Gillespie algorithm [40, 109] is used to study the influence of stochasticity of chemical reactions on the system dynamics when $f \approx 1.05$, close to the second bifurcation point.

As shown in figure 2.3(a), the deterministic limit-cycle behavior is largely preserved in all stochastic simulations. The deviation from perfect periodic kinetics is bigger when the system volume is

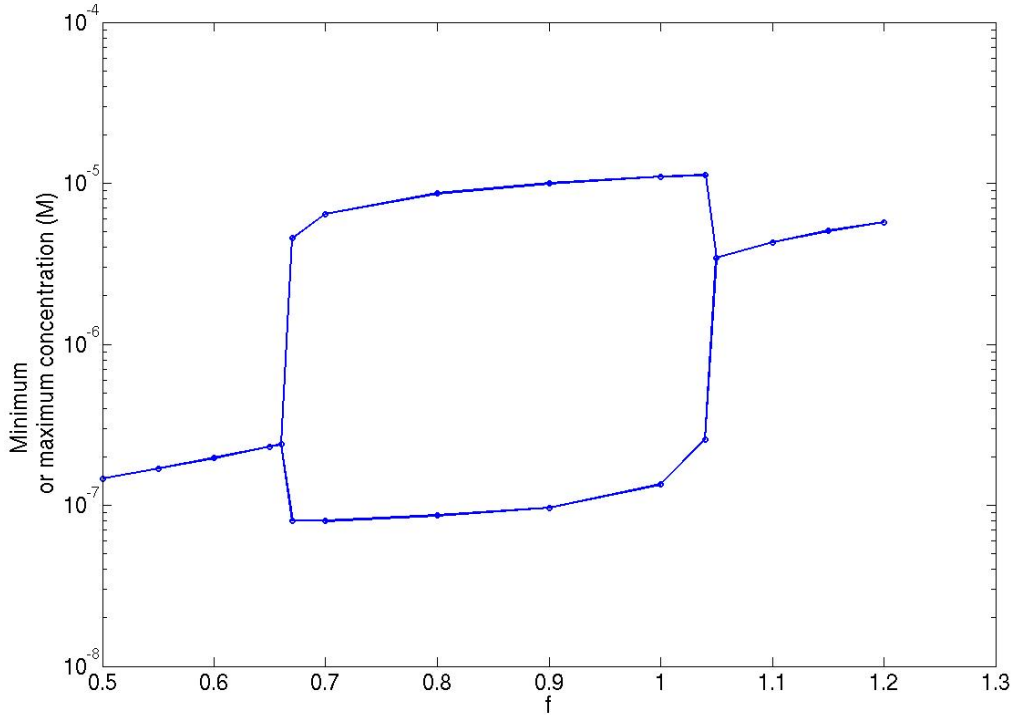

Figure 2.2. Bifurcation diagram based on deterministic simulation of the reduced model. The minimum and maximum concentration of X are plotted as a function of f.

decreased, in agreement with theoretical consideration in a more general context [37, 38]. This observation holds true independently of the value of control parameter f as long as system volume is not too small (compare red curves with black ones in figure 2.3). However, when more noise is present due to the decrease of system volume, the behavior of the system may show qualitatively different feature (compare green or blue curves with black ones in figure 2.3(b) and figure 2.3(c)). In particular, the system may be excited from steady state to limit cycle transiently and exhibit pronounced oscillation.

To quantify the periodicity in these kinetic traces, we consider the power spectral density (PSD) of figure 2.3. The PSD of a time series is defined as the magnitude square of its Fourier transform. All time series being of finite length, a Hamming window is used to reduce the contribution of spurious side peaks. The simulation data has a sampling rate of 1 Hz and around 10^5 points, sufficient to get a converging estimate of PSD. It is divided by a Welch window of 1024 with 50%

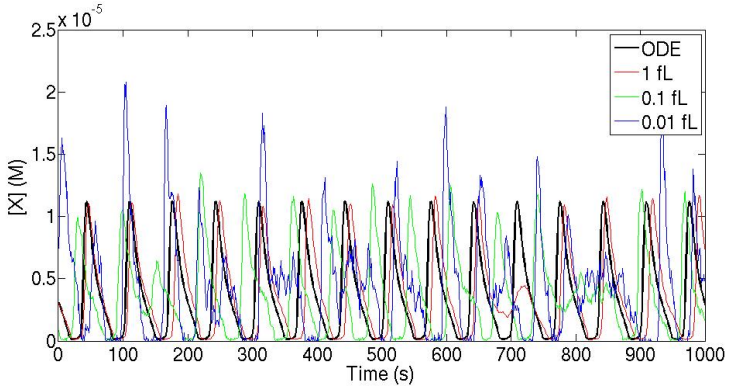

(a)

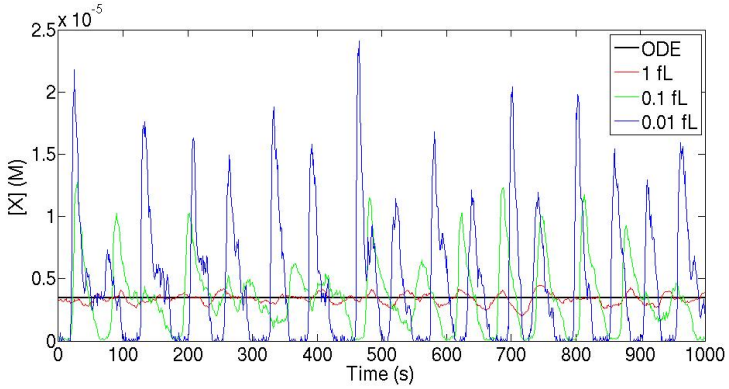

(b)

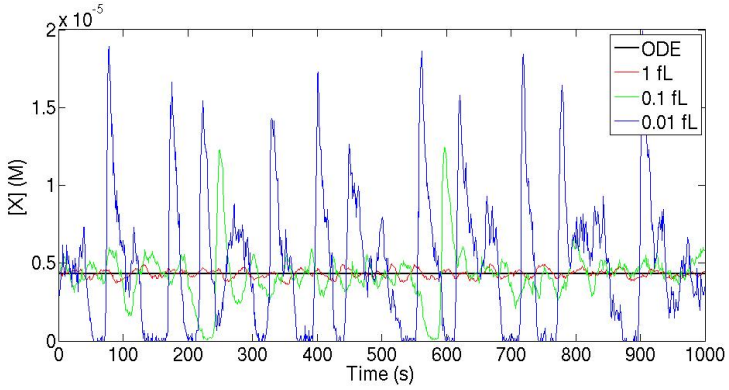

(c)

Figure 2.3. The concentration of X from deterministic (black) or stochastic simulation with system volume of 1 fL (red), 0.1 fL (green), and 0.01 fL (blue) at $f = 1.03$ (a), 1.05 (b), and 1.10 (c).

overlap to smooth the final PSD. A signal-to-noise ratio (SNR) is then obtained from the peak of PSD using $SNR \equiv \frac{P(\mathrm{B})}{P(\mathrm{A})} \frac{f_\mathrm{B}}{f_\mathrm{C} - f_\mathrm{B}}$. Here $P(\mathrm{B})$ is the PSD at the signal peak located at f_B, $P(\mathrm{A})$ is the minimum PSD to the left of the peak, and f_C is the frequency which satisfies $P(\mathrm{C}) = P(\mathrm{B})/e^{1/2}$ (figure 2.4(b)). SNR reflects the periodicity of the time series in a quantitative way. For example, at $f = 1.05$, the deterministic simulation does not show any periodicity (figure 2.3(b), black), so its PSD (figure 2.4(a)) has no nonzero peaks. With the introduction of stochastic noise, the system undergoes significant periodic fluctuation (figure 2.3(b), green) and there is a clear peak in its PSD (figure 2.4(b)) at 0.015 Hz, the limit-cycle frequency for $f = 1.04$.

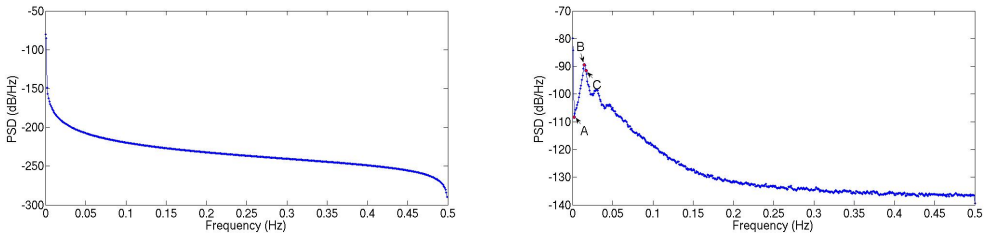

(a) (b)

Figure 2.4. The PSD of [X](t) from deterministic (a) or stochastic (b) simulation with $V = 0.1$ fL and $f = 1.05$.

Figure 2.5 summarizes the relation between SNR and system volume at different values of the bifurcation parameter. When the system is inside the limit-cycle region (figure 2.5, red and green), the destructive effect of stochastic noise is reflected in the decrease of SNR with decreasing volume. The sensitivity of SNR to system volume is bigger when f is further away from the bifurcation point mostly due to bigger SNR at large volumes, which is consistent with the intuition that limit cycle is more stable in that region. When the system is slightly outside the limit-cycle region (figure 2.5, blue and black), the noise induces periodic fluctuations with a characteristic frequency close to the neighboring limit-cycle value (Table 2.2). This influence tends to be more significant when system volume is reduced to introduce more noise (figure 2.5, black). When f is very close to the bifurcation point, there exists an optimal volume where SNR is maximized (figure 2.5, blue). This phenomenon has been reported previously in other systems [60–62, 64, 120, 125], and associated with stochastic

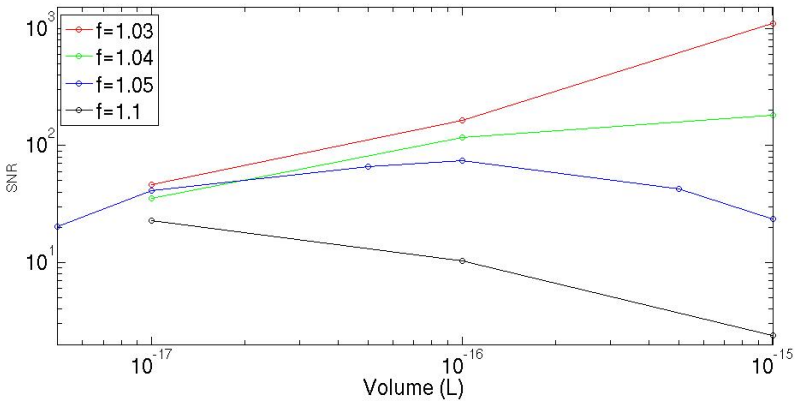

Figure 2.5. SNR as a function of system volume at different values of the bifurcation parameter f by spectral analysis of time series [X](t) from stochastic simulations.

resonance [32] where a system driven by external periodic force is more responsive to noise of a certain magnitude. In the context of chemical reactions, noise is inversely proportional to the square root of system volume [39, 166], so the optimal noise strength translates to an optimal volume. From a mathematical point of view, SNR for small system volumes tends to be less dependent on the value of f, whereas for big system volume, it closely follows the deterministic results. As f increases and crosses the bifurcation point, SNR for big volumes increases significantly, and at some particular f, it must be very close to the SNR for small volumes. At this point, because SNR assumes similar values at big and small volumes, there must exist at least one extremum at intermediate volumes as long as SNR is dependent on volume.

Table 2.2. The peak frequency of PSD as a function of volume and bifurcation parameter

Volume (L)	Peak frequency (Hz)			
	$f = 1.04$ (deterministic)	$f = 1.04$ (stochastic)	$f = 1.05$ (stochastic)	$f = 1.1$ (stochastic)
5×10^{-18}	0.015	—	0.016	—
1×10^{-17}	0.015	0.016	0.016	0.016
5×10^{-17}	0.015	—	0.016	—
1×10^{-16}	0.015	0.016	0.015	0.016
5×10^{-16}	0.015	—	0.015	—
1×10^{-15}	0.015	0.015	0.015	0.017

Finally, even when the system volume is big enough to prevent the appearance of significant

fluctuation around the steady state (figure 2.3(b) and 2.3(c), red), there is still a well-defined peak in the PSD with SNR > 1. PSD being the Fourier transform of the correlation function, a peak in PSD implies that the system relaxes to the steady state in an oscillatory fashion [37]. A high SNR means the relaxation time is longer than the oscillation period. Considering that the peak frequency is still similar to the neighboring limit-cycle frequency, one could extract some information regarding the limit cycle region from a spectral analysis of the fluctuation around the steady state.

Conclusion

In this section, we analyze a reduced model of bromate–CHD system which supports oscillatory kinetics in bulk under appropriate conditions. Comparison between deterministic and stochastic simulations reveals the effect of random noise on the dynamical features of the system. In general, noise adds a perturbation to the deterministic trajectory. When the system is configured very close to the bifurcation point, chemical reaction noise may transiently push the system over the bifurcation point, and one would observe limit-cycle behavior when steady state is predicted by the deterministic model. Even when the noise is not strong enough to change the dynamics qualitatively, it induces fluctuation whose power spectrum contained valuable information on the nearby limit-cycle region. Moreover, when the bifurcation parameter assumes some particular value very close to the bifurcation point, there exists an optimal system volume for the excitation of steady state by stochastic noise. This phenomena is closely related to stochastic resonance.

This study may lead to the experimental verification of the conclusions drawn above from numerical investigations. With the advancement of microfluidic techniques, it is straightforward to observe the bromate–CHD reaction in femtoliter reactors with tunable volume [68, 116] and study the influence of chemical noise on reaction kinetics.

2.1.2 Stochastic Defocusing of Peroxidase–Oxidase System in Response to Initial Conditions

Introduction

Chemical reactions are in nature a random process, but the stochasticity does not manifest itself in traditional bulk experiments dictated by the ensemble average of the behavior of a large number of molecules [166]. Chemical reactions essential to biological systems are conveniently studied in terms of the time evolution of the components' concentrations, and lots of useful information has been extracted and used to construct complicated metabolic [5] and genetic [31, 132] oscillators in vivo. Real cellular environment, however, differs from in vitro experiments in two fundamental aspects. First, in many cases only a small number of molecules are involved in biochemical interactions [110]. For example, in a highly compartmentalized cell, reactions often take place in a small volume on the order of femtoliters, so the copy numbers of involved molecules are much smaller than that in bulk experiments. Small copy numbers are also characteristic of genetic materials [89]. In addition, cellular environment is extremely crowded, so diffusion of molecules is much slower than in dilute solution [99].

An intuitive way to address the first problem is to study biochemical reactions in microreactors. With the development of "lab on a chip," fabrication of microreactors have been more and more accessible to chemists and biologists [23, 66]. Much effort has been put into understanding the physics of fluid at micrometer scale [133], and integrating and parallelizing processes in microfluidic chips [93]. High throughput, low reagent consumption, and fast turnout rate are among the most often cited advantages of microfluidics. More relevant to this work, it is possible to fabricate microreactors comparable in size to real cellular compartments and thus more relevant to the investigation of biochemical reactions in their native conditions. The deterministic approach of reaction kinetics based on law of mass action should give way to its stochastic counterpart when it is used to predict or interpret experimental results in microreactors. For a well mixed microreactor, the stochasticity can be accounted for by using Gillespie's stochastic simulation algorithm or its variants [40]. Although, as mentioned above, diffusion in cellular environment is hindered due to molecular crowding, there

is some evidence that only minor modification is required to take crowdedness into account [41]. So for this work, Gillespie algorithm [40, 109] is used to simulate biochemical reactions in a confined volume of femtoliter scale.

The inherent randomness of chemical reactions adds noise to the deterministic evolution of a biochemical system. The effect is more significant when a nonlinear system is of interest. Noise-induced phenomena have been explored in both abstract [37, 59] and realistic chemical reaction networks [6, 47, 171]. Peroxidase–oxidase (PO) oscillator [103] is a well-studied nonlinear system of biological importance. A recent review summarizes the current models for PO system [12, 56, 119], and the list of relevant reactants are still being updated. Although an abstract model was proposed around 30 years ago [103], realistic models have been the interest of different groups to explain various dynamical behavior observed in PO systems in appropriate part of its parameter space [9, 11, 12, 104, 119]. By taking stochastic effects into consideration, it is possible to predict the behavior of the PO system in a confined space and compare it against experimental results.

We compared the asymptotic behavior of the PO system as a function of initial H_2O_2 concentration [56] using stochastic and deterministic simulation methods. The results demonstrated the effect of the randomness of chemical reactions even when the system volume is as big as 100 fL. It may be compared to stochastic defocusing [72] reported for other systems. This work is expected to prompt future experimental investigations to quantitatively test the prediction of numerical simulation.

Deterministic model

PO system can manifest oscillatory or steady-state behavior under different conditions. For example, it was observed that initial concentration of H_2O_2 determined the asymptotic behavior of the PO system (i.e., steady state or periodic oscillation). To be particular, deterministic simulation of the BFSO model [56] showed that when $[H_2O_2]_0 < c_0$, the system oscillated with a defined period, and when $[H_2O_2]_0 > c_0$, steady state was eventually achieved. The critical concentration c_0 was determined to be ≈ 0.29998 μM from a reaction network (BFSO model) composed of 14 reactions and 11 species (Table 2.3). We take this as a case study to explore the stochastic effect of chemical

Table 2.3. BFSO model for PO system [56]

Reaction	Rate constant	Unit
$NADH+O_2 + H^+ \rightarrow NAD^+ + H_2O_2$	10.0	$M^{-1}\ s^{-1}$
$H_2O_2 + Per^{3+} \rightarrow$ compound I	1.8×10^7	$M^{-1}\ s^{-1}$
compound I + NADH $\rightarrow$ compound II + NAD$\bullet$	4.0×10^5	$M^{-1}\ s^{-1}$
compound II + NADH $\rightarrow Per^{3+} +$ NAD$\bullet$	2.6×10^5	$M^{-1}\ s^{-1}$
NAD$\bullet$ + $O_2 \rightarrow NAD^+ + O_2^-$	2.0×10^7	$M^{-1}\ s^{-1}$
$O_2^- + Per^{3+} \rightarrow$ compound III	1.7×10^7	$M^{-1}\ s^{-1}$
$2O_2^- \xrightarrow{2H^+} H_2O_2 + O_2$	2.0×10^7	$M^{-1}\ s^{-1}$
compound III + NAD$\bullet \rightarrow$ compound I $+ NAD^+$	6.0×10^7	$M^{-1}\ s^{-1}$
$2NAD\bullet \rightarrow NAD_2$	5.6×10^7	$M^{-1}\ s^{-1}$
$Per^{3+} + NAD\bullet \rightarrow Per^{2+} + NAD^+$	1.8×10^6	$M^{-1}\ s^{-1}$
$Per^{2+} + O_2 \rightarrow$ compound III	1.0×10^5	$M^{-1}\ s^{-1}$
$\rightarrow$ NADH	7×10^{-8}	$M\ s^{-1}$
$\rightarrow O_2$	5.28×10^{-8}	$M\ s^{-1}$
$O_2 \rightarrow$	4.4×10^{-3}	s^{-1}

reactions.

The transition is quantified by plotting the probability of limit cycle behavior with respect to $[H_2O_2]_0$. As expected, deterministic simulation predicts that the transition from limit cycle to steady state is discontinuous, and the system's behavior is not well defined if $[H_2O_2]$ starts exactly from c_0. The behavior of the system starting away from c_0 ends up to be either steady state or periodic oscillation after a short transient period. As is shown in figure 2.6 (red lines), deterministic simulation shows that PO system will assume either steady state or oscillatory state depending on the initial concentration of H_2O_2 even if it is very close to c_0 (figure 2.6(c)).

Stochastic simulation and result

The transition around c_0 should be sharp but continuous in reality. In this case stochastic simulation is invoked to resolve the discontinuity by taking stochastic effect into consideration.

Intuitively, the concentrations of involved species in the system are fluctuating around the deterministic results in stochastic simulations as shown in figure 2.6. However, when the system is initiated using $[H_2O_2]_0 \approx c_0$, the system's fate lost its predictability. Either steady state or oscillation may be the ultimate choice (compare blue and green lines in figure 2.6). Interestingly, no transition between the two choices was observed within a realistic period of time (data not shown).

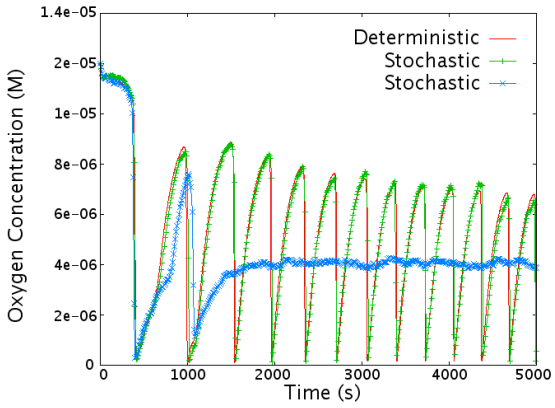

(a)

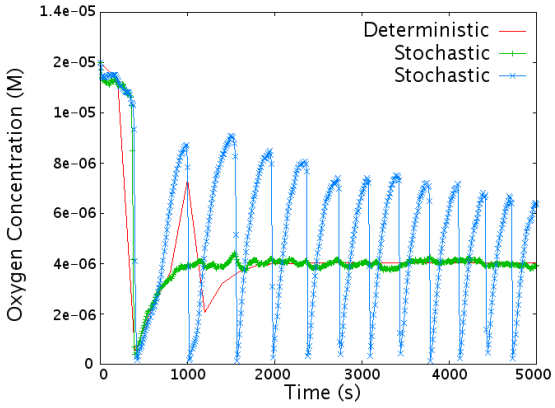

(b)

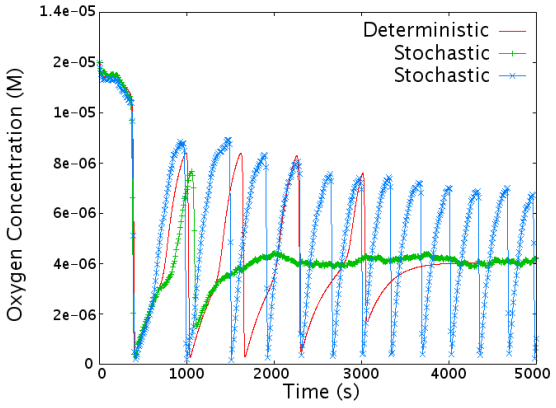

(c)

Figure 2.6. Oxygen concentration as a function of time for $[H_2O_2]_0 = 0.28$ μM (a), 0.32 μM (b), or 0.30 μM (c). Red: Deterministic simulation results; green and blue: stochastic simulation with qualitatively different results (system volume is 10^{-15} L).

The response of the system to initial conditions is then quantified by running the simulation a sufficient number of times and calculating the probability of finding the system in either of the two attractors.

Among N independent simulations of the system, the number n of instances of oscillation obeys a binomial distribution of mean Np and variance $Np(1-p)$, where p is the probability of the system assuming oscillatory behavior. With a confidence of 95%, N should satisfy

$$\frac{2\sqrt{Np(1-p)}}{Np} < 0.05$$

to achieve an error $\leq 5\%$ in p. In particular, $N > 1600$ if $p \approx .5$. Therefore, more than 1600 simulations of the BFSO model for each initial $[H_2O_2]_0$ were used to calculate p and its error using

$$\begin{aligned} p &= \frac{n}{N}, \\ \Delta p &= \frac{2\sqrt{Np(1-p)}}{N}, \end{aligned}$$

respectively.

Figure 2.7 shows the convergence of p to a constant when the number of simulation is increased. In these simulations, $[H_2O_2]_0$ is chosen to be 0.30 μM, and 1600 simulation runs were carried out with different length of simulation time. The probability for the system to be in either oscillatory or steady state was estimated after the completion of each simulation and plotted against the number of finished simulation runs. Clearly, once a sufficient number of simulations are realized, we would be able to get a very accurate estimate of p. In addition, even if different simulation time is used, the estimated p is within statistical error of one another, suggesting that 5000 s is enough for the system to relax to an attractor.

The purpose of this work is to explore the effect of system size on the behavior of the system when $[H_2O_2]_0$ is changed in the critical region. Simulations were carried out using different $[H_2O_2]_0$, and the probability p of oscillatory state was calculated as above. From the results summarized in figure. 2.8, one readily sees the effect of stochastic nature of chemical reactions: the transition from

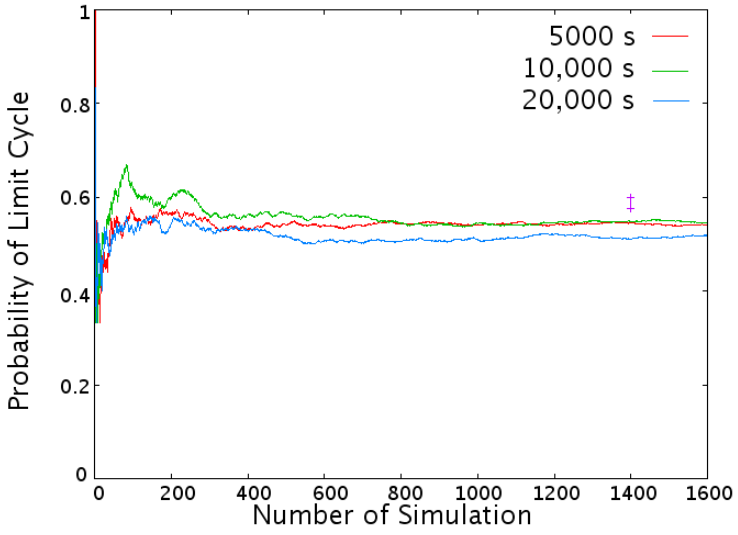

Figure 2.7. Convergence of p when the number of simulation runs is increased. System volume was 10^{-15} L, and simulation time was 5000 (red), 10,000 (green), or 20,000 (blue) s. After 1600 simulation runs, p is within statistical error (purple bar) of one another.

oscillatory behavior to steady state is a *continuous* function of $[H_2O_2]_0$. This transition approaches to step function as system volume is increased. However, even when $V = 10^{-13}$ L, the probability of oscillatory dynamics for $[H_2O_2]_0$ close to c_0 is still about 0.5, far away from possible deterministic values of 0 or 1.

It is intuitive to understand the results with a much simplified picture of a particle moving in a double-well potential. Here the valley of the double well corresponds to either oscillatory behavior or steady state. $[H_2O_2]_0$ determines the initial position of a ball moving under the influence of both the potential and a random force. The potential, originated from the reaction network, exerts a deterministic force on the ball's movement; the random force is due to the stochastic nature of chemical reactions, and its magnitude is inversely proportional to the square root of the system volume [39]. In our particular PO system, the barrier between the wells is so high compared with random force that no transition between wells is observed once the system settles in either well. But if the system starts very close to the top of the barrier, random force may be strong enough to perturb it to either side with almost equal probability. Even when the random noise in decreased by increasing system volume, the fate of the system is undetermined as long as it is close enough to

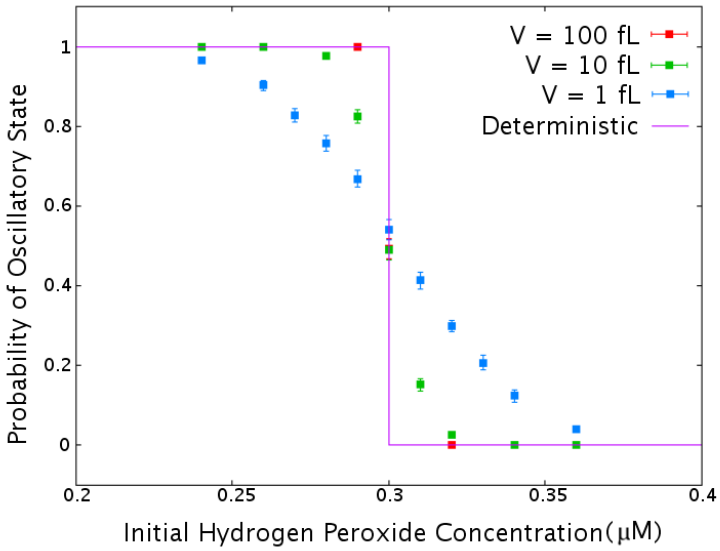

Figure 2.8. The probability of observing oscillatory behavior in PO system as a function of initial H_2O_2 concentration. System volume was 10^{-13} L (red), 10^{-14} L (green), or 10^{-15} L (blue). Deterministic result was also shown as a line.

the top of the barrier; in fact, p is independent of system volume ranging from 1 fL to 100 fL when $[H_2O_2]_0 = 0.30$ μM. It turns out that p is very close to 0.5 under this condition, and this suggests that the potential is quite symmetric at the barrier top. The symmetric feature of the potential is also reflected in the symmetric shape of the curves in figure 2.8 in smaller volumes around the point $(c_0, 0.5)$.

Conclusion and discussion

In summary, we carried out stochastic as well as deterministic simulations of PO system using realistic reaction models. The behavior of the system, controlled by the initial H_2O_2 concentration, exhibits a continuous transition when reaction noise is accounted for. Its deviation from the discontinuous transition predicted by deterministic simulation is more obvious when system volume is smaller, but very close to the critical H_2O_2 concentration, all stochastic results show significant deviation from deterministic prediction independent of system volume.

The experimental verification of the above conclusion is expected to be a direct corroboration of

master-equation approach to chemical reaction kinetics. From a practical point of view, this system is easier to handle for the control parameter is the initial concentration of a reagent. This saves us from maintaining the concentrations of certain chemicals during the course of the experiment as normally required by some other oscillators. The fate of the system after a short transient period may assume either one of the two qualitatively different choices, leaving little uncertainty in the interpretation of the data. With the advent of microfluidics, such experiments may be carried out with high throughput to gain enough statistics for comparison with numerical results.

The smoothing of a discontinuous transition is very similar to stochastic defocusing where the steepness of the system's response curve to the control parameter is reduced by stochastic noise in chemical reactions [72]. It would be interesting to determine whether this is detrimental or beneficial to living organisms and how nature avoids or employs this effect.

2.2 The Effect of Diffusion on Confined Enzymatic Reaction Cascades

2.2.1 Introduction

In vitro studies on biological systems have attracted more and more interests among biologists and chemists by offering a typical reductionists' way of tackling complex problems pertaining to life sciences [1]. Practically, chemists in this area are working in a biological setting by leveraging their expertise on chemical reactions. Just as the property of a molecule can, at least in principle, be deduced from the constituent atoms and bonds, the interesting behaviors of complex biological systems can also be explained by studying their basic elements, that is, chemical reactions and their communications.

Most of the chemical reactions in cells are catalyzed by different enzymes with a very high specificity and efficiency. Usually, enzymes are regarded as factories converting raw materials to end products. These factories are not working independent of one another; rather, they function as a whole entity to generate the multitude of life sciences. To wire these enzymes together, na-

ture has to tune the communication among them appropriately. This communication is mediated through the coupling of enzymatic reactions. Two reactions are coupled by sharing the same type of molecule in their reaction schemes. The shared molecule may be small metabolites or macromolecules, including enzymes themselves. These communications usually lead to a very large and correlated reaction network whose dynamics cannot be predicted simply by intuition. Numerical simulation using stochastic algorithm has been successful in solving the dynamics of complicated reaction networks [40, 108].

Compared with bulk chemical reactions, the complexity of biological system is more evident when spatial constraints are taken into consideration. In this sense, diffusion is influential in determining the dynamics of the reaction network. In section 2.1, biochemical reaction networks are studied under the assumption that all species are well mixed. In living cells, however, molecules interact with each other in a crowded and confined environment [99], where diffusion is closely coupled with reactive collisions. In biological systems, due to the coexistence of molecules with extremely different diffusion constants, the significance of diffusion may exhibit itself evidently. So far, people have studied the effect of diffusion on different biological systems and showed that diffusion is indispensable in the explanation [126] and prediction [35] of some complex behaviors such as synchronization and pattern formation.

The effect of diffusion may be modeled directly as discussed below in section 2.3, but it is instructive to explore its influence on the basis of some scaling analysis. Recently, a group of authors investigated the effect of spatial limitation or compartmentalization starting from timescale analysis of diffusion process and using stochastic simulations of a group of enzymes [80, 96, 136–139]. Their system (termed molecular network) is unique in that law of mass action is not valid, and nonlinear dynamics emerge. We will summarize this theory and then make some extension in different experimental contexts in this section. The following section is devoted to an outline of molecular network. In section 2.2.3, the effect of free diffusion of small molecules on one or several molecular networks are described. In section 2.2.4, a possible method is proposed to enslave the dynamics of a group of enzymes by a strong external injection of signal molecules. The feasibility of this scheme depends largely on the legality of the model in section 2.2.2.

2.2.2 Molecular Network

Consider a cellular compartment of size L in which an enzyme is converting substrates into products. The following timescale analysis [58] will reveal the existence of two different dynamic regimes, namely, local or global. First of all, because the size of enzyme is much larger than that of small molecules (substrates or products), one can neglect the diffusion of enzymes. In mathematical language, the diffusion constant of enzyme is much smaller than that of small molecules, so only the latter contributes significantly to the relative diffusion constant D. Then one has a good estimate of the time needed for a small molecule to diffuse throughout the compartment (t_{mix}),

$$t_{\text{mix}} \approx L^2/D. \tag{2.1}$$

In another word, it takes about t_{mix} for a molecule to forget its initial location.

The substrate molecule has to collide with the active site of an enzyme to start a reaction, so another important characteristic time is the traffic time, t_{traffic}, the small molecule spends on diffusion before meeting the active site of an enzyme (figure 2.9). According to reaction–diffusion theory [57], in three-dimensional space, if there is only one enzyme in the system,

$$t_{\text{traffic}} \approx L^3/DR = t_{\text{mix}} \cdot \frac{L}{R}, \tag{2.2}$$

where R is the size of the active site. The last expression in equation (2.2) means it always takes longer for a small molecule to collide with the active site of an enzyme than to transverse the cell volume. Equivalently, the small molecule has forgot its initial position before it finds an enzyme. For a real biological system, there are usually many enzymes (say, N). Then it takes a shorter period of time (t_{transit}) for the molecule to dock an active site. If the enzymes are randomly distributed in the volume,

$$t_{\text{transit}} = \frac{1}{N} t_{\text{traffic}} = \frac{L^3}{NDR} = t_{\text{mix}} \cdot \frac{L}{NR}. \tag{2.3}$$

Now the relation between t_{transit} and t_{mix} can be changed qualitatively by tuning N around a

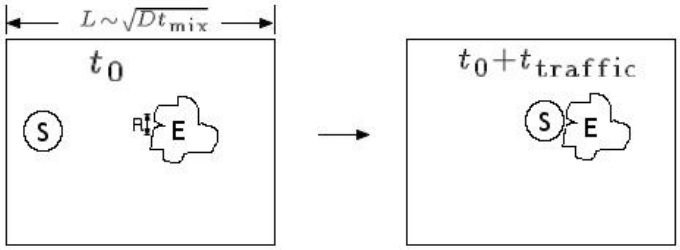

Figure 2.9. The physical meaning of $t_{\rm traffic}$. In a small volume of dimension $L \approx \sqrt{Dt_{\rm mix}}$ containing only one enzyme, the small substrate molecule spends $t_{\rm traffic}$ in diffusion before colliding with the active site (of dimension R) of enzyme E.

critical number

$$N_{\rm crit} = L/R.$$

If $N \ll N_{\rm crit}$, $t_{\rm transit} \gg t_{\rm mix}$ which means the substrate molecule has lost its memory of initial condition before docking an enzyme's active site. In another word, it is equally possible for the substrate to react with any enzyme in the system. So the enzyme can feel the *global* change of the number of substrate molecules. In the regime where $N \gg N_{\rm crit}$, that $t_{\rm transit} \ll t_{\rm mix}$ indicates the substrate molecule finds a docking site before traveling a significant portion of the volume. Alternatively, the substrate molecule only interacts *locally* with nearby enzymes.

To have a feeling of the order of magnitude, consider a volume of micrometer size containing enzymes with nanometer-sized active sites, then $N_{\rm crit} = 1000$ and the critical concentration $c_{\rm crit} \approx 10^{-6}$ M. With this number of enzymes, if the diffusion constant for small molecules is about 10^{-5} cm^2/s, then $t_{\rm mix} = t_{\rm transit} \approx 1$ ms and $t_{\rm traffic} = 1$ s.

Finally, the characteristic time of an enzyme reaction, $t_{\rm turnover} \approx 1/k_{cat}$, should be taken into consideration. If $t_{\rm turnover}$ is smaller than both $t_{\rm transit}$ and $t_{\rm mix}$, the system is equivalent to a diffusion-controlled reactor in the local dynamics regime or a well-stirred reactor in the global dynamics regime. These two scenarios are familiar to chemists. On the other hand, if enzyme dynamics is the slowest process in the system, in the global regime, during the enzyme turnover cycle, the change in the number of the substrates can be experienced by every enzyme with equal probability, because $t_{\rm mix}$ is the smallest timescale in the system. For local dynamics, one can divide the volume into several

smaller ones, each of which gives a smaller t_{mix} with almost the same t_{transit} until global dynamics is possible in these element cells. This is feasible because t_{mix} is dependent on the size of the system (equation (2.1)), but t_{transit} is controlled by enzyme concentration (equation (2.3)). In summary, the only interesting regime for new dynamics is

$$t_{\text{turnover}} \gg t_{\text{transit}} \gg t_{\text{mix}}, \tag{2.4}$$

that is, the enzyme turnover cycle is the slowest process in the system, and the diffusion of substrate is the fastest. This criterion may be fulfilled by the compartmentalization of enzymes in a volume of appropriate size, which is common in biological systems.

When equation (2.4) is satisfied, any substrate molecule has traveled throughout the system before finding an active site, and enzyme reaction is very slow compared with these two processes. From an enzyme's point of view, at every moment of its turnover cycle, it can collide with any substrate with the same possibility, and thus the change of the number of substrates affects the dynamics of each enzyme with the same strength. In such a system, the dynamics of a group of enzymes may be synchronized through the diffusion of small molecules, and it is called a molecular network [58]. To enable the synchronization, there should be a mechanism in the system for small molecules to exert their effect on the dynamics of enzymes. Various feedback mechanisms have been proposed, including product inhibition [137], product activation [96, 136, 139], allosteric activation [80], and substrate recycling [138].

It is the interest of this report to concentrate on the substrate recycling scheme in which the product is converted back to substrate by an additional fast pathway in the background (figure 2.10). It is easy to find such a reaction system in the repertoire of biological pathways. A case in point is the cycling between adenosine triphosphate (ATP) and pyrophosphate (PPi) [54] (figure 2.11). In the language of figure 2.10, substrate ATP is converted to product PPi by luciferase, and product is transformed back to substrate by another enzyme (ATP sulfurylase) which has a faster dynamics than luciferase [54]. A more well-known example, namely, enzyme cascade, is also related to this scheme. In this case the substrate is not a small molecule but a protein which can be covalently

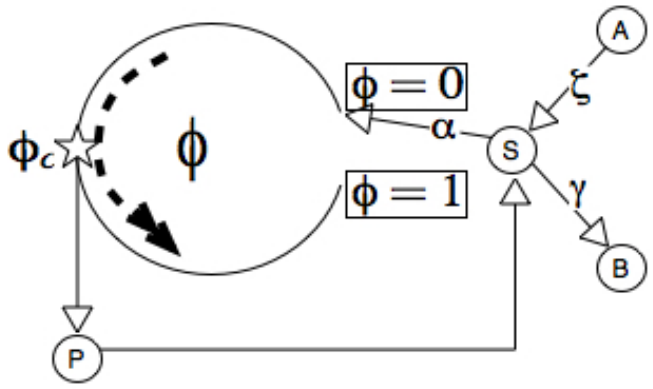

Figure 2.10. A schematic description of an enzyme in a molecular network. Substrate S is supplied and decays at a constant rate ζ and γ, respectively. Enzymatic cycle is characterized by a phase variable ϕ. When $\phi = 0$, the enzyme is available to bind with a substrate at a probability rate of α. Product P is released once $\phi > \phi_c$ and converted back to substrate immediately.

modified, say, by a phosphorylating kinase. The modified protein is then subjected to dephosphorylation spontaneously or catalytically (by a phosphatase). This cycle of phosphorylation level is equivalent to the hydrolysis of ATP. The energy stored in ATP is seemingly wasted, so it is also called a futile cycle. In a futile cycle, although the substrate is not a small molecule, its diffusion constant may assume an appropriate value to make a molecular network possible. There has been a large body of literature on the significance of this futile cycle since 1970s. It is clear now the futile cycle renders ultrasensitivity [17, 28, 29, 123, 135], zero-order sensitivity [46], memory storage [85, 86], noise reduction [158], and stochastic focusing [105]. To the best of my knowledge, all these works, either simulations or experiments, are concerned with steady-state behavior or fluctuation around the steady state. The uniqueness of molecular network is its departure from steady-state simulation to real dynamic exploration. The surprising results show the synchronization of the dynamics of the enzymes in a molecular network [138].

Before showing the numerical result reproduced by me, it is useful to briefly describe how to simulate a system described in figure 2.10 (for more detail, see reference [137]). One first approximates the turnover cycle of an enzyme as a one-dimensional diffusion process on a biased potential surface. Numerical simulation has shown the possibility of this reduction of dimensionality in the context

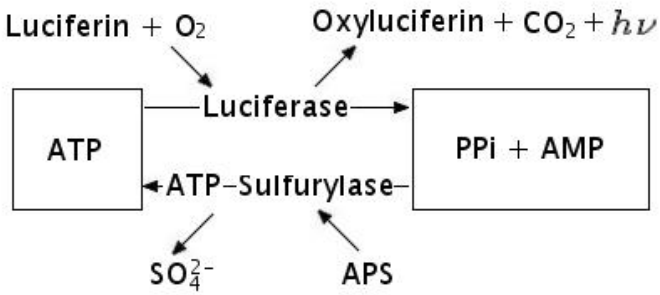

Figure 2.11. A possible realization of the enzymatic cycle in figure 2.10. Substrate ATP is converted to product PPi by luciferase with the consumption of luciferin. PPi is readily used by ATP sulfurylase to regenerate ATP using APS (adenosine phosphosulfate). The activity of luciferase can be monitored by luminescence.

of protein folding [10]. A phase parameter $\phi \in [0, 1)$ is used to characterize the state of enzyme or enzyme–substrate complex in its configuration space [79]. When $\phi = 0$, the enzyme is ready to bind with a substrate with probability rate α. In a molecular network, the possibility of the binding of a substrate molecule with an enzyme in time interval dt is

$$1 - (1 - \alpha dt)^s \approx \alpha s dt,$$

where s is the number of free substrate molecules in the system. After the formation of enzyme–substrate complex, phase parameter ϕ is evolved according to the following Langevin equation,

$$\frac{d\phi}{dt} = v + \eta(t), \tag{2.5}$$

where v is the drift velocity along the potential surface of enzyme–substrate complex, and $\eta(t)$ is a Gaussian noise introduced to simulate the effect of thermal fluctuation. Drift velocity is simply assumed to be the reciprocal of t_{turnover}, which is equivalent to approximating the conformational evolution of enzyme–substrate complex as a "clock." This clock, however, is not accurate due to the

existence of Gaussian noise $\eta(t)$ with a delta correlation function

$$\langle \eta(t)\eta(t') \rangle = 2\sigma\delta(t-t'),$$

where correlation intensity σ can be related to the dispersion ξ of turnover time as follows [79, 138]

$$\xi \approx (2\sigma\tau_{\text{enzyme}})^{1/2}. \tag{2.6}$$

As ϕ is increased from 0 according to equation (2.5), it will pass a critical point ϕ_c when a product is released and the enzyme begins the relaxation toward the initial configuration which is also the end of an enzymatic turnover cycle. This clock approximation, despite of its roughness, grasps the essence of a typical enzymatic cycle. Indeed, the binding of substrate molecule changes the potential surface of a single enzyme so that the initial configuration is not an energy minimum for the enzyme–substrate complex, and this complex relaxes along the rugged downslope of potential surface [10]. This is consistent with the fact that it is the transition state rather than substrate that is stabilized by an enzyme. After the release of product, the potential energy surface recovers and the enzyme relaxes backward toward initial configuration. The rate of relaxation may be different from that of the previous downslope motion because the substrate is absent. It should be noted that the detail of the reaction is not covered in the turnover cycle simulated by equation (2.5).

Under this simulation scheme, the dynamics of a group of enzymes in a molecular network shows the synchronization of the turnover cycle of individual enzymes. In particular, the enzymes self-organize into group(s) which behaves like a single enzyme. Figure 2.12 depicts the time evolution of the number of substrate molecules in a molecular network. The oscillation is the result of synchronized activity of individual enzymes. Without synchronization, the number of substrates would be distributed randomly around the steady-state value. With synchronization, the enzymes in the system release products, which are converted back to substrates at once, almost simultaneously and thus peaks of substrate generation are observed. The number of free enzymes also oscillates at the same frequency as expected.

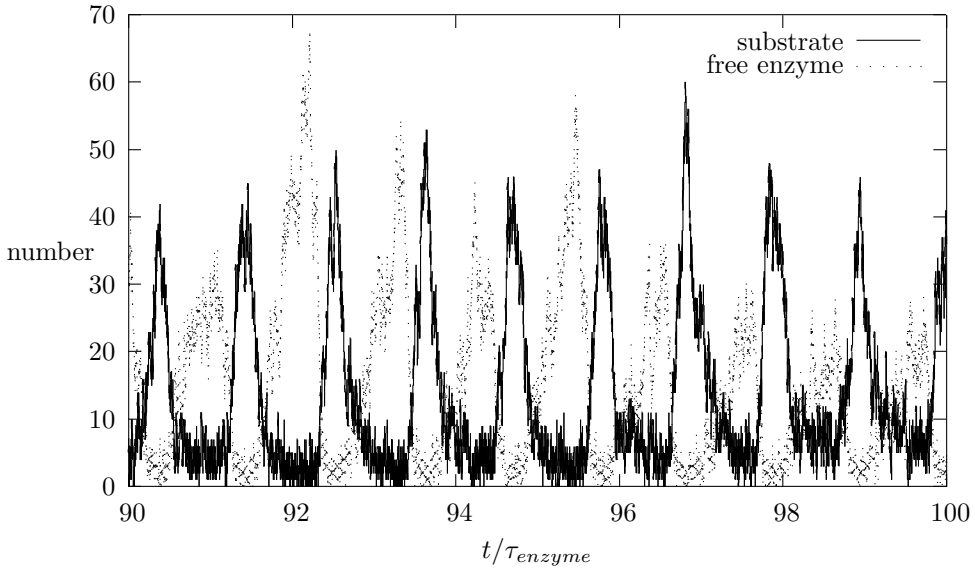

Figure 2.12. The number of substrates (line) and free enzymes (dots) as functions of time in a molecular network consisting $N = 1000$ enzymes. Other parameters were $\phi_c = 0.2$, $\xi = 0.02$, $\gamma = 15/\tau_{\text{enzyme}}$, $\zeta = 200/\tau_{\text{enzyme}}$, and $\alpha = 10/\tau_{\text{enzyme}}$.

The generation of synchronization might be related to the clock nature of every single enzyme. In a highly abstract mathematical theory of Kuramoto, clocks can be synchronized by strong enough coupling to give coherent dynamics [143]. This idea has been verified in a real chemical system [73, 98]. It is interesting to ask if similar behavior is possible in biochemical systems. It seems difficult to find a biological system that can be described by a clock as simple as that in Kuramoto theory. Also, the coupling in real world is more complicated. But the molecular network mentioned in this section is a reasonable approximation to real biological dynamics and possible connection between real biological systems and Kuramoto theory. It would be instructive to understand molecular network within the framework of a mathematical theory on coupled oscillators or clocks.

Oscillation is important to the control of metabolism [25, 75], so people have been interested in its origin. In general, oscillation is typical of nonlinear chemical reactions whose dynamics have inherent periodic solutions. The resulting periodicity is a feature of the nonlinear differential equation based on law of mass action. Researchers have proposed different mechanism to elucidate the oscillations observed in biological systems along this line [45]. In contrast, in the cycling scheme in figure 2.10, traditional kinetic equations do not have nonlinearity [138]. When space constraints are considered,

periodicity emerges in the dynamics. It is interesting to study if this mechanism can be exemplified in a real biologically relevant system in vitro. If that is the case, one may further look for its existence in vivo.

2.2.3 The Coupling among Molecular Networks

As mentioned above, the emergence of oscillation is related to the clocklike assumption on the dynamics of the enzymes in the molecular network. In the original model [138], the communication among enzymes is analyzed a priori in terms of the separation of timescales, so the detail of this communication is not embodied in the model. Other researchers have made simulations of similar systems using more realistic models, for example, network [147] or random walk [168], to describe communication among enzymes and revealed their significance on the synchronization of enzymes. In contrast to these studies, the dynamics of several molecular networks coupled together by the diffusion of small molecules seems interesting if we think about the problem at a higher level. Here, each molecular network rather than each enzyme behaves like a clock and influences other networks through different communication methods. This idea is not new in literature. For example, some researchers were interested in the synchronization of many neuron networks rather than that of neurons in a single network [97]. The interaction among several molecular networks was only reported very recently [14].

In terms of experimental research, it is also useful to study the behavior of several molecular networks for it is easier to observe the dynamics of each network (∼micrometers) than that of a single enzyme (∼nanometers). In our lab, protein patterns have been made with a high precision of spatial definition [67]. These protein patches might act as molecular networks and interact among one another by the diffusion of small molecules. Furthermore, in real biological systems, like cell membrane, domains with a high concentration of a certain enzyme are universal, and they might talk with each other rather than work independently [51, 92]. All these can be cast into a model composed of several molecular networks connected by the diffusion of small molecules. Before tackling this problem, it is also useful to start from a much simpler scheme.

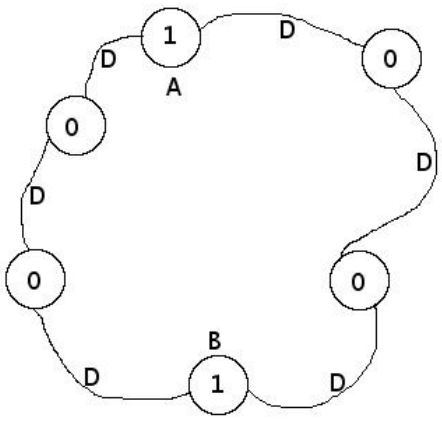

Figure 2.13. Connected molecular networks. The transportation of small molecules among vesicles is approximated by a stochastic hopping process with probability rate D. Each sphere labeled "1" denotes a GUV in which the criterion for molecular network is satisfied and enzymatic cycles in figure 2.10 are also found. Those labeled "0" lack the key enzymes in figure 2.10, but still have the source and the sink pathways of substrates.

2.2.3.1 Hopping Mechanism

The simplest method to model the diffusion among molecular networks is random walk. Actually there have been efforts to set up a network of giant unilamellar vesicles (GUVs) connected by lipid tubules [69, 71]. Normally, these microtubules are barely visible under light microscopy because of their small diameters, but mass transportation through these lipid "bridges" has been confirmed by fluorescence microscopy. By tuning the diameter and length of the bridge, the effective transportation coefficient among connected GUVs may be adjusted. If the reaction in each GUV can be treated as a molecular network, it is possible to study the effect of connectivity on the dynamics of coupled molecular networks by running biochemical reactions in vesicle networks. Thus, it is useful to get some insight of the dynamics of coupled molecular networks by numerical simulation.

Figure 2.13 shows the cyclic connection of six molecular networks which may be vesicles in real experiments. These vesicles are of an appropriate size to satisfy the criterion of molecular networks (equation (2.4)), but they may or may not be loaded with the key enzymes in figure 2.10 and

thus labeled "1" or "0", respectively. A parameter D is used to describe the probability rate for small molecules to jump to adjacent vesicles. By increasing this parameter, the correlation between adjacent molecular networks is enhanced. As a proof of concept, the numbers of substrates in the two type 1 vesicles in figure 2.13 are simulated and compared in figure 2.14 for two different values of D. The cyclic arrangement in figure 2.13 is equivalent to an infinite array of molecular networks separated by two "empty" compartments lacking enzymes. As D increases, the phase difference between the substrate oscillation in the two molecular networks changes from 180° to 0°. This is consistent with our intuition because D is a measure of coupling strength between molecular networks. In a different context, increasing coupling also leads to the synchronization of electrochemical oscillators [73]. Note that usually it is the cumulative behavior that is the output of a biological unit, so the ability to tune the correlation among constituent molecular networks enables a cell to generate qualitatively different output to other pathways. In particular, the oscillation of a single molecular network is buried in the overall output if there is no correlation among constituent networks, whereas oscillatory output is achieved if every molecular network rocks almost in phase. In a case as simple as figure 2.13, a phase difference of 180° makes the overall output only half of that for two synchronized networks. The ability of generating oscillation and tuning its amplitude is significant in the control of the metabolism and signal transmission, because oscillatory signal can trigger cell response even if average signal intensity is below the threshold [25]. It is also straightforward to test this conclusion in a real GUV network.

2.2.3.2 Effect of Free Diffusion and Distance

Let us returned to address the question put forward at the beginning of this section: the dynamics of several molecular networks coupled by the diffusion of small molecules. Besides the effect of diffusion on a single molecular network, the significance of internetwork distance is also considered in this subsection.

To simulate this system numerically, one has to combine the simulation of diffusion equation and molecular networks. We start this endeavor from the simplest case, that is, one-dimensional

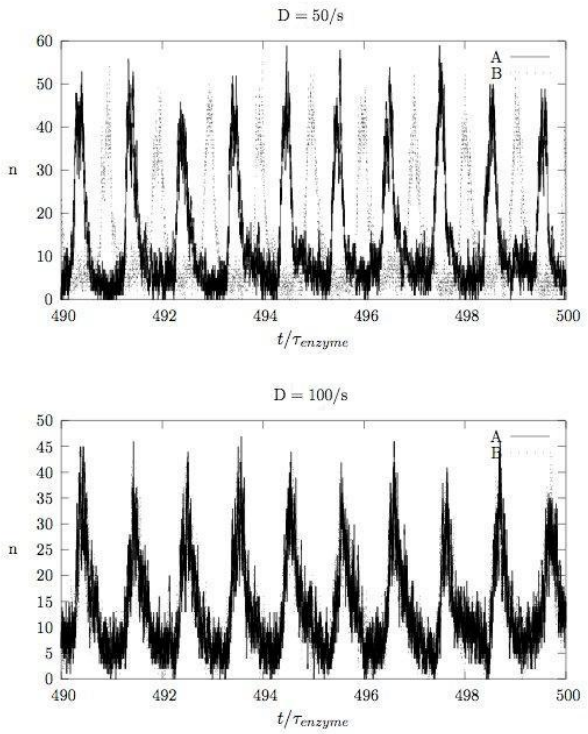

Figure 2.14. The number of substrates (n) in the two molecular networks (labeled "1" in figure 2.13) as a functions of time. Upper panel: Hopping probability rate (D) is $50/\tau_{\text{enzyme}}$ and the dynamics of two networks (A and B in figure 2.13) are not synchronized. Lower panel: D is increased to $100/\tau_{\text{enzyme}}$ and the dynamics of A and B are synchronized.

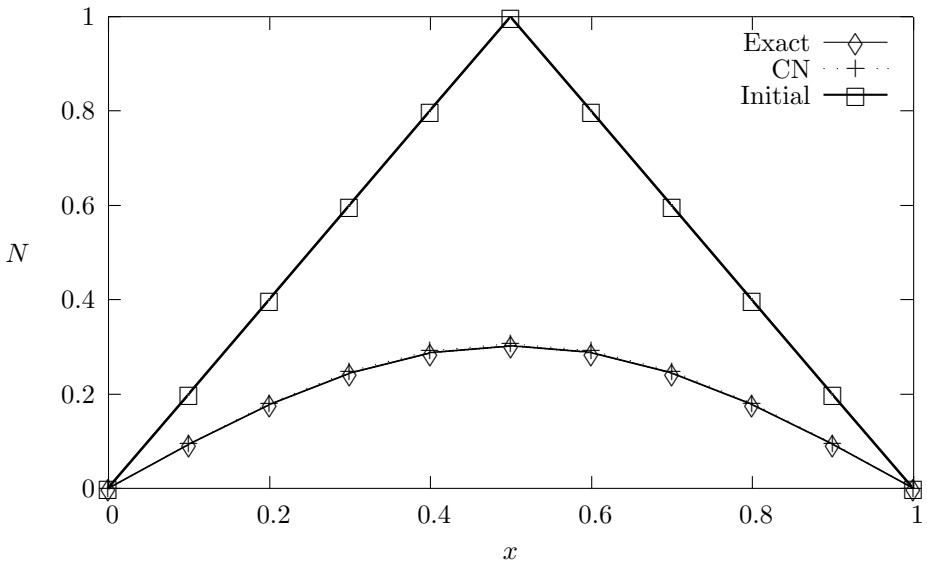

Figure 2.15. The solutions to a test diffusion equation $\frac{\partial N(x,t)}{\partial t} = \frac{\partial^2 N(x,t)}{\partial^2 x^2}$ with Dirichlet boundary condition and a given initial condition (square) by Crank–Nicholson (cross) and analytical (diamond) method.

diffusion. First of all, one-dimensional space was divided to many cells of dimension Δx and the substrate concentration inside each cell was assumed to be uniform. Diffusion equation

$$\frac{\partial N(x,t)}{\partial t} = D\frac{\partial^2 N(x,t)}{\partial^2 x^2} \tag{2.7}$$

was solved numerically to give the number of substrates (N) at time t and in the cell with coordinate x. Among different discretization schemes to approximate equation (2.7), Crank–Nicholson method was chosen [107]. It gave a fairly good result in a test case (figure 2.15). In mathematical language, the discretization of diffusion equation couples different oscillators by adding to the governing differential equation of each oscillator an additional term dependent linearly on the state of other oscillators. In this sense, although the individual oscillator is not modeled here by a differential equation explicitly, the coupling of molecular networks can still be compared to the coupling of neurons. The difference lies in the fact that the coupling term for a neural network is highly abstract and not necessarily an approximation to Fick diffusion. Still, it would be interesting to compare the coupling of neurons to that of molecular networks in future works.

0	1	0	0	1	0	0	1	0

Figure 2.16. The discretization of one-dimensional space into several cells. The meanings of "1" and "0" are clarified in the text.

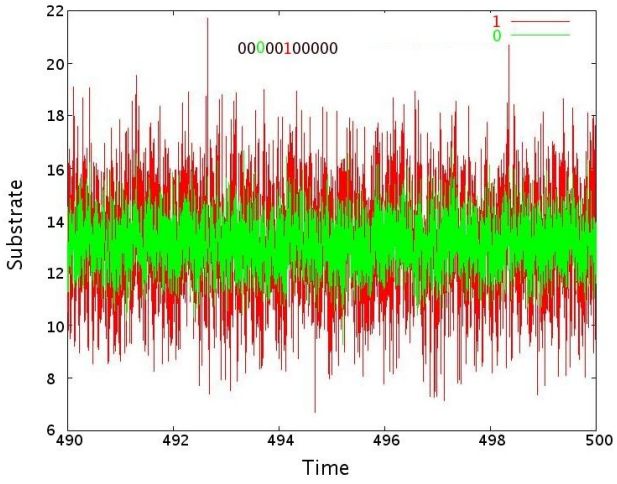

Figure 2.17. The numbers of substrates in compartments with (red) and without (green) enzymes as functions of time (in unit of τ_{enzyme}). One-dimensional space was divided into 11 compartments of either types. Further increase of the number of surrounding type 0 cells did not change the result qualitatively.

In my simulation, the elementary cells of size Δx fell into two kinds labeled by "0" or "1" (figure 2.16) as in section 2.2.3.1. From the property of molecular networks (equation (2.4)) and equation (2.1), it is reasonable to choose $\Delta x \approx \sqrt{D\Delta t}$. The parameters defining a molecular network were the same as those to obtain figure 2.12. In solving the diffusion equation, Dirichlet boundary condition was always assumed. Boundary condition had no effect on the dynamics of type 1 cells as long as the number of type 0 cells is big enough at the two ends.

As the first example, the effect of free diffusion of small molecules into surrounding medium is investigated. In figure 2.17, the numbers of substrates in the molecular network and an enzyme-free compartment are depicted. Due to the diffusion of small molecules into the surrounding medium,

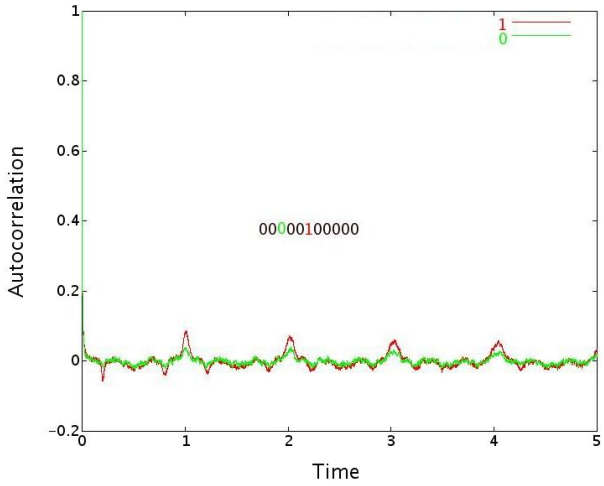

Figure 2.18. The correlation functions of the numbers of substrates in compartment with (red) and without (green) enzymes calculated from figure 2.17. The unit for time is τ_{enzyme}.

one can hardly find any oscillation in the number of substrates.

Another method to show the oscillatory behavior of a function $y(t)$ is to calculate the time correlation function $C(\tau)$,

$$C(\tau) = \frac{\langle (y(t) - \langle y(t) \rangle)(y(t+\tau) - \langle y(t) \rangle) \rangle}{\langle (y(t) - \langle y(t) \rangle)^2 \rangle},$$

where angular brackets denote time average. For a sinusoidal function, its correlation function is still sinusoidal with the same period. Generally the periodicity and amplitude of a correlation function is an indication of the oscillatory component of the original function. For figure 2.17, the corresponding correlation function is shown in figure 2.18 which exhibits the remnant oscillation in the molecular networks. In addition, it is not a surprise that correlation is smaller in the surrounding cells than that in the molecular network.

Furthermore, it is interesting to study the dynamics when more molecular networks are included in the system. In figure 2.19 the correlation functions of substrate numbers in molecular networks are depicted to show the effect of distance between two molecular networks. When they are separated by an appropriate distance, they can reinforce each other to counter the effect of diffusion, as we

can observe that the amplitude of the correlation function reaches maximum when internetwork distance is $4\Delta x$, or, in another work, there are three type 0 cells separating two molecular networks. Here, we are interested in the effect of coupling on the amplitude of autocorrelation functions which indicates the extent to which enzymes in a single molecular network are synchronized (figure 2.19). Additionally, similar to section 2.2.3.1, it is meaningful to study the cross-correlation between two

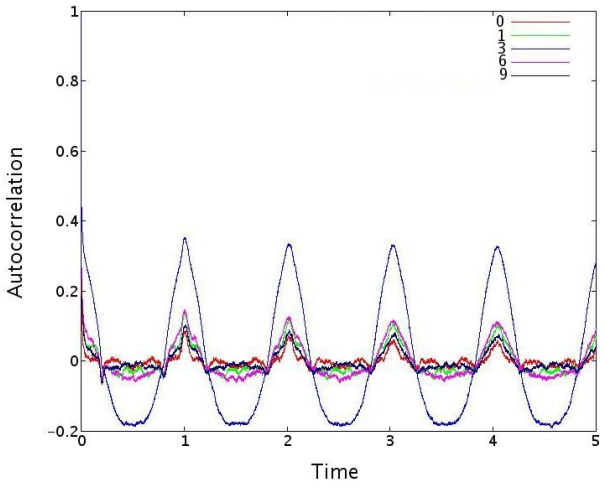

Figure 2.19. The correlation functions of substrate number as functions of distance between two molecular networks. The configuration of the system was similar to figure 2.18 except that there were two molecular networks separated by 1 (green), 3 (blue), 6 (purple), or 9 (black) type 0 cells. Red line is the same as figure 2.18 for comparison. Note that it is the autocorrelation function in one of the two molecular networks in each system that is depicted here. The amplitude of correlation function reaches a maximum when internetwork distance assumes an optimal value indicating the substrate oscillation in the coupled molecular networks can reinforce each other by the diffusion of substrates. The unit for time is τ_{enzyme}.

molecular networks separated by different numbers of type 0 cells. In general, for two time-dependent functions $y_1(t)$ and $y_2(t)$, we may calculate their difference $y(t) = y_1(t) - y_2(t)$ and compare the variance of $y(t)$ $(\sigma_y) = \langle (y(t) - \langle y(t) \rangle)^2 \rangle)$ with the sum of variances of $y_1(t)$ and $y_2(t)$. Here, the ensemble average used to calculate variance is replaced by average over time. The ratio

$$R = \frac{\sigma_y}{\sigma_{y_1} + \sigma_{y_2}} \tag{2.8}$$

should be one for two independent processes y_1 and y_2, and it differs from one if y_1 and y_2 are correlated such that

$$\langle (y_1 - \langle y_1 \rangle)(y_2 - \langle y_2 \rangle) \rangle \neq \langle y_1 - \langle y_1 \rangle \rangle \langle y_2 - \langle y_2 \rangle \rangle = 0, \tag{2.9}$$

where brackets denote average over time. Along this line, we plot in the upper panel of figure 2.20 the variances (σ_1 and σ_2) of the number of substrates in the two molecular networks as functions of the number of type 0 cells in between. These variances reach maximum when two molecular networks are separated by three type 0 cells, because oscillation is more pronounced in this case. The variance σ of the difference between two networks is also plotted. Note that σ is not a maximum when distance is $4\Delta x$. According to equation (2.8), R is calculated and depicted in the lower panel of figure 2.20. R is significantly different from one when distance is 3, suggesting significant correlation between the two molecular networks. On the other hand, when R is not far from one and thus equation (2.9) almost becomes an equality, although it is mathematically insufficient to rule out the correlation between y_1 and y_2, it is still safe to say that there is little correlation between the two molecular networks. In fact, the cross-correlation[1] between the two molecular networks in question is almost zero for large spatial separation where $R \approx 1$ (figure 2.21). Finally, note that the more molecular networks in a system, the bigger the amplitude of correlation functions (figure 2.22).

On the basis of the numerical simulation, one can discuss its biological significance. As mentioned in section 2.2.3.1, the ability of generating and tuning oscillatory signal output is important for biological entities. Using a simple one-dimensional model, we show a possible method to achieve this, namely, simply changing the spatial arrangement of several molecular networks. A similar result was also reported in a different context [126]. This scheme is plausible in that nature does not have to evolve new enzymes to generate qualitatively different signal output, and smart utilization of existing function is usually the trick of nature.

[1]The cross-correlation between $y_1(t)$ and $y_2(t)$ is defined as

$$C(\tau) = \frac{\langle (y_1(t) - \langle y_1(t) \rangle)(y_2(t+\tau) - \langle y_2(t) \rangle) \rangle}{\sqrt{\langle (y_1(t) - \langle y_1(t) \rangle)^2 \rangle \langle (y_2(t) - \langle y_2(t) \rangle)^2 \rangle}}.$$

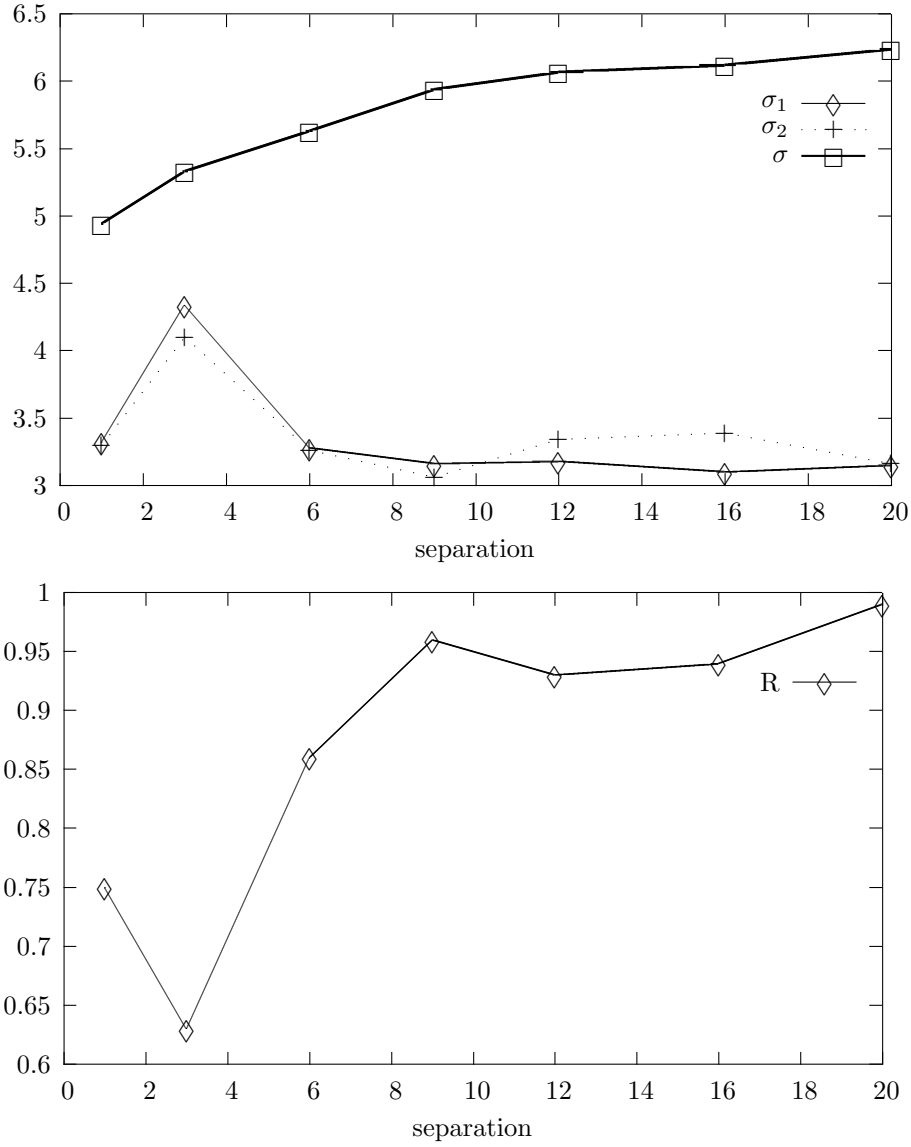

Figure 2.20. Upper panel: the variances of the number of substrates in two molecular networks (diamond, σ_1; cross, σ_2) as functions of their separation and the variance of the difference between the numbers of substrates in two molecular networks (square, σ). Lower panel: the ratio R between σ and $\sigma_1 + \sigma_2$.

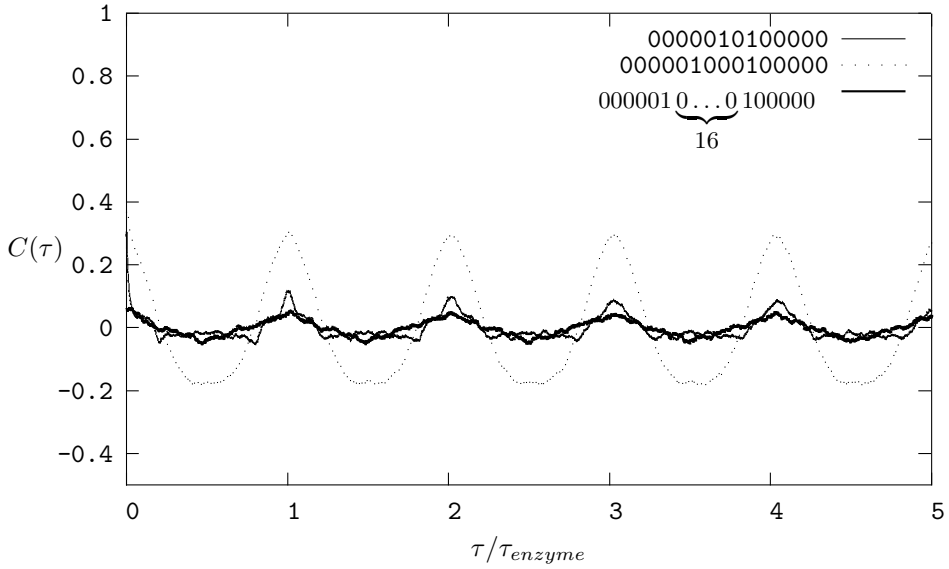

Figure 2.21. The cross-correlation functions (as defined in note 1) between two type 1 molecular networks separated by 1 (line), 3 (dots), or 16 (bold) type 0 cells. When the distance between two networks is too large, there is little correlation between their dynamics.

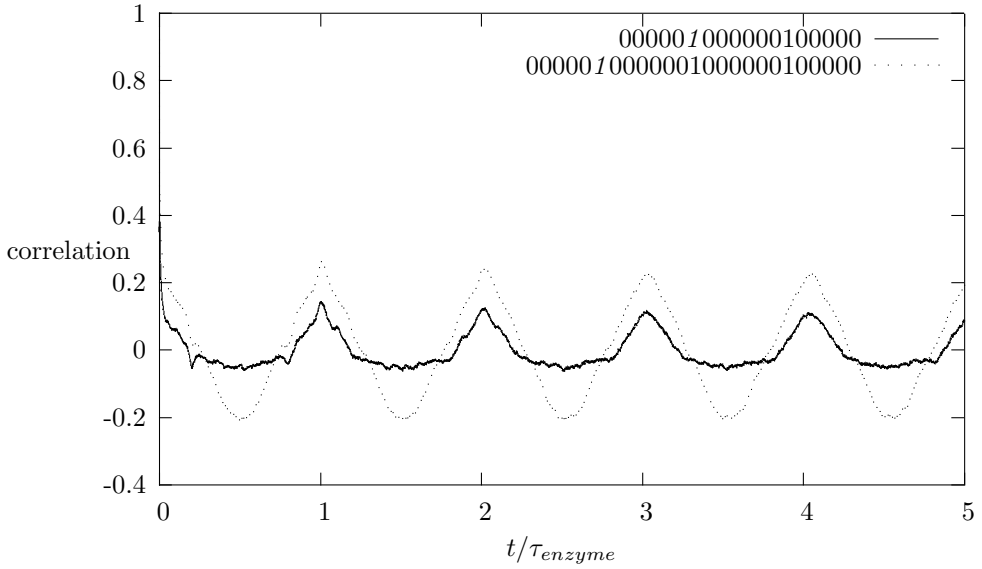

Figure 2.22. The correlation function is dependent on the number (solid, two; dot, three) of molecular networks in the system. The configurations of the systems are also labeled, and the autocorrelation functions of the italicized molecular network are shown.

In summary, this section discusses the coupling of several molecular networks which can also be studied in experiments. Further work will be concentrated on its verification by experiments and generalization to more complex configurations in simulation [14]. These works, however, are constructed on the basis of molecular network. Therefore, it is still important to study other aspects of this model and search for new implications which are significant to biological systems and verifiable experimentally.

2.2.4 Effect of Source Oscillation

Molecular network also makes it possible to control the dynamics of a group of enzymes by external manipulation. Experimentally, many enzymes can be enslaved by pulsed light to act synchronously [49, 50]. Similar to this, in the regime of molecular network, external source of substrate may also serve to control the dynamics of enzymes.

To simulate this effect, the same molecular network as in figure 2.10 is used as a model. In addition to the substrate supply at constant rate ζ, an oscillatory source with rate

$$\zeta_1 = f\left(1 + \cos(\frac{2\pi t}{T})\right) \tag{2.10}$$

is used to enslave the enzymes in the network, where f is the adjustable variable equivalent to the average rate of this oscillatory substrate influx. In real simulation, the number of substrates supplied by this source in an interval dt is generated by a Poisson distribution with mean $\zeta_1 dt$. The period T in equation (2.10) is chosen to be close to the average period without ζ_1.

The results may be analyzed in terms of the number of free enzymes as a function of time. Similar to figure 2.12, the number of free enzymes is still periodic with the existence of oscillatory substrate source. Further analysis reveals two periods in the timecourse of the number of free enzymes (see figure 2.23). This indicates that there are two groups of enzymes in the molecular network. The enzymes in each group behave almost in phase such that they return to the free state (i.e., ready to bind substrate) almost at the same moment. The appearance of a second enzyme group is attributed

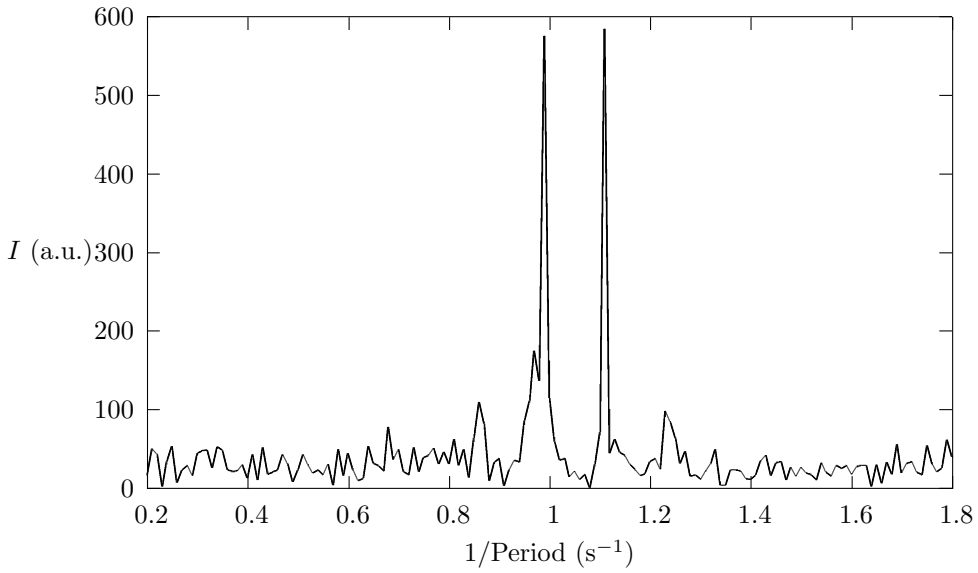

Figure 2.23. The Fourier analysis of the number of free enzymes in a molecular network. Two peaks show up as opposed to one without oscillatory source. In the simulation, $f = 512\ \mathrm{s}^{-1}$, $T = 0.9$ s, and other parameters were the same as figure 2.12 and $\tau_{\mathrm{enzyme}} = 1$ s.

to the oscillatory source without which only one group of enzyme is formed for the system simulated.

The two peaks in figure 2.23 have different origins. One is from the intrinsic oscillation which is independent of the source oscillation, and the other is the result of an external oscillatory substrate source. This is obvious if we pay attention to the positions of these peaks. In figure 2.24, the periods corresponding to intrinsic and external peaks are plotted as functions of f with external period T being equal to 0.9 s. The external peak has the same period as the oscillatory source as expected, but the period of the intrinsic oscillation approaches asymptotically the period under constant source as f is decreased. Furthermore, we plot the ratio of the heights of the two peaks as a function of f in figure 2.25. With the increase of f, the intrinsic peak is weaker compared with the external one. Note that the height of two peaks is almost equal when $f = 512\ \mathrm{s}^{-1}$, although the strength ζ of the constant source is only $200\ \mathrm{s}^{-1}$. This is an indication of the robustness of the intrinsic oscillation. Figure 2.25 also gives a threshold of $4 < f_c < 8$ for the external peak to be observable.

As noticed by others, some biological systems have responses to the changes in thermal noise [105]. In this context, we will study the change of external and intrinsic peaks when the intensity of

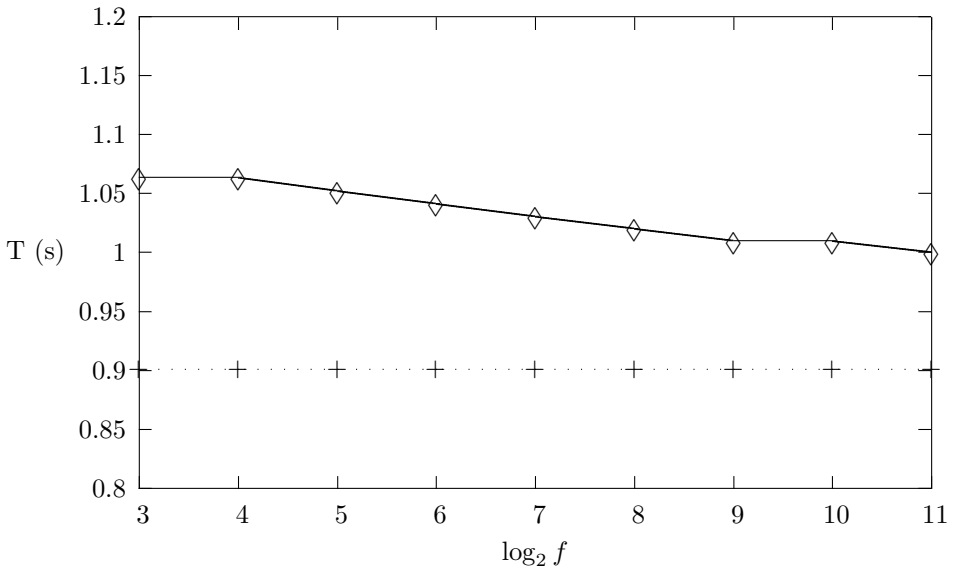

Figure 2.24. The period corresponding to intrinsic (diamond) and external (cross) peak as a function of f. The period of oscillatory source was kept as 0.9 s. As f is decreased, the intrinsic period approaches 1.08 s which is the period when only constant source is used. Different f was used to simulate the dynamics of a molecular network, and the timecourse of the number of free enzymes is Fourier transformed to obtain the positions of peaks. Other parameters were the same as figure 2.23.

noise (equation (2.6)) is varied to see, for example, if there is stochastic focusing [105]. Indeed, as shown in figure 2.26, the height of intrinsic and external peak changes with noise strength, and the ratio between the two can be varied qualitatively by tuning noise strength through, for example, temperature. If we replot figure 2.25 with a different noise strength (figure 2.27), it is obvious that the response of the system to periodic substrate source in terms of the ratio of the two peaks is enhanced by bigger noise intensity. In addition, the maximum in figure 2.26 might also be related to stochastic resonance [32].

The simulation in this section proposes a method to effectively change the collective dynamics of enzymes through the application of an external source of substrate. In addition, it is interesting to ask if nature utilizes this phenomenon to encode the information from a source to some output, because enzyme compartments in the cell may have the property of molecular networks. People have been using the radio wave to transport information for a long while, and the above simulation

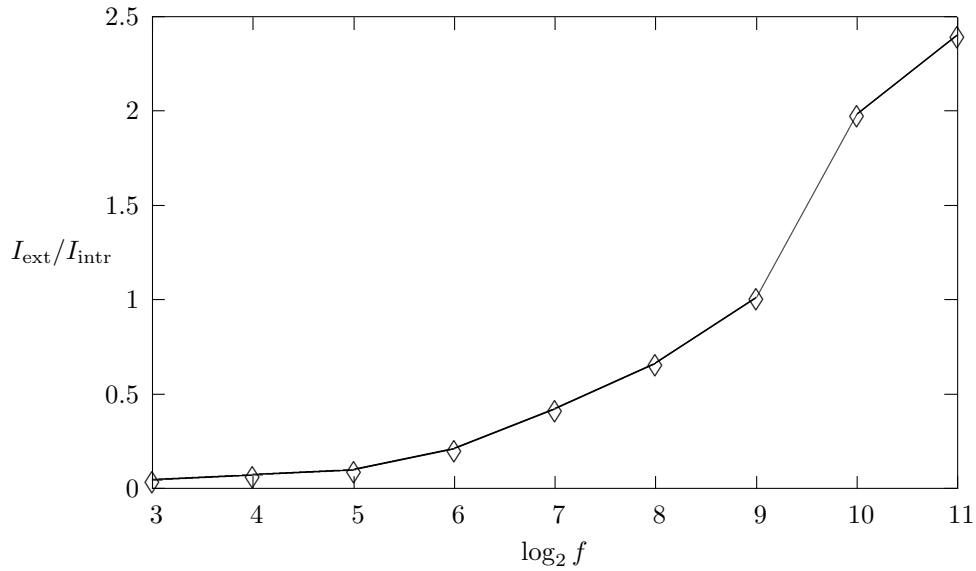

Figure 2.25. The ratio of the height $I_{\rm ext}$ of external peak over that ($I_{\rm intr}$) of intrinsic peak as a function of f. Different f was used to simulate the dynamics of a molecular network and the timecourse of the number of free enzymes was Fourier transformed to obtain the height of peaks. Other parameters were the same as figure 2.23.

shows the possibility for a molecular network to encode and carry the information to other metabolic pathways. Interestingly enough, there is evidence that specificity is realized by enzyme's differential responses to signals of different frequencies [25], so the ability of preserve frequency information should be indispensable to biological systems. Of course, this simulation can and should be subject to experimental verification in the future.

2.3 Statistical Properties of Molecular Collisions

2.3.1 Analytical Result of Off-time Distribution

An intuitive way to study the effect of diffusion on biochemical reactions is to consider the statistical property of molecular collisions which are a prerequisite of all bimolecular reactions. As a first step, let us consider the collision between a mobile particle A and a static particle B (figure 2.28). According to Smoluchowsky theory, the probability of such an event in a small time interval dt is $k_{\rm D}dt$, where $k_{\rm D} = 4\pi r D_{\rm A}/V$, determined by the distance r at contact between the two particles,

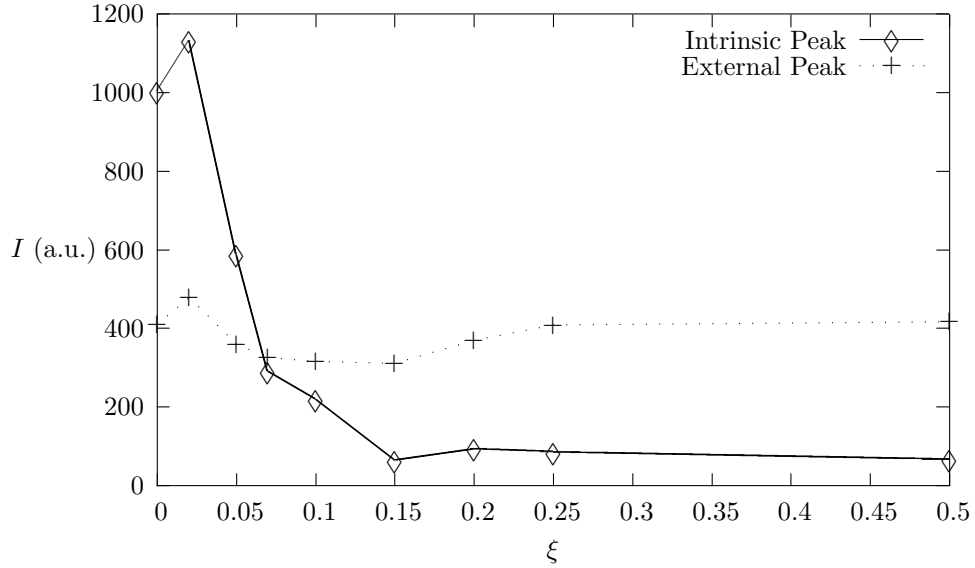

Figure 2.26. The heights (I) of external and internal peaks as functions of noise strength ξ when $f = 128$ s^{-1} and $T = 0.9$ s. Other parameters were the same as figure 2.23.

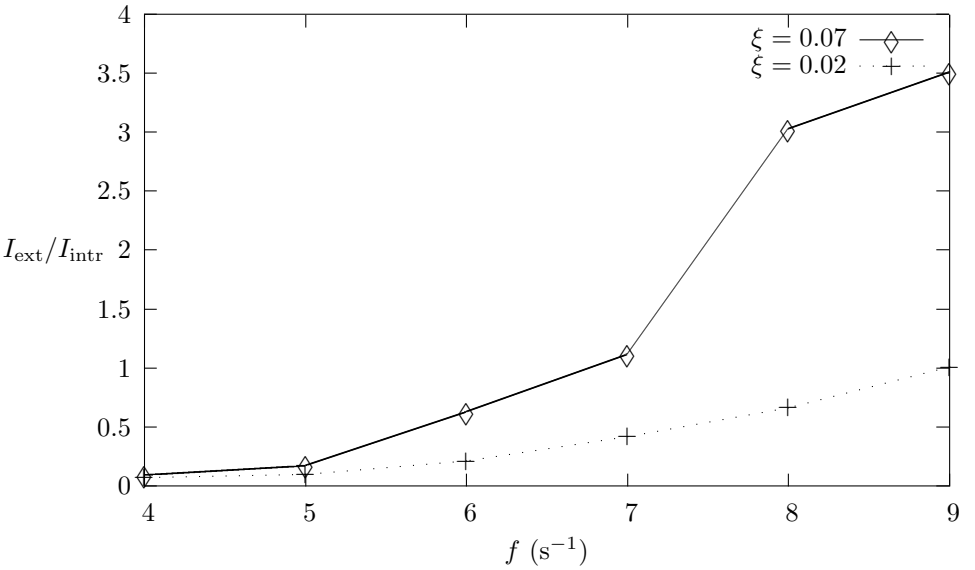

Figure 2.27. The ratio of the height I_{ext} of external peak over that (I_{intr}) of intrinsic peak as a function of f under different noise strength $\xi = 0.02$ or 0.07. Different f and ξ were used to simulate the dynamics of a molecular network and the timecourses of the number of free enzymes were Fourier transformed to obtain the height of interested peaks. Other parameters were the same as figure 2.23.

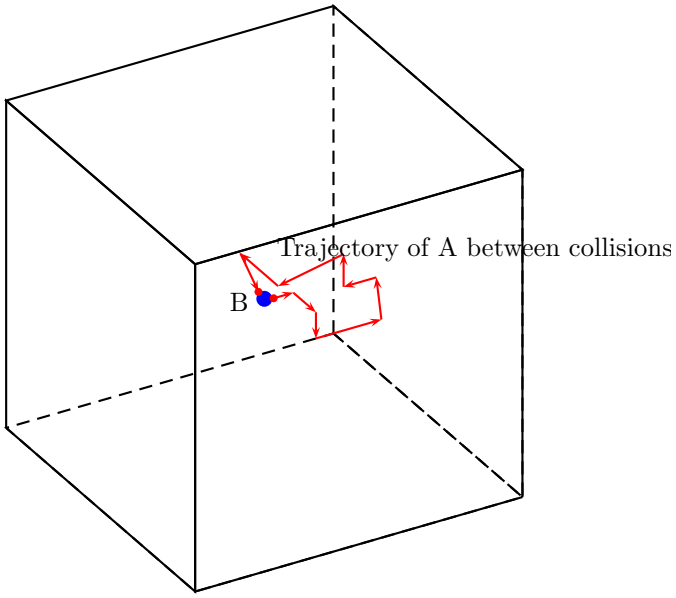

Figure 2.28. The collision between a static particle B (blue dot) and a mobile particle A (red dot) in a cubic reactor of size L.

the diffusion coefficient D_{A} of particle A, and the system volume V. In other words, the off-time t_{off} between consecutive collision events should follow an exponential distribution, or

$$p(t_{\mathrm{off}}) \propto e^{-k_{\mathrm{D}} t_{\mathrm{off}}}. \tag{2.11}$$

A closer look at the process, however, suggests that after a collision event, particle A should have higher probability to collide with particle B than it would if placed far away from particle B [101]. Equation (2.11), in fact, implicitly assumes that the initial position of A is random, that is, particle A has no memory of its trajectory history. The collision–recollision clustering is of important biological consequence. For example, it may be responsible for the rapid recognition of gene sequence by transcription factors [52]. Quantitatively, the off-time distribution scales as $t_{\mathrm{off}}^{-3/2}$ when $t_{\mathrm{off}} \ll V^{2/3}/D$ [111]. The divergence at $t_{\mathrm{off}} = 0$ is consistent with the intuition that the probability of a collision event immediately after the previous collision approaches certainty. Indeed, a numerical simulation verifies this power-law scaling in figure 2.29.

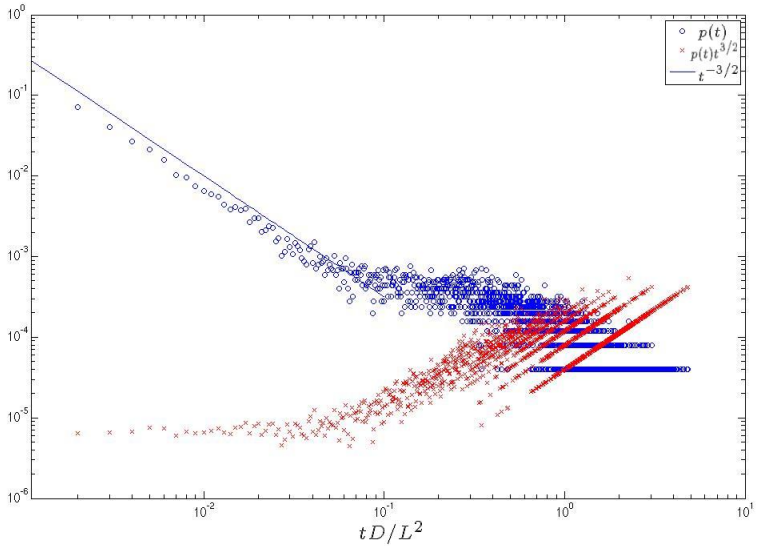

Figure 2.29. The off-time distribution obtained from Brownian motion simulation of the collision between a moving and a static particle in a cubic box of size L (for details, see section 2.3.2). The power-law scaling for small t is indicated by plotting $p(t)t^{3/2}$ as well.

A closely related problem is the collision of a molecule with the boundary of the reactor. Experimentally, one could observe the fluorescence from the transient association of a single Nile Red molecule, confined inside a unilamellar lipid vesicle, with the bilayer wall [33]. The off-time, defined as the dark time between fluorescence events, also follows different distribution in different regimes. To calculate this distribution, we consider the diffusion of a particle inside a spherical reactor with radius R (figure 2.30). Due to the symmetry of this system, the probability distribution c of the particle's position is only a function of its radial position r and time t. The initial condition, as a result, should also exhibit this symmetry as

$$c(r, t = 0) = \delta(r - r_0)/(4\pi r_0^2),$$

where r_0 is the initial position of the particle [111].Here, $c(r, t)$ is the solution to the well-known diffusion equation,

$$\frac{\partial c}{\partial t} = D\nabla^2 c, \tag{2.12}$$

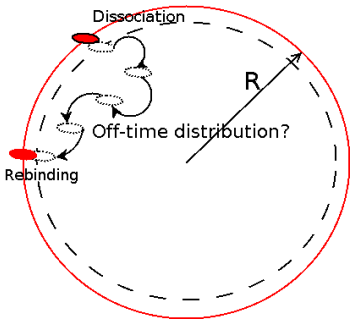

Figure 2.30. The collision between a diffusing particle and the reactor wall.

where D is the diffusion coefficient of particle A. The solution of equation (2.12) can be facilitated by a transformation of variable $u \equiv rc$. The new variable satisfies wave equation, or

$$\frac{\partial u}{\partial t} = D\frac{\partial^2 u}{\partial x^2}.$$

and the following boundary conditions,

$$\begin{aligned} u(r, t = 0) &= \frac{\delta(r - r_0)}{4\pi r_0}, \\ u(r = 0, t) &= 0, \\ u(r = R, t) &= 0. \end{aligned}$$

By using Laplace transformation, one obtains its solution in Laplace space [111],

$$u(r, s) = \frac{\sinh(\sqrt{s/D}r_<)\sinh(\sqrt{s/D}(R - r_>))}{4\pi r_0\sqrt{sD}\sinh(\sqrt{s/D}R)}, \tag{2.13}$$

where $r_< \equiv \min(r, r_0)$, and $r_> \equiv \max(r, r_0)$. The dark time distribution can be identified with the flux out of the absorbing boundary,

$$p(t) = -4\pi R^2 D \left.\frac{\partial c}{\partial r}\right|_{r=R}. \tag{2.14}$$

From equation (2.13), one has

$$c(r,s) = \frac{\sinh(\sqrt{s/D}r_0)\sinh(\sqrt{s/D}(R-r))}{4\pi r r_0 \sinh(\sqrt{s/D}R)}, \tag{2.15}$$

for $r > r_0$. After each collision, the particle starts diffusion from a region very close to the boundary, so $r_0 \lesssim R$. This prompts us to work with a new variable $y \equiv R - r$ which is expected to be much smaller than R. In terms of y, the solution equation (2.15) is written as

$$c(y,s) = \frac{\sinh(\sqrt{s/D}(R-y_0))\sinh(\sqrt{s/D}y)}{4\pi r_0 (R-y)\sinh(\sqrt{s/D}R)}, \tag{2.16}$$

where $y_0 = R - r_0$. The off-time distribution is then evaluated using equation (2.14) and equation (2.16) to be

$$\begin{aligned} p(s) &= \frac{R}{R-y_0}\left[\cosh(\sqrt{s/D}y_0) - \sinh(\sqrt{s/D}y_0)\coth(\sqrt{s/D}R)\right], \\ &= \frac{R}{R-y_0}\frac{\sinh(\sqrt{s/D}(R-y_0))}{\cosh(\sqrt{s/D}R)}. \end{aligned} \tag{2.17}$$

It is instructive to consider two limiting cases of equation (2.17) whose inverse Laplace transforms admit analytical solutions. When $sR^2/D \gg 1$ and $sy_0^2 \ll 1$,

$$\begin{aligned} p(s) &\approx \frac{1}{1-\frac{y_0}{R}}\left[1 + \frac{sy_0^2}{2D} - \sqrt{s/D}y_0\right], \\ &\approx \left(1 + \frac{y_0}{R} + o(y_0^2)\right)\left(1 - \sqrt{s/D}y_0 + o(sy_0^2)\right), \\ &\approx 1 - \left(\sqrt{s/D} - 1/R\right)y_0 + o(y_0^2) + o(sy_0^2), \\ &\approx 1 - \sqrt{s/D}y_0. \end{aligned}$$

This implies $p(t) \propto t^{-3/2}$ when $y_0^2/D \ll t \ll R^2/D$. On the other end of the spectrum when

$sR^2/D \ll 1$,

$$\begin{aligned} p(s) &\approx \frac{R}{R-y_0}\left[1+\frac{sy_0^2}{2D}-\frac{y_0}{R}\left(1+\frac{sR^2}{2D}\right)\right], \\ &\approx 1-\frac{sy_0R}{2D}. \end{aligned}$$

This implies that $p(t) \propto e^{-t/(y_0R/2D)}$ when $t \gg R^2/D$. Interestingly, the scaling behavior of off-time distribution is qualitatively similar to that of the first case we considered. There is some difference, though, when figure 2.29 is compared with figure 2.31 at intermediate t. The algebraic scaling for small t is illustrated in figure 2.31 obtained by numerical inverse of equation (2.17) [165].

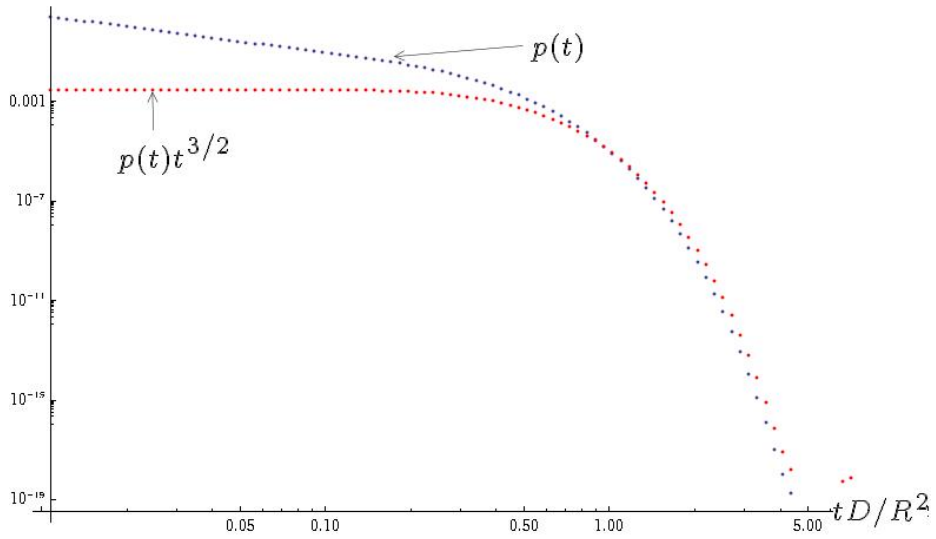

Figure 2.31. The off-time distribution exhibits power-law scaling when $t \ll R^2/D$. Off-time distribution was obtained by numerical inversion of equation (2.17) with $y_0/R = 0.01$.

2.3.2 Numerical Simulation of the Reactant–Reactant and Reactant–Wall Collision

2.3.2.1 Algorithms for Spatial Stochastic Reaction Simulation

Biochemical reactions rarely happen in a well-mixed reactor as assumed throughout section 2.1. Instead, the coupling of reaction, diffusion, and convection gives rise to spatial patterns in the distri-

bution of biomolecules. To resolve the spatial features in reaction network simulation, it is necessary to incorporate mass transport into the theoretical framework. As a first step, diffusion should be accounted for appropriately in the simulation algorithm. There are currently two approaches popular in literature with different emphasis on the discretization of space or time.

Space discretization is the approach to divide the reactor into small compartments where well-mixed condition is assumed to be valid. Diffusion between adjacent compartments is treated as a first-order reaction with rate constant deduced from diffusion coefficient. Although consistent with intuition, it has several practical and theoretical issues to be resolve before gaining wider applicability. First of all, the number of reactions is increased drastically by the inclusion of diffusion steps, although modified stochastic simulation algorithm was proposed to accelerate the process [55]. More importantly, there is some ambiguity in the choice of compartment size. On one hand, if it is too big, diffusion cannot mix reactants thoroughly within each compartments. On the other hand, if it is too small, there would be virtually no chance for bimolecular reactions to take place, because the possibility of both reactants being in the same compartment approaches zero. To solve this problem, people have proposed to modify the reaction rate according to the size of the compartments such that simulation result is less dependent on the fineness of spatial discretization [27].

Temporal discretization essentially simulates the Brownian motion trajectory of each molecule in the system. Different software packages [4, 140] are available to couple the diffusion with biochemical reactions. The spatial resolution of the algorithm is determined by the time step Δt used for simulation as well as the diffusivity of the molecules. Although the diffusion process can be faithfully reproduced, the correct treatment of reaction is not trivial. Recognizing that unimolecular reaction do not have spatial dependence and trimolecular reactions are extremely rare, one only needs to simulate bimolecular reactions appropriately. It is widely accepted that two molecules have to be close enough for reaction to take place and not every close encounter leads to product formation. As such, the interaction radius σ and the probability of reactive collision p (during Δt) are required to simulate bimolecular reactions even in this oversimplified model. Because it is difficult to estimate σ and p from first principle, one has to make the choice by some phenomenological arguments.

The most intuitive one is to stipulate that the effective rate constant calculated according to the

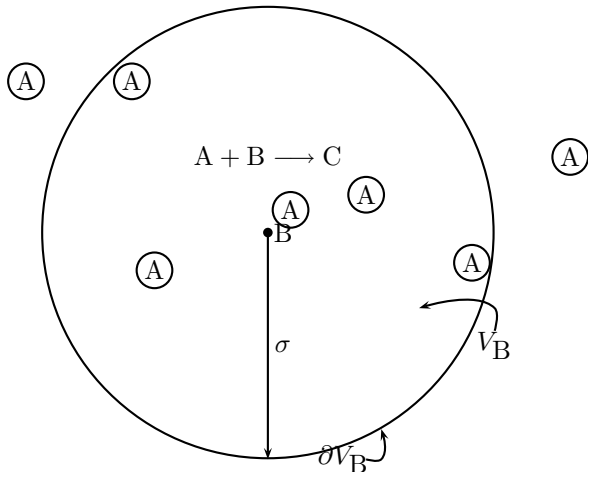

Figure 2.32. The influence sphere V_{B} of B is centered at B with radius σ. Molecule A may react with B if it is within the sphere.

simulation algorithm is consistent with bulk measurement results, which is normally supplied as an input to the simulation. Mathematically, one has to choose Δt, σ and p such that

$$k = f(\Delta t, \sigma, p),$$

where k is the rate constant for the bimolecular reaction of interest with unit m^3/s. The exact functional form of f will be discussed in the context of heteroreaction

$$\mathrm{A} + \mathrm{B} \longrightarrow \mathrm{C}$$

following the discussion in reference [27]. For convenience, we will generally consider the movement of A relative to B. Furthermore, we fix our attention on a single B located at the center of our coordinate system, and A molecules are floating around with an effective diffusion coefficient of $D = D_{\mathrm{A}} + D_{\mathrm{B}}$, where D_{A} and D_{B} are the diffusion coefficients for A and B in lab frame, respectively.

When $\Delta t \to 0$, the simulation approximates the infinitely detailed Brownian dynamics coupled with reaction inside B's influence sphere V_{B} (figure 2.32). The steady-state concentration of A is

the solution to the following reaction–diffusion equation

$$\begin{aligned} D\nabla^2 c &= 0 \text{ for } r > \sigma, \\ D\nabla^2 c - \lambda c &= 0 \text{ for } r < \sigma, \end{aligned} \tag{2.18}$$

where r is the radial coordinate, and $\lambda = p/\Delta t$ is the reaction rate inside the sphere. The reaction rate due to the removal of A can be expressed in terms of the total flux of A through the surface ∂V_{B} of the influence sphere V_{B} as

$$\begin{aligned} \text{Reaction rate} &= \frac{N_{\mathrm{B}}}{V} \int_{V_{\mathrm{B}}} \lambda c \, dV, \\ &= c_{\mathrm{B}} \int_{V_{\mathrm{B}}} D\nabla^2 c \, dV, \\ &= c_{\mathrm{B}} D \int_{\partial V_{\mathrm{B}}} \left. \frac{\partial c}{\partial r} \right|_{r=\sigma} dS, \end{aligned}$$

where N_{B} is the total number of B in a system of volume V and c_{B} is the concentration of B. The solution to equation (2.18) is straightforward, and the resulting reaction rate divided by the bulk concentration of A and B gives the desired expression for k:

$$k(\Delta t \to 0) = 4\pi D \left(\sigma - \sqrt{D/\lambda} \tanh\left(\sigma \sqrt{\lambda/D} \right) \right). \tag{2.19}$$

In particular, if all the collisions are reactive, that is, $p = 1$ or $\lambda \to \infty$, Equation (2.19) reduces to the well-known Smoluchowsky equation $k(\Delta t \to 0) = 4\pi D\sigma$.

When $\Delta t \to \infty$, the simulation process can no longer be described by the reaction–diffusion equation. During Δt, the concentration gradient of A is removed by diffusion. Reactions are simulated at the end of the diffusion step by removing A inside the influence sphere according to probability p. In another word, the reaction rate is proportional to the size of V_{B}:

$$\begin{aligned} \text{Reaction rate} &= p \frac{N_{\mathrm{B}} \frac{4}{3}\pi\sigma^3}{V} \frac{N_{\mathrm{A}}}{V \Delta t}, \\ &= \frac{4}{3}\pi\sigma^3 c_{\mathrm{A}} c_{\mathrm{B}} \frac{p}{\Delta t}. \end{aligned}$$

Here, c_{A} and c_{B} are the bulk concentration of A and B, respectively, so the rate constant is

$$k(\Delta t \to \infty) = \frac{\frac{4}{3}\pi\sigma^3 p}{\Delta t}, \tag{2.20}$$

For intermediate values of Δt, no analytical solution is available yet. The following numerical scheme can be used to correlate k with σ, p, and Δt. Let us consider the effect of diffusion during Δt. Reactions not being simulated in this period, diffusion equation can be used to describe the spatial distribution of A around a single B. To render the equation dimensionless, we scale c by the bulk value c_{A}, r by the interaction radius σ, and t by σ^2/D. The diffusion equation now reads

$$\frac{\partial g(\rho,\tau)}{\partial \tau} = \nabla_\rho^2 g(\rho,\tau), \tag{2.21}$$

where $g \equiv c/c_{\mathrm{A}}$, $\rho \equiv r/\sigma$, and $\tau \equiv tD/\sigma^2$ are dimensionless variables. The boundary conditions are

$$\begin{aligned} g(\rho \to \infty) &= 1, \\ g(\rho = 0) &< \infty. \end{aligned}$$

Our question is to determine the distribution $g(\rho, \tau + \Delta\tau)$ given an arbitrary $g(\rho,\tau)$. This can be achieved by obtaining the Green's function $G(\rho, \rho'; \Delta\tau)$ which is the solution to equation (2.21) subjected to the initial condition $g(\rho, \tau = 0) = \delta(\rho - \rho')/(4\pi\rho'^2)$. As before, the spherical symmetry allows for a convenient change of variable $u \equiv g\rho$, and the differential equation for u,

$$\frac{\partial u}{\partial \tau} = \frac{\partial^2 u}{\partial \rho^2},$$

with initial condition $u(\rho, \tau = 0) = \delta(\rho - \rho')/(4\pi\rho')$ and boundary condition $u(\rho = 0, \tau) = 0$ can be solved to obtained the Green's function. In the end, one has

$$G(\rho,\rho';\Delta\tau) = \frac{1}{\rho\rho'\sqrt{4\pi\Delta\tau}} e^{-\frac{(\rho-\rho')^2}{4\Delta\tau}} - \frac{1}{\rho\rho'\sqrt{4\pi\Delta\tau}} e^{-\frac{(\rho+\rho')^2}{4\Delta\tau}}.$$

The evolution of $g(\rho,\tau)$ can be expressed using Green's function

$$g(\rho,\tau+\Delta\tau)=\int_0^\infty G(\rho,\rho';\Delta\tau)g(\rho')4\pi\rho'^2\,d\rho'.$$

The effect of reaction is to remove molecule A within the influence sphere with probability p. It can be realized before or after the diffusion step. After some iteration, $g(\rho)$ will approach a steady state which satisfies the following equation

$$\begin{aligned} g(\rho) &= (1-p)\int_0^1 G(\rho,\rho';\Delta\tau)g(\rho')4\pi\rho'^2\,d\rho' \\ &+ \int_1^\infty G(\rho,\rho';\Delta\tau)g(\rho')4\pi\rho'^2\,d\rho' \text{ (reaction first)} \qquad (2.22) \\ g(\rho) &= \int_0^\infty G(\rho,\rho';\Delta\tau)g(\rho')4\pi\rho'^2\,d\rho' \\ &- pH(1-\rho)\int_0^\infty G(\rho,\rho';\Delta\tau)g(\rho')4\pi\rho'^2\,d\rho' \text{ (diffusion first)}, \qquad (2.23) \end{aligned}$$

where $H(1-\rho)$ is the Heaviside function. To be self-consistent, the solutions to these two equations should be related to each other by a diffusion step. In fact, equations (2.22) and (2.23) can be rewritten in matrix format if $g(\rho)$ is discretized and then expressed as a column vector $\mathbf{g}=\{g(\rho_i)\}$ where $\rho_i\in(0,\infty)$:

$$\mathbf{g_1} = \mathbf{DRg_1} \text{ (reaction first)} \qquad (2.24)$$

$$\mathbf{g_2} = \mathbf{RDg_2} \text{ (diffusion first)}. \qquad (2.25)$$

Here the effect of reaction and diffusion is accounted for by the operation of matrices $\mathbf{R}$ and $\mathbf{D}$, respectively. Multiplying equation (2.25) with $\mathbf{D}$ from left, one immediately realizes that $\mathbf{Dg_2}$ is a solution to equation (2.24). Indeed, if the solution to equation (2.23) is further evolved by a diffusion step, the result is the same as the solution to equation (2.22) (figure 2.33).

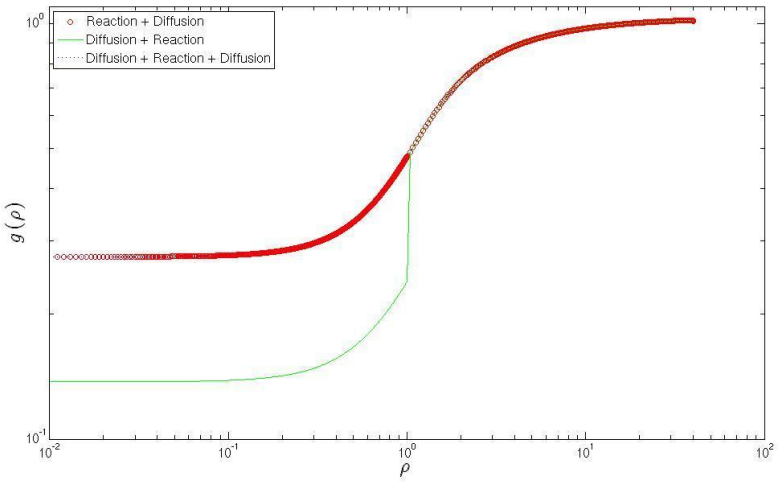

Figure 2.33. The solution to equation (2.22) (red circle, reaction followed by diffusion) and equation (2.23) (green line, diffusion followed by reaction). The latter is further evolved by a diffusion step to obtain the blue dotted line which is equivalent to the solution of equation (2.22). Parameters: $p = 0.5$ and $\sqrt{2\Delta\tau} = 0.5$. Discretization: 1000 points each in $(0, 1]$ and $(1, 40]$ and $g(\rho > 40) \equiv 1$.

The solution to equation (2.22) or equation (2.23) can then be used to compute reaction rate

$$\begin{aligned} \text{Reaction rate} &= \frac{N_{\mathrm{B}}}{V\Delta t} p \int_0^\sigma c_{\mathrm{A}} g(r/\sigma) 4\pi r^2 \, dr, \\ &= \frac{c_{\mathrm{A}} c_{\mathrm{B}}}{\Delta t} p \int_0^1 g(\rho) 4\pi \rho^2 \sigma^3 \, d\rho. \end{aligned}$$

The rate constant is thus

$$k = \frac{\sigma^3 p}{\Delta t} \int_0^1 g(\rho) 4\pi \rho^2 \, d\rho. \tag{2.26}$$

In summary, given p, σ, and Δt, one could solve for $g(\rho)$ from equation (2.22) (or equation (2.23) supplemented by an extra diffusion step) and then k is related to these parameters by equation (2.26). In particular, when $\Delta t \to \infty$, $g(\rho)$ approaches unity, and equation (2.26) reduces to equation (2.20) as expected.

It is also possible to derive such a relation on the basis of other diffusion models. Based on

Table 2.4. Classification of spatial stochastic simulation algorithms

Methods	MCell [140]	Smoldyn [3]	reference [27]
Independent parameter	σ, Δt	$p(=1)$, Δt	Δt, either p or σ
Dependent parameter	p	σ	p or σ

ray-tracing method, MCell [140] uses the following expression

$$\begin{aligned} k &= p\pi\sigma^2\left(\frac{4D}{\pi\Delta t}\right)^{1/2}, \\ &= \sqrt{2\pi}\frac{\sigma^3 p}{\Delta t}\frac{\sqrt{2D\Delta t}}{\sigma}, \end{aligned} \tag{2.27}$$

to correlate p, σ and Δt with k. The last expression (equation (2.27)) suggests that the reduced reaction rate $\kappa \equiv k\Delta t/\sigma^3$ is proportional to p and $\gamma \equiv \sqrt{2D\Delta t}/\sigma$, the latter of which is the root-mean-square displacement of A (relative to B) scaled by σ. This scaling is consistent with the result of Green's function approach [27] when γ is big.

In all of the schemes discussed above, it is not sufficient to fully determine all of the three parameters required for the simulation using a single constraint on k. In practice, user would normally choose Δt first according to the desired temporal and spatial resolution; a rule of thumb is that the spatial resolution scales as $\sqrt{D\Delta t}$. Then either p or σ can be freely adjusted. Available literatures differ in their choices of user inputs as summarized in Table 2.3.2.1.

2.3.2.2 Numerical Results from Smoldyn Simulation

Smoldyn was used to study the collision between reactants or reactant and wall in a confined space. The source code of Smoldyn was slightly modified to report the position and time of each collision event. In a typical simulation, an enzyme, with diffusion coefficient 7×10^{-11} m^2/s, and a substrate, with diffusion coefficient 4.4×10^{-10} m^2/s, were placed randomly in a cubic box. By design, every collision leads to reaction in Smoldyn simulation, so one can conveniently follow the collision between molecules. Figure 2.34(a) shows the positions of the collision between a pair of substrate and enzyme in a 60 nm box. Clearly, some of the collision events cluster at a "hot spot." To determine if they also cluster in time domain, we also plot the time of the collision events in figure 2.34(b). Indeed, the

30,000th to 70,000th collision happen during a short time window of less than 0.5 μs. The collision frequency in this short period of time is much higher than the average collision frequency. This was also reported by others [15]. The close proximity of the molecules to the edge or corner of the reactor is expected to be the reason for the clustering of collisions. If we consider the diffusion of substrate molecule relative to the enzyme, after a collision event the asymptotic probability of the substrate returning to the enzyme for another collision is zero. But if they are temporarily confined by the edge or corner of the reaction, repetitive collision is more likely to happen, and this will have important implications on the reaction rate.

Similar results were also obtained when we considered the collision between a diffusing molecule and the reactor wall (figure 2.35). Repetitive collisions take place in clusters, and this may effectively increase the interaction between the reactor wall and the diffusing molecules. When the reactor size is decreased, this interaction may result in the significant nonspecific adsorption of macromolecules to the wall and change the activity of the molecule due to either denaturation or size-exclusion effect. The efficiency of surface passivation is thus required to be optimized further in micro- or nanoreactors. Alternatively, more frequent interaction between diffusing molecules and the reactor wall may significantly modify the apparent reaction kinetics, as shown recently in the oxidation of Amplex Red catalyzed by horseradish peroxidase confined in femtoliter chambers [48].

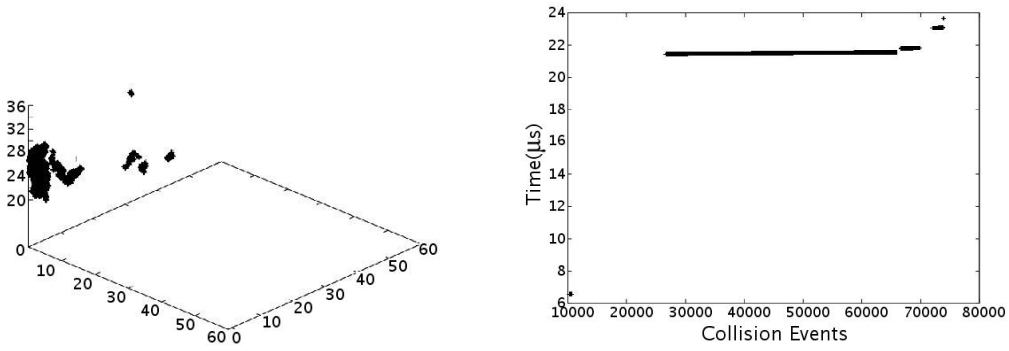

(a) (b)

Figure 2.34. The position (a) and time (b) of the collision events between a pair of substrates and enzymes. The box was 60 nm × 60 nm × 60 nm. The time step was 1.5 ps. The interaction radius was 3.5 nm.

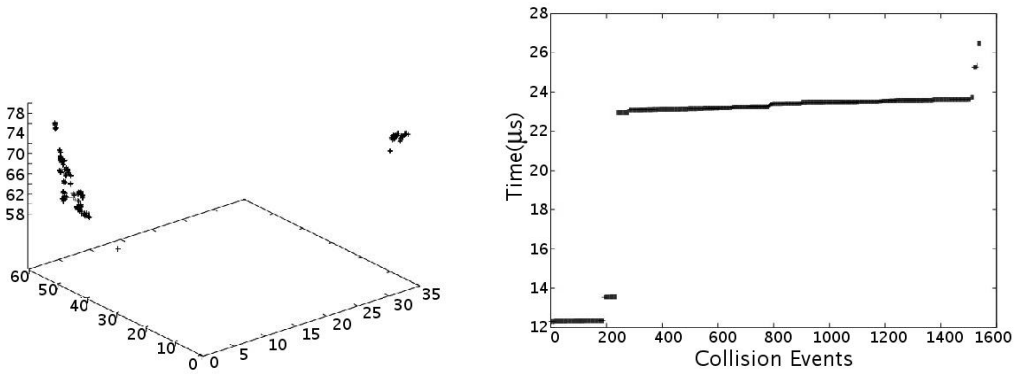

(a) (b)

Figure 2.35. The position (a) and time (b) of the collision events between an enzyme and reactor wall. The box was 100 nm × 100 nm × 100 nm. The time step was 1.5 ps.

Chapter 3

Fast Mixing and Reaction Initiation Control of Single-enzyme Kinetics in Confined Volumes*

Abstract

A device with femtoliter-scale chambers and controlled reaction initiation was developed for single-molecule enzymology. Initially separated substrate and enzyme streams were rapidly mixed in a microfluidic device and encapsulated in an array of individual microreactors, allowing for enzyme kinetics to be monitored with millisecond dead times and single-molecule sensitivity. Because the arrays of chambers were fabricated by micromolding in polydimethylsiloxane, the chambers were monodisperse in size, and the chamber volume could be systematically controlled. Microreactors could be purged and replenished with fresh reactants for consecutive rounds of observation. Repeated experiments with statistically identical initial conditions could be performed rapidly, with zero cross talk among chambers in the array.

3.1 Introduction

Enzymatic reactions are ubiquitous in living systems and are involved in virtually every process related to physiological functioning of the cell. Such reactions usually take place in the ultrasmall volumes of cellular compartments, often with just a few copies of relevant molecules. In vitro

*This chapter is adapted with permission from S.-Y. Jung, Y. Liu, and C. P. Collier, *Langmuir*, 24:4439–4442, 2008.

experimental measurements can be used to simplify complex biological processes by isolating and then correlating the key biochemical factors involved. These measurements are typically performed under ideal conditions, such as in dilute homogeneous solution. However, the biochemical reaction steps that occur in vivo take place under highly nonideal, crowded, and confined conditions in the cell, which can significantly affect their thermodynamic and kinetic properties [99, 121]. To better understand how to infer in vivo dynamics from in vitro experimental measurements, we have fabricated femtoliter-scale biomimic compartments in microfluidics-based devices for capturing real-time single-molecule enzyme dynamics in confined spaces.

Several methods have been reported for interrogating chemical reactions with single-molecule sensitivity in ultrasmall containers such as micelles, vesicles [16, 63], oil-dispersed droplets, and nanoliter to femtoliter wells defined in various substrates such as silicon, polycarbonate [153], and polydimethylsiloxane (PDMS). Etched optical fibers [112, 113] and zero-mode waveguides [81] have also been employed as microreactors. These were typically used to characterize biochemical reaction kinetics at steady state. However, it is also important to have the ability to observe transient behavior of biochemical systems. A common technological challenge in terms of measuring transient dynamics for all these methods is achieving a well-defined zero of time for initiating the reaction in the confined space to monitor kinetics at early times. Ismagilov [130] and Cate [82] have demonstrated very rapid mixing in oil-dispersed aqueous plugs in microfluidic devices; however, the sizes of the plugs were defined by channel dimensions, typically in the tens to hundreds of micrometers range. To the best of our knowledge, single-molecule sensitivity has not yet been demonstrated in these devices.

We have developed a device with millisecond dead times to enable the observation of single-enzyme reactions at early stages as well as at steady state. The microfluidic device that we are reporting here completely mixes reactants (such as enzyme, substrate, and inert biological macromolecules as crowding agents) in about 100 ms and traps them in arrays of femtoliter-scale chambers defined at the interface of a glass coverslip and PDMS [116].

Effective mixing is the main obstacle in reducing the dead time in a microfluidic device. Fluid flows in microfluidics are characterized by low Reynolds number and high Péclet number due to the dimensions of microchannels and flow rates. Under these conditions, diffusive mixing is very slow

and ineffective. Much effort has been devoted to facilitate mixing in this regime [18, 127, 128, 146]. Recently, chaotic advection generated by staggered-herringbone structures in a microchannel [144, 145] was shown to accelerate the mixing of two otherwise colaminar streams. This makes it possible to initiate a reaction with a well-defined time zero and well-mixed initial conditions. Optical lithography was used to fabricate raised features 5 μm in diameter on a master silicon template, which formed cavities in PDMS by micromolding. Each 5 μm chamber had a volume of approximately 100 fL (4.4 μm diameter with 6.5 μm height), as inferred from scanning electron microscopy (SEM) images of the microchambers.

In the device, fluid flowed in an inlet channel which was in registry with the array. A control valve in a second PDMS layer fabricated using multilayer soft lithographic techniques [164] intersected the flow channel in the bottom layer and could be hydraulically actuated (within a few milliseconds) to seal off the flow channel, trapping the liquid in the ultrasmall chambers. The femtoliter chambers were positioned in the field of view of an inverted optical microscope, and fluorescent products from enzymatic reactions were detected using a CCD camera. The excitation source was a mercury–xenon lamp that was attenuated with neutral density filters and controlled by a fast electronic shutter.

3.2 Materials and Methods

Beta-Galactosidase (β-Gal) was purchased from Calbiochem (San Diego, CA), and resorufin-β-d-galacto-pyranoside (RGP) was obtained from Molecular Probes (Eugene, OR). Bovine serum albumin (BSA) and sulforhodamine 101 (Texas Red) was purchased from Aldrich (St. Louis, MO). All chemicals were used without further purification for making aqueous solutions with Millipore 18 MΩ water (Billerica, MA). SU8-2025 and its developer were produced by MicroChem (Newton, MA). SU8-2005 was made by diluting SU8-2025 with cyclopentanone (Sigma Aldrich, St. Louis, MO).

The microfluidic devices were fabricated using multilayer soft lithographic techniques [18] (see the supporting information for details). Solutions were introduced to the microfluidic device by a syringe pump (SP101i, World Precision Instruments, Sarasota, FL) through polystyrene tubing and 23-gauge stainless steel needles (Technical Innovations, Brazoria, TX). The control valve was filled

with 18 MΩ water and deflected downward by compressed air (20 psi) to close the channel and seal the chambers. For leaking and mixing tests, 1 μM Texas Red solution was used in one of the inlets. For enzymatic reactions, 50 μM of RGP solution was reacted with solutions containing 4.5–9 ng/mL β-Gal.

Fluorescence images were obtained on an inverted epifluorescence microscope (Eclipse TE300, Nikon, Melville, NY) equipped with a CCD camera (CoolSNAP-HQ, Roper Scientific, Tucson, AZ) using a 100× oil-immersion objective (NA 1.4). Metamorph software from Universal Imaging Corp. (Downingtown, PA) was used to capture and process images. Captured images were transferred to Adobe Photoshop for further processing. A 200 W mercury–xenon arc lamp (Ushio, Japan) acted as the light source for excitation, and appropriate filter sets (G-2E/C filter combination, Nikon, Melville, NY) were used for Texas Red and resorufin detection. Photobleaching of resorufin during experiments was minimized by utilizing neutral density filter sets (ND 8 and ND 4) and synchronizing the CCD with a Lambda SC smart shutter (Sutter, CA). Resorufin solutions of known concentration were injected into the device and trapped in 100 fL chambers. The fluorescence intensity integrated over the area of a selected chamber showed a linear relationship with the concentration of resorufin. This was used later to calculate the increase of resorufin concentration as a function of time due to enzymatic reactions in chambers of the same volume.

3.3 Results and Discussion

The overall scheme of microfluidic device is depicted in figure 3.1. Substrate and enzyme solutions were introduced from two different inlets and mixed thoroughly after passing through the herringbone mixer. The homogeneous reaction mixture was then trapped in individual microchambers as soon as hydraulic pressure was applied to the control valve to push the chamber layer to the bottom of the channel on the coverslip.

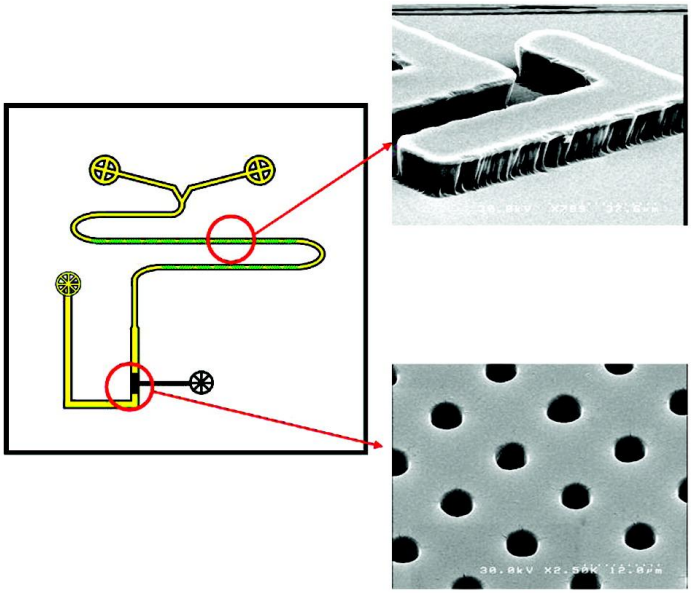

Figure 3.1. Layout of the microfluidic device including mixer, chamber array, and control valve. Inserts: SEM images of mixer mold (top), and array of chambers molded into PDMS (bottom).

3.3.1 Mixing and Encapsulation

Many control experiments to test the suitability of these devices for single-molecule enzymology were performed. The devices containing arrays of 100 femtoliter microchambers were tested with Texas Red solution in pH 7.4 buffer to show the thorough mixing by the chaotic mixer and the absence of leaking from or cross talk among the microchambers in the array. Figure 3.2 illustrates the effect of the chaotic mixer using fluorescence images of the main channel at different positions. Colaminar streams of 1 μM Texas Red solution and buffer-only solution were introduced at the two inlets by the syringe pump at a flow rate of 10 μL/min. The results of the mixing process can be visualized in the subsequent stages of the mixer; by the ninth stage, the flows appeared to be completely mixed. The fluorescence intensity of the homogeneous solution at this location corresponded to a calibrated resorufin concentration of 0.5 μM, which indicated complete mixing quantitatively. At the flow rates used, this occurred within about 140 ms, at which point the mixed flow could be trapped in the chambers by actuating the control valve. This short dead time ensured that early kinetics could be observed in this device.

PDMS is water permeable [124], so careful humidity control was necessary to minimize rapid

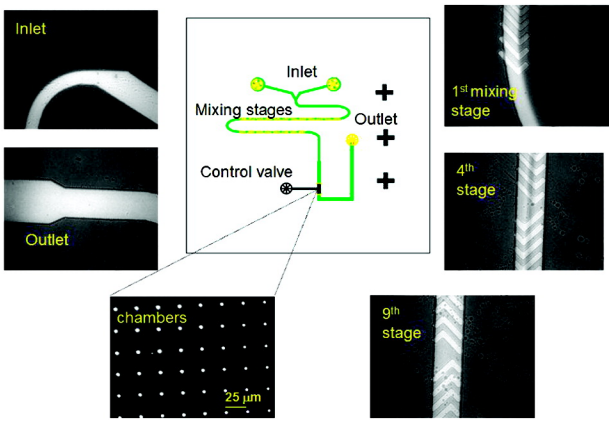

Figure 3.2. Mixing by chaotic advection by herringbone structures in the microfluidic channel. Fluorescence images show progress of mixing at different locations in the channel (arranged in clockwise order, starting with the inlet at the upper left).

evaporation of encapsulated solution in the femtoliter volumes of the chambers. To achieve this, the control valve reservoir located above the microchambers was filled with buffer solution. No sign of evaporation of the solutions in the microchambers was observed for as long as 30 min after the control valve was actuated. To test for cross talk between adjacent chambers due to leaking or diffusion of solute molecules through PDMS, a selected microchamber with Texas Red solution was photobleached by high-intensity light from the arc lamp through a closed iris. After the fluorescent dye in the selected chamber was bleached, recovery of fluorescence intensity was monitored for 20 min. Figure 3.3(d) shows line scans of fluorescence intensity from the chamber taken before (a), right after (b), and 20 min (c) after photobleaching. No fluorescence intensity increase could be observed from the bleached chamber, indicating an absence of cross talk between the selected chamber and its surrounding environment.

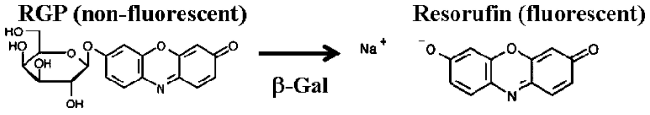

Scheme 3.1. Hydrolysis of RGP substrate by β-Gal to produce fluorescent resorufin.

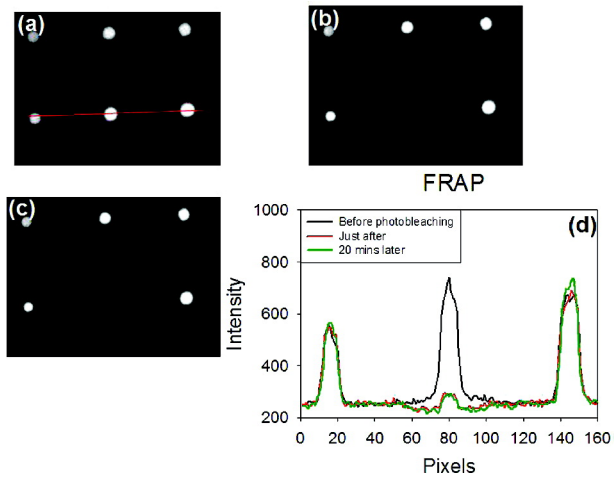

Figure 3.3. Line scans (d) of fluorescence intensity from images of an array of 100 fL chambers containing 0.5 µM Texas Red solution taken before (a), right after (b), and 20 min (c) after photobleaching the lower middle chamber through an iris.

3.3.2 Single-enzyme Experiments

After characterizing the basic properties of the device, enzymatic reactions in the microchambers were carried out as a proof of concept. β-Gal and RGP were used as the enzyme and substrate. Enzymatic cleavage of RGP by β-Gal releases fluorescent resorufin, with galactose as a by-product (Scheme 3.1). Enzymatic activity could be conveniently monitored by the increase of fluorescence intensity with time due to the accumulation of resorufin in the chambers (figure 3.4(a)).

A low concentration of β-Gal (4.5–9 ng/mL) was used such that on average, 0.5 to 1 enzyme would be trapped in each chamber. Figure 3.4(a) shows a typical snapshot of fluorescence intensity in six microchambers taken 60 s after the initiation of enzymatic reactions. After closing the control valve, a distribution of reaction rates was monitored by increasing fluorescence in the chambers. Figure 3.4(b) is a plot of mean product concentrations as functions of time, with associated linear regressions, showing discrete reaction rates corresponding to zero, one, or two enzymes per chamber. Observations of fluorescence intensity were recorded at 60 s intervals using a synchronized electronic shutter to prevent photobleaching and allow for a relatively long period of data acquisition (shutter open time was one second for each measurement). Error bars correspond to $\pm$ one standard deviation from the mean. The linear correlation coefficients for the fitted lines were 0.9946 (zero enzymes per

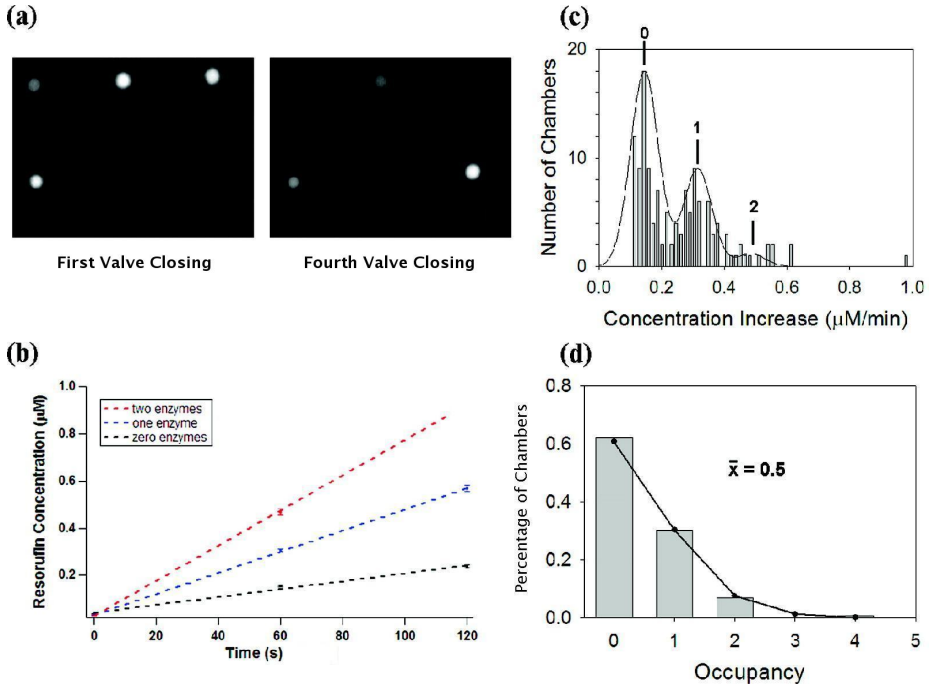

Figure 3.4. Enzyme reactions in microchambers. β-Gal concentration was 9 ng/mL (one enzyme per 100-femtoliter chamber on average) with 100 μM RGP for (a), and 4.5 ng/mL (0.5 enzymes per 100-femtoliter chamber on average) with 100 μM RGP for (b)–(d). Chambers were coated with 10 mg/mL BSA before experiments to minimize nonspecific binding of enzymes onto PDMS wall. (a) Fluorescence images of chambers taken 60 s after the initiation of enzymatic reactions. Subsequent opening and closing rounds of chambers by the control valve show no memory effect, which indicates negligible nonspecific adsorption of enzymes onto the chamber wall. (b) Mean product concentrations as functions of time, with associated linear fits, showing discrete reaction rates corresponding to zero, one, or two enzymes per chamber. Error bars correspond to ± one standard deviation from the mean. (c) The histogram of the fluorescence increase for 132 chambers was binned to groups corresponding to zero, one, or two enzymes in a chamber. (d) The percentage of chambers (bar) containing zero, one, or two enzymes agreed with a Poisson distribution (line) with a mean value of 0.5.

chamber), 0.9999 (one enzyme per chamber), and 0.9999 (two enzymes per chamber). The raw data from 395 independent measurements associated with this plot are included in the supporting information.

A histogram of the fluorescence increase for 132 chambers was binned to groups corresponding to zero, one, or two enzymes per chamber (figure 3.4(c)). The percentage of each group can be described

by a Poisson distribution with a mean value of 0.5 (figure 3.4(d)), as expected from the enzyme concentration employed. The initial rate of product molecule formation, 243 ± 30 resorufin per enzyme/s, was consistent with bulk stopped-flow and steady-state measurements (288 ± 33 resorufin per enzyme/s), performed by us (see the supporting information), and others [26]. When successive opening and closing rounds of the chambers were performed by actuating the control valve, the distributions changed, indicating that the enzymes were not surface bound, but free in solution. Importantly, the initial rate of reaction in different chambers remained roughly the same. This suggests that their catalytic activity was not affected by nonspecific adsorption to the chamber walls, which had been passivated with high concentrations of BSA (10 mg/mL) for 1 h before the measurements. This was corroborated by another control experiment where the enzymes were flushed out of the chambers, and then the solution containing only substrate but no enzymes was trapped. No fluorescence increase was detected over background levels due to weak autohydrolysis of the substrate.

Our device enables rapid gathering of kinetics data on the same chip, so it is especially useful for single-molecule studies where dynamic [88] or static [153] disorder must be thoroughly explored by analyzing a statistically significant ensemble of experiments. This can be achieved by flushing out the old reaction mixture from the chambers at the conclusion of a measurement with fresh, well-mixed solution of enzyme and substrate for 15 min. This flushing procedure resulted in no observed memory effects in reaction kinetics in the microchamber from one run to the next. Statistically independent reaction kinetics could be observed from the same chamber with each closing of the control valve.

3.4 Summary and Conclusions

A microfluidic platform combining rapid mixing and controlled reaction initiation in femtoliter-volume microreactors was developed and tested. As a proof of concept, single-enzyme reaction kinetics was measured with the device. Control experiments established the effective isolation of each microchamber from its neighbors in the array, without memory effects from previous experiments.

These devices enable access to early kinetics of single-molecule experiments, in addition to steady-state kinetics, made possible by a judicious combination of well-established microfluidic techniques.

It is straightforward to change the dimensions or contents of the chambers to mimic various features of real cellular compartments. For example, one could introduce inert crowding agents, such as BSA, to study the effect of molecular crowding on reaction kinetics [99]. To study the significance of geometric constraints [152], chambers of different shape, size, or topology may be fabricated in the same way. In particular, chambers smaller than 1 μm, from molds fabricated with electron-beam lithography, would provide spatial confinement on a scale matching confocal microscopy, without the need for surface chemistry to immobilize enzymes, which has been shown to affect reaction rates [100]. The microenvironment in a chamber could be further tuned in the time domain, through temporal control of solute concentration by adjustable osmosis between the aqueous compartments of the chamber and the control valve reservoir [124]. With the use of a passive chaotic mixer on chip, mixing is complete within 140 ms, which makes transient as well as steady-state behavior accessible for observation. This feature is especially suitable for biological studies where transient, nonequilibrium phenomena are ubiquitous. Furthermore, with the introduction of connecting channels among chambers, one would be able to study the diffusion-mediated coupling of individual reactors and accompanying emergent behavior such as spatial wave generation and pattern formation [14]. These devices represent the beginning of the fabrication of model systems that can be used to systematically track, in a general and quantitative way and with single-molecule sensitivity, the transitions in enzyme kinetics from ideal, in vitro experimental conditions toward the greater complexity found in living cells. Our system can be useful for other interesting questions as long as fluorescence can serve as a readout signal. For instance, the unfolding of single freely diffusing RNase H could be studied in our system to complement steady-state, spFRET measurements on surface immobilized enzymes [78] to reveal the early stages of protein conformational changes in confined biomimetic environments.

Each one of the chambers in the array was virtually identical in terms of size and shape, and may be thought of as an independent reactor. The number and density of chambers in an array can be increased significantly with submicrometer chambers fabricated with electron-beam lithography.

This will enable the acquisition of large numbers of measurements quickly, not only by observing many chambers in an array simultaneously, but by multiple repeated measurements on the same array (because the chambers can be flushed out and reused). This will allow a better statistical sampling of the distributions of kinetic behaviors in enzyme catalysis in confined and highly nonideal, but physiologically more realistic, nanoenvironments.

Acknowledgment

The authors thank Alireza Ghaffari at the Micro–Nano Fabrication Laboratory at Caltech for help with microfluidic device fabrication.

Supporting Information

Photolithography

PDMS molds were fabricated with multilayer photolithographic techniques. Briefly, negative tone photomasks for the control and mixer layers were printed on transparency films at 20,000 dots per inch resolution by CAD/Art Services (Bandon, OR). A chrome mask with arrays of 5 μm dots was purchased from MEMS and Nanotechnology Exchange (Reston, VA). To make the mold for the mixer–chamber layer, SU8-2005 was first spun at 2000 rpm on a piece of silicon wafer cleaned by 2-propanol. After soft baking (1 min at 65 ℃ and 2 min at 95 ℃), the 5 μm dot arrays as well as alignment marks were transferred from the chrome mask to the resist by UV exposure at 4.5 mW/cm^2 for 90 s, followed by post exposure baking (1 min at 65 ℃ and 1 min at 95 ℃), and development in SU8 developer. Patterns of 5 μm dots were further stabilized by hard baking at 150 ℃ for 5 min. Each 5 μm chamber had a volume of approximately 100 femtoliters (4.4 μm diameter with 6.5 μm height), as inferred from scanning electron microscopy (SEM) images of the microchambers. Another layer of 25 μm thick SU8-2025 photoresist was then spin coated on top of the dot pattern and soft baked (1 min at 65 ℃ and 3 min at 95 ℃). To align the staggered-herringbone mixer patterns relative to the array of dots, four corners of the silicon chip were carefully cleared with SU8 developer

to reveal the alignment marks on the mold. The mixer patterns were then transferred to the second resist layer through the transparency mask by UV exposure at 4.5 mW/cm^2 for 1 min. After post exposure baking (1 min at 65 ℃ and 3 min at 95 ℃) and development in SU8 developer, the patterns were hard baked at 150 ℃ for 5 min. The mold for the control layer was made separately in a similar manner using single-step photolithography. The main channel layer was also made using SU8-2025 photoresist. A piece of clean, dry # 1 coverglass (Fisher Scientific, Pittsburgh, PA) was coated with a uniform layer of 35 µm thick SU8-2025. After soft baking (1 min at 65 ℃ and 3 min at 95 ℃), the coated coverglass was exposed to UV illumination under the transparency mask for the channel layer at 4.5 mW/cm^2 for 1 min. Post exposure baking and development in SU8 developer revealed negatively defined channels in resist layer on the glass coverslip.

Multilayer Soft Lithography and Device Assembly

The final device consists of three layers: a main channel layer (bottom), an intermediate mixer–microchamber layer (middle) and a control layer (top). The top two layers were assembled using multilayer soft lithography [164]. Before application of the PDMS elastomer, all of the silicon molds were treated with chlorotrimethylsilane vapor for 5 min to prevent strong adhesion between the elastomer and photoresist after curing. The elastomer used in this experiment was RTV 615 from General Electric Silicones. A silicone elastomer mixture with excess polymer base (20:1 mass ratio of polymer base and curing agent) was spin coated onto the microchamber–mixer mold at 2400 rpm for 60 s and cured in an oven at 80 ℃ for 45 min. The control layer was prepared by pouring silicone elastomer with deficient polymer base (5:1 mass ratio of polymer base and curing agent) onto the control layer mold and baking at 80 ℃ for 45 min after the elastomer was degassed. The control layer was peeled from the mold and aligned with the PDMS coated microchamber–mixer mold. The two-layer PDMS assembly was then baked for two hours to bond the two layers together into a single structure which was then peeled from the microchamber–mixer mold. The gradient of curing agents at the interface of the two layers drives their migration from the top layer to the bottom, ensuring that the two layers are strongly bonded together by covalent cross-linking at the interface [164]. Finally, the bottom layer and top two layers were activated by oxygen plasma cleaning (plasma

cleaner PDC-32G, Harrick Scientific Corp., Ossining, NY) and bonded together by heat treatment in an oven at 80 ℃ overnight.

Stopped-flow Measurements

The kinetics of reference β-Gal–RGP reactions in bulk solution was monitored with a stopped-flow instrument (SX.18MV, Applied Photophysics, Surrey, UK). Final concentration of 0.19 nM β-Gal with 100 µM of RGP was mixed and the fluorescence increase due to the enzymatic generation of resorufin was measured. A typical plot of resorufin concentration increase as a function of time is shown in figure 3.5. The mean and standard deviation from five measurements gave the initial rate of resorufin formation as 288 $\pm$ 33 resorufin per enzyme/s, which is close to the rate from a single enzyme in a 100 fL chamber: 243 resorufin per enzyme/s.

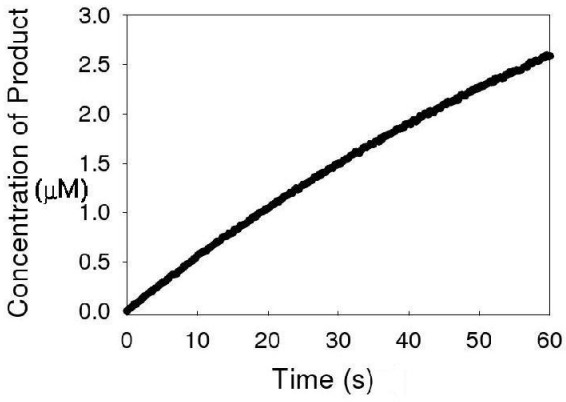

Figure 3.5. Bulk measurement of β-Gal enzyme activities by a stopped-flow instrument.

Chapter 4

Enzymatic Reactions in Femtoliter Droplets

4.1 On-chip Generation and Manipulation of Water Droplets

4.1.1 Introduction

The development of micro- and nanofluidics makes it possible to achieve an exquisite control of flow at microscale. It is thus natural to explore the possibility of putting the biomimetic compartments into microfluidic devices and to study their property individually under precisely defined conditions. The first step is the generation of the desired microreactors on demand. Second, we would like to process the information in each of them with high throughput and selectivity.

A lot of effort has been made to develop methods to generate phospholipid vesicles on chip [30, 155]. More attention has been paid to the application of two-phase immiscible system in microfluidics. Air bubbles in water, water-in-oil, or oil-in-water droplets have been the focus of a lot of groups recently (for reviews, see references [129] and [20]). With the help of suitable surfactants, micron-sized compartments can be generated and stabilized in microfluidic devices. Due to the discrete distribution of the objects of interest, this area is named "digital microfluidics." The advantage of digital microfluidics includes the high uniformity of objects' size distribution, the precise control of the microenvironment, the possibility of multiplexing and parallelization, and the small amount of reagent consumption.

In the context of biochemical investigation, water-in-oil droplets is of special attention. It is

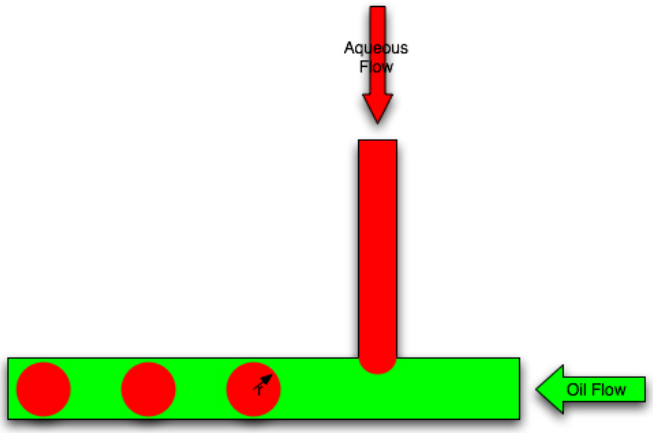

Figure 4.1. The formation of water (red) droplets in oil (green) in a microfluidic channel. Top view is shown above and the cross section of the channels could be rectangular or rounded.

straightforward to generate these droplets in a microfluidic channel. The simplest design is a T-junction where aqueous solution is injected into the flowing carrier oil which is immiscible with water. Figure 4.1 illustrates a typical T-junction for droplet generation. There are, however, a few issues to be concerned with when we wish to incorporate them into microfluidic devices as biomimetic reactors:

- The size of water droplets is still larger than typical prokaryotic cells or compartments in eukaryotic cells.
- The high flow rate in a microfluidic channel makes prolonged observation on the same droplet impossible if flow is not stopped; the generation of droplets is not decoupled from other functions of the device.

The main obstacle to the optimization of digital microfluidic devices is the lack of realistic physical models with predictive power. Two-phase flow involves the nonlinear interaction of surface tension and shear force. This is further coupled with the mass transfer of bulk phases and surfactants. The resulting coupled nonlinear partial differential equation can only be tackled by numerical methods [21, 22, 94]. Take droplet generation as an example, to model the process in full detail, one has to resolve the fine structure of the breakup point between the forming droplet and the bulk phase. This region becomes so small that the usual continuum approach to the problem is fundamentally

defective [141]. One essentially is confronted with a problem with vastly different scales.

Qualitative models, however, may still prove helpful in some cases. Talyor [156] suggested that the size of the droplet be determined by a dimensionless number reflecting the relative strength of shear stress with respective to surface tension. It is defined as

$$Ca = \mu\epsilon r/\gamma,$$

where μ is the viscosity of the carrier fluid (oil), ϵ is the shear rate in the channel, r is the radius of the droplet and γ is the surface tension between the two phases, that is, oil and water. Assuming that the droplets form as the result of balanced surface tension and shear force, Ca should be $O(1)$, implying

$$r = \gamma/\mu\epsilon.$$

This relation makes physical sense at least qualitatively. When the carrier fluid is more viscous, shear force is larger with the same shear rate, and the droplet has to assume a smaller radius to generate a comparable Laplace pressure. Alternatively, with a smaller surface tension, it is easier to generate smaller droplets because the penalty due to increased surface area is not so significant. Another model, provided by Whitesides and Stone, pays special attention to the geometric constraints inherent in a T-junction. To be specific, the periodic blocking of the oil flow by the aqueous streams generated a slightly higher positive backpressure in the oil channel, which swept the aqueous plug down the main channel, allowing the process to be repeated [22, 36].

With the help of available physical models and intuition, people have experimented with various clever designs to overcome the above-mentioned obstacles. For example, in order for the droplet size to reach micron or even submicron regime, a recycling channel was included to accumulate those tiny satellite droplets generated as a by-product [154]. In another study, a docking mechanism was developed to store droplets at specific positions for further prolonged treatment [124].

Here we report our result in the development of an integrated microfluidic platform with the ability of stable generation and simultaneous observation of selected micron-sized droplets.

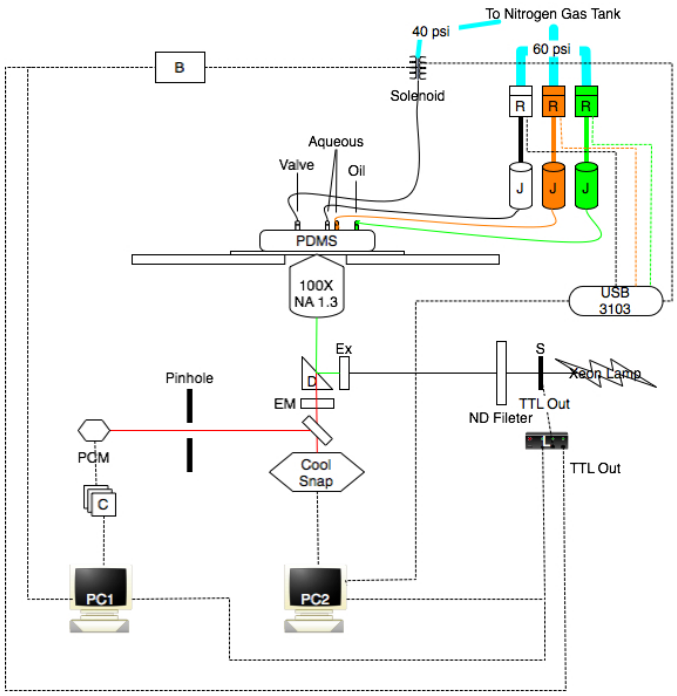

Figure 4.2. An integrated platform for digital microfluidics. For details, see text.

4.1.2 An Integrated Platform for Digital Microfluidics

Figure 4.2 shows the setup of our microfluidic workstation. A piece of PDMS device was fixed onto a microscope stage for epifluorescence and bright-field observation with 100X NA 1.3 objective. To feed fluids into the device, compressed nitrogen with pressure controlled by three different regulators (R) was injected into Teflon jars (J) containing aqueous solution (white or orange J) or oil (green J). Fluids entered the device through Tygon tubing and 23-gauge stainless needle. A critical function of the device is the ability of stopping the movement of droplet for prolonged observation. This was achieved by applying a pressure of 40 psi, managed by a solenoid valve, to the control port. The aqueous droplets usually contained fluorophores excited by a mercury–xenon lamp for fluorescence microscopy. After passing through a set of ND filters and excitation filter, the excitation light was deflected by a dichroic mirror (D) and then collimated by the objective onto the sample, and the resulting fluorescence was collected by the same objective, cleaned by emission filter, and finally recorded by a cooled CCD camera (Cool Snap). For measurements of higher time resolution, a photon-counting module (PCM) was employed to measure the photon flux due to emission. A

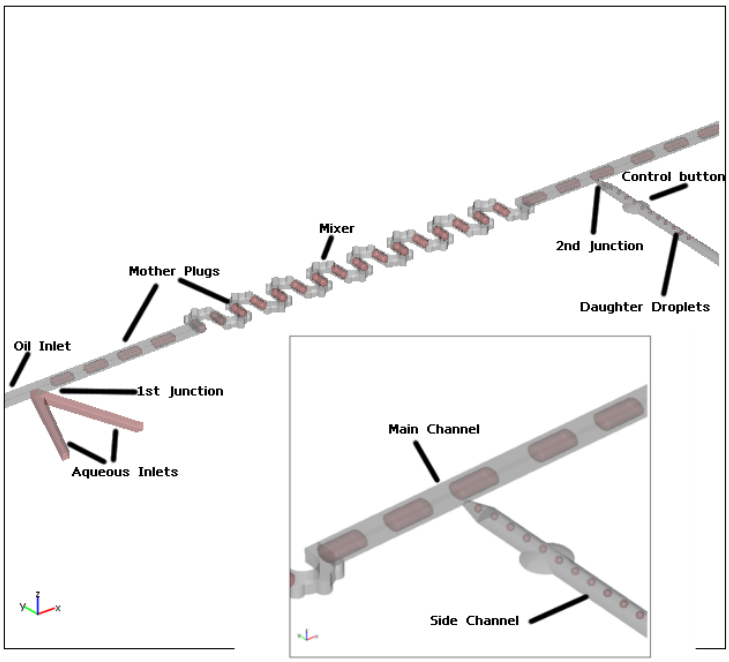

Figure 4.3. Layout of microfluidic devices.

mechanical shutter (S) was added between ND filter and light source to reduce photobleaching of fluorophores. The whole system was controlled by two computers (PC1 and PC2). PC1 was responsible for the collection and analysis of photon-counting data, and PC2 was mainly devoted to the control of Cool Snap. Both PCs had their own mechanism to operate the shutter via SC Lambda controller (L) and solenoid valve via a home-built relay board (B) (for details, see section 4.1.3).

The layout of the device is rendered in figure 4.3. Two aqueous inlets introduced reactants into the oil phase to form mother plugs. Reaction mixture was mixed in the chaotic mixer before daughter droplets were splitted from mother plugs at the second junction. Pneumatic pressure could stop the movement of daughter droplets by sealing the side channel at the control button. Other parts of the device was not affected by this action, so new droplets were generated in the side channel once the control button was released again.

4.1.3 Instrument Control and Data Acquisition

All the electronic components in figure 4.2 were controlled by home-built softwares with graphical user interface (GUI) written in either Matlab 2007b or Labview 8.5. Matlab is a scripting language widely used in physics and engineering for its extensive computation library. It has sufficient support for GUI construction, but users have to modify the code to suit their needs. As such, a basic understanding of object-oriented programming is required. The learning curve, however, is not as steep as it seems. Furthermore, it is easy to incorporate complicated data processing routines into a new program. Labview, in contrast, offers a programing environment without the need of code writing. Labview is specially designed for instrument control and there is a huge library of device drivers for end users. However, one has to call Matlab or other languages for involved computational tasks.

The control signal widely used in our study was variable or binary DC voltage. We used a USB analog output board (USB-3103, Measurement Computing, Norton, MA) to generate required voltage ranging from 0 to 10 V with 16-bit resolution. Not all instruments had an ideal interface ready to take the signal source, so some basic electronic shop techniques were applied to build some simple circuit boxes.

Metamorph was used to save the images captured by Cool Snap. Data from the photon-counting module was acquired by a digital counter on a PCI-6014 multifunction data acquisition board (National Instruments, Austin, TX) which is controlled by Labview.

The following subsections give the details of the instrument control and data acquisition systems.

4.1.3.1 Pressure Regulator

A precise control of the gas pressure applied to the solution jars is essential to the establishment of balanced flow and fine tuning of droplet size. One Marshal-Bellofram pressure regulator (Series 2000) was dedicated to each fluid jar to achieve independent control of the flow rates in different inlets. 60-psi nitrogen gas was supplied to the regulator, and the output gas pressure was controlled by DC voltage ranging from 0 to 10 V with a resolution of less than 0.5 mV. The voltage was conveniently generated by USB-3103 according to user's specification. A Matlab program was written with a

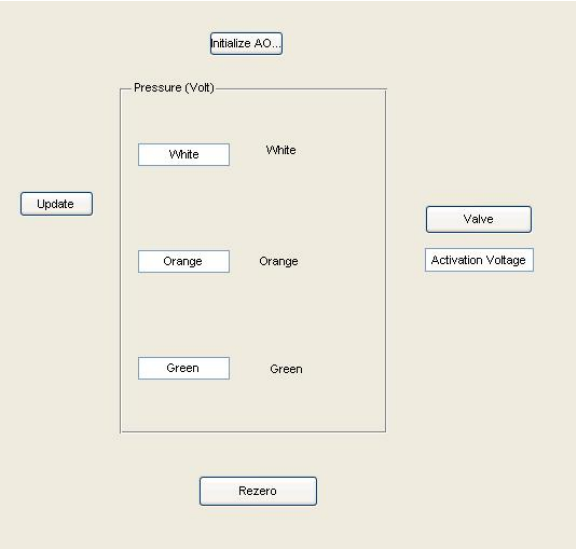

Figure 4.4. The user interface of the Matlab program to control pressure regulators.

user interface as in figure 4.4. In our system, there were three color-coded inlets: white, orange, and green. The white and orange inlets were aqueous channels, and the latter was usually dedicated to the one with fluorescent solutions. The green inlet was reserved for oil phase. To use the program, one first click the "Initialize AO" button to establish a connection between the computer and USB-3103. After typing desired voltages into the corresponding boxes, clicking "update" would generate the voltage signal and induce flow. A button "rezero" stopped all the flow by resetting the voltages to zero. A more advanced version of the control program is shown in figure 4.5. In addition to live monitoring of output voltages, a slow update function was implemented to reduce the pressure "shock" when big changes of voltage had to be made. This was achieved by specifying the step size and total duration for the voltage update.

4.1.3.2 Photon Counting Module

The output of photon-counting module is a transistor-transistor logic (TTL) pulse train with ∼10 ns width, which can be recorded by a digital counter on a PCI-6014 multifunction data acquisition board. The number of photons arriving during a specified time period equals the difference of two counter readings at the beginning and the end of the period. A Labview program (figure 4.6) was

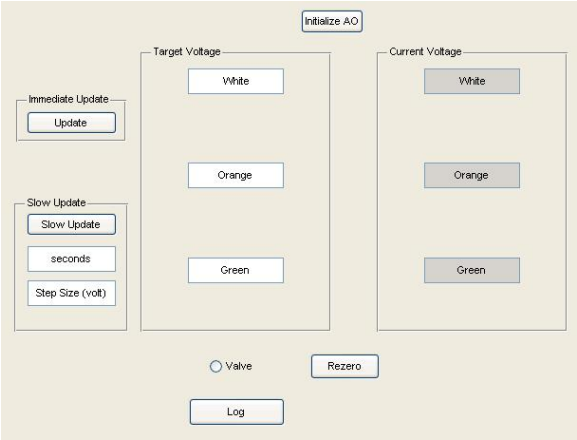

Figure 4.5. The user interface of a more advanced Matlab program to control pressure regulators.

written to set the bin time and length of acquisition.

4.1.3.3 Mechanical Shutter

The mechanical shutter was managed by a smart shutter controller which talked to both Metamorph and general TTL signal source. In the first case, the opening and closing of the shutter could be synchronized with the exposure of CCD array on Cool Snap. In the latter, any TTL pulse could be used to trigger the shutter. This is useful for coordinating the reading of the counter and the status of the shutter.

4.1.3.4 Solenoid Valve

The activation of control valve was realized by opening the solenoid valve between the device and the pressure source. Because the available voltage source did not have enough current to activate the solenoid, a relay circuit, under the control of available voltage output, was built to supply the required current.

The relay circuit is detailed in figure 4.7. The solenoid valve needs 12 VDC and at least 250 mA to activate, and this can be provided by a commercial power adapter (ELPAC-WM113). Unfortunately, no switch is provided with the power source, so a Reed relay was inserted between the solenoid and the power source to control the application of voltage. The available relay module (W171-DIP-7)

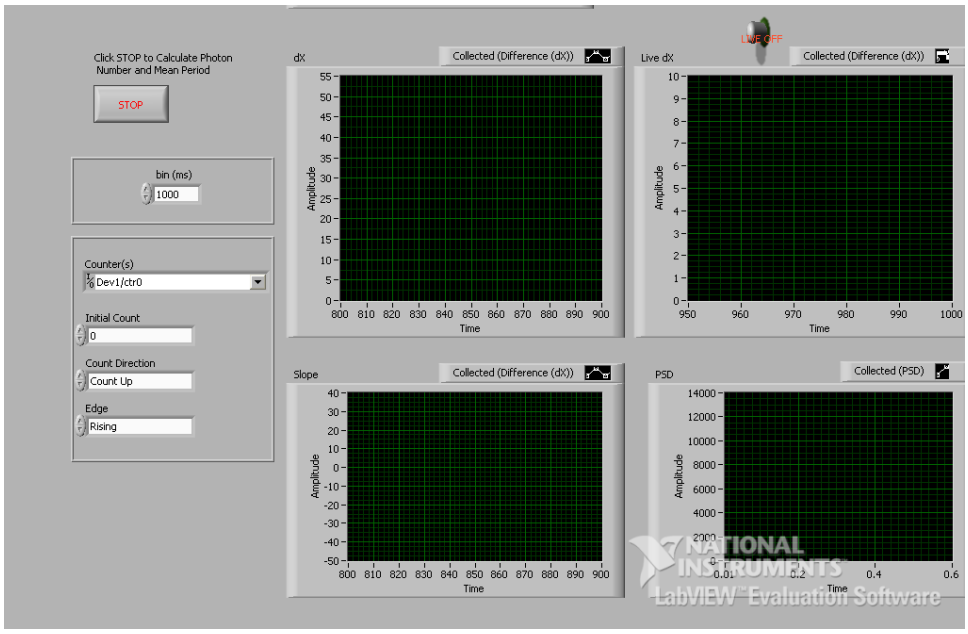

Figure 4.6. Labview program to control the counter.

needs an input voltage of 5 V and at least 10 mA which is bigger than what is available from either USB-3103 or TTL output signal. To amplify the current, a transistor (2N3904) was employed. Because $h_{FE} > 100$ for the transistor, when 5 V signal is applied to the base, a base current of 0.42 mA (= 5 V/12 kΩ) generates a collector current of 42 mA, sufficient to close the Reed relay and activate the solenoid. To buffer the sudden change of magnetic field in Reed relay and solenoid, two diodes (1N4001) were added in appropriate places to protect the transistor and external IC board (for example, USB-3103). Additional resistors were also added to attenuate the current flowing through the solenoid. Alternatively, a Darlington pair may be used as a switch to control the application of 12 VDC power supply. This design (figure 4.8) is conceptually simpler than the one in figure 4.7. In either way, a low current 5 V signal could generate the required 12 V source with a current high enough to open the solenoid valve.

In real experiments, the valve was controlled by any of the three voltage sources for different purposes. The simplest scenario was opening the valve from USB-3103 manually from the graphical user interface in figure 4.4 or 4.5. This was useful for device testing when timing was not important. Alternatively, the TTL-out pulse from shutter controller was used to open the solenoid and thus

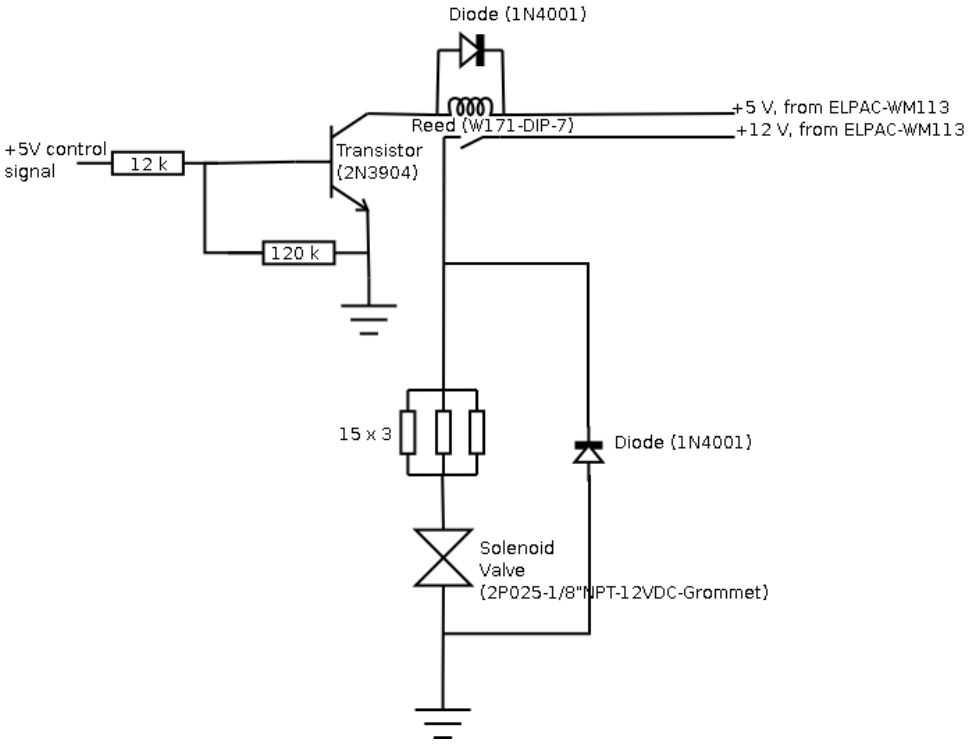

Figure 4.7. Relay circuit to control the opening of solenoid valve.

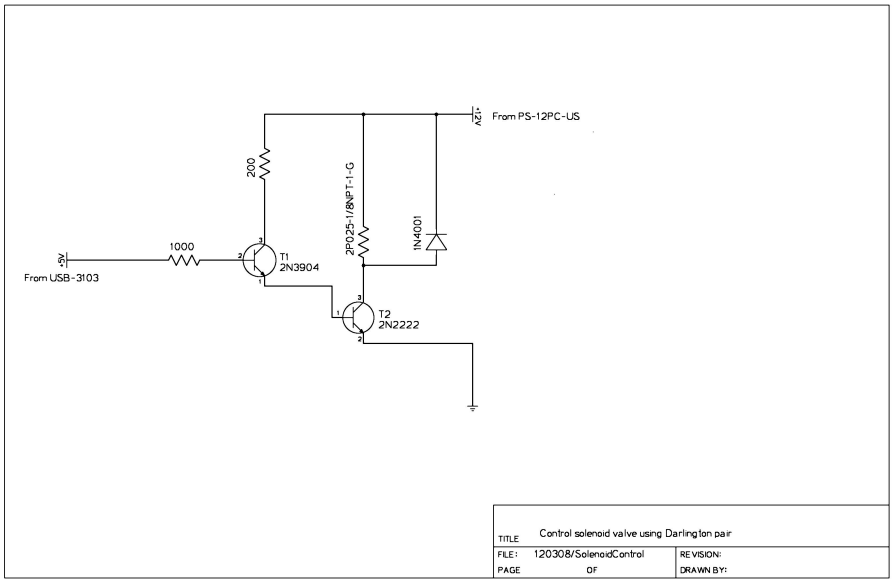

Figure 4.8. Darlington pair to control the opening of solenoid valve.

stop the flow in side channel. In this way, the valve was synchronized with the image acquisition. This was normally used when a time series of fluorescence images was taken to monitor the enzyme kinetics in static droplets. Note that the pressure in the control valve was preserved for about 30 s even after the solenoid valve was closed, so the sequential opening and closing of the solenoid due to the multiple activation of shutter did not change the pressure in control valve significantly over time. Finally, the valve could be controlled by the result of photon counting. The control valve was closed once the photon number was above a certain threshold, which signified the arrival of a droplet in the detection volume. Of course, because of the delay of a couple tens of milliseconds in the activation of solenoid valve, there was little chance to capture the same droplet that was responsible for the threshold crossing. But a tunable delay could be intentionally inserted after the threshold-crossing event such that when the flow stopped, there was a significant chance for a droplet to land at the focal volume. This was achievable due to the regular spacing and stable speed of the droplet train. Indeed, as illustrated in figure 4.9, automatic closing of control valve using the threshold-crossing mechanism guaranteed that in most cases, droplets landed reproducibly at the same position (inside the white circle) after the flow is stopped. Figure 4.10 shows the Labview interface to realize this control mechanism.

4.2 Shear-driven Redistribution of Surfactant Affects Enzyme Activity in Well-mixed Femtoliter Droplets*

Abstract

We developed a microfluidic platform for splitting well-mixed, femtoliter droplets from larger water-in-oil plugs, where the sizes of the daughter droplets were not limited by channel width. These droplets were separated from mother plugs at a microfabricated T-junction, which enabled the study of how increased confinement affected enzyme kinetics in droplets 4–10 μm in diameter. Initial rates

*This section is adapted from Y. Liu, S.-Y. Jung, and C. P. Collier, Anal. Chem., 81:4922–4928, 2009. Copyright 2009 American Chemical Society.

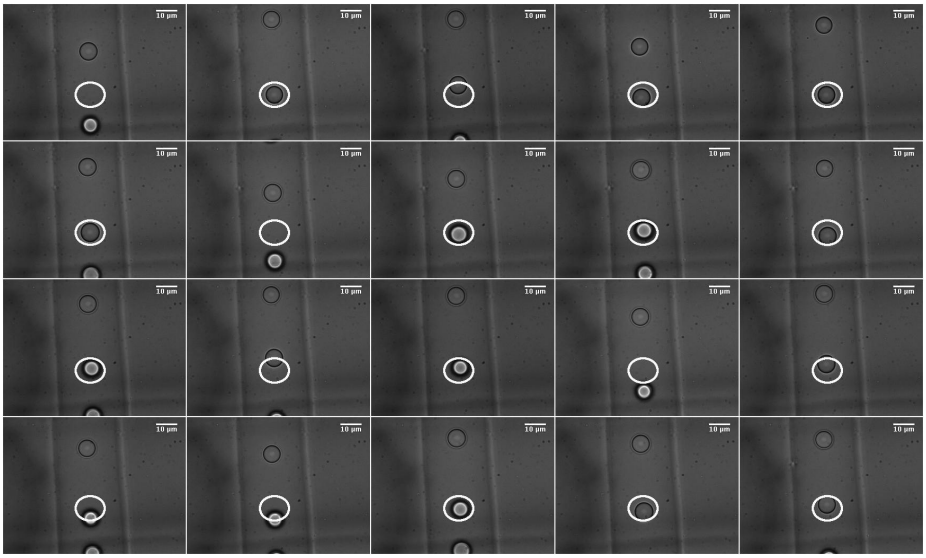

Figure 4.9. Using threshold-crossing mechanism to automatic stop the flow guaranteed that in most cases (13 out of 20 shown here) droplets landed at roughly the same position. This was important to increase data acquisition efficiency when PMT, with a confined detection volume, was used as the detector.

for enzyme catalysis in the mother plugs and the largest daughter droplets were close to the average bulk rate, whereas the rates in smaller droplets decreased linearly with increasing surface-to-volume ratio. Rates in the smallest droplets decreased by a factor of four compared with the bulk rate. Traditional methods for detecting nonspecific adsorption at the water–oil interface were unable to detect evidence of enzyme adsorption, including pendant drop tensiometry, laser scanning confocal microscopy of drops containing labeled proteins in microemulsions, and epifluorescence microscopy of plugs and drops generated on chip. We propose that the slowing of enzyme reaction kinetics in the smaller droplets was the result of increased adsorption and inactivation of enzymes at the water–oil interface arising from transient interfacial shear stresses imparted on the daughter droplets as they split from the mother plugs and passed through the constricted opening of the T-junction. Such stresses modulate the interfacial area and density of surfactant molecules that can passivate the interface. Bright-field images of the splitting processes at the junction indicate that these stresses scaled with increasing surface-to-volume ratios of the droplets but were relatively insensitive to the average flow rate of plugs upstream of the junction.

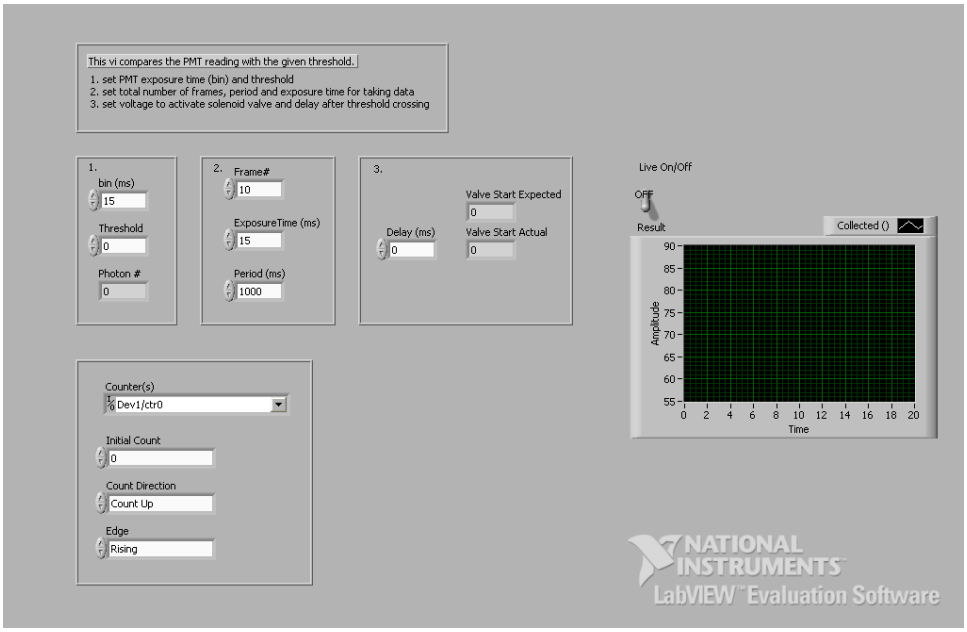

Figure 4.10. Labview program to control the valve closing by fluorescence signal.

4.2.1 Introduction

Advances in nanotechnology offer opportunities for discovering and characterizing new chemical and biochemical phenomena in ultrasmall, biomimetic systems containing only a few reacting molecules [15, 16, 115, 131]. Many biochemical transformations in living systems occur in highly nonideal, crowded, and confined cellular nanoenvironments, which can significantly affect thermodynamic and kinetic properties [99, 121]. Numerous methods have been reported for carrying out chemical and biochemical reactions in compartmentalized containers as model systems [63, 68, 70, 81, 112, 113, 153]. However, nonspecific adsorption and inactivation of enzymes at surfaces and interfaces at small scales, as the surface-to-volume (S/V) ratio becomes very high [77], can significantly degrade the ability to obtain accurate measurements of kinetic rates.

Water-in-oil plug formation in microfluidic devices has become an attractive and well-established method for the compartmentalization of aqueous reactions that avoids the inherent surface properties of polydimethylsiloxane (PDMS) and other solid materials [129]. Many reports have been published on the formation and rapid mixing of monodisperse water-in-oil plugs formed at the intersection of two or more aqueous streams with an immiscible oil stream (for a review, see reference [129]). As

is the case for compartments defined in solid substrates, minimization of nonspecific adsorption of biomolecules at the aqueous–oil interface requires careful choice of passivating molecules, typically polyethylene glycol (PEG)-based phospholipids or surfactants. Control of nonspecific protein adsorption at the water–oil interface has been demonstrated by Roach et al. in microliter drops with pendant drop tensiometry, and nanoliter water-in-oil plugs in a microfluidic device by fluorescence microscopy and measurements of enzyme kinetics [114].

The sizes of water-in-oil plugs scale with microchannel dimensions, typically in the range 10–100 μm. We have designed a microfluidic device, shown schematically in figure 4.11 that included a second T-junction downstream of a mixing stage, which allowed smaller daughter droplets ($\leq$10 μm in diameter) with well-mixed, homogeneous concentration profiles, to be split off from the larger water-in-oil mother plugs. Without a change in the geometry of the second T-junction [84] or implementing complicated pressure control schemes at both inlets and outlets [94, 170], daughter droplet volumes could be continuously and reproducibly controlled over more than 2 orders of magnitude by adjusting the backing pressures at the oil and aqueous inlets. The resulting daughter droplet size distributions for all diameters generated at the second T-junction had coefficients of variation (COV) that were less than 3%, indicating they were monodisperse and configurable. The nascent daughter droplets were then trapped in the side channel of the junction by closing a control valve. This device was used to measure the effects of daughter droplet volume on the reaction rates of confined β-galactosidase enzymes (β-Gal) at the same concentration using a fluorogenic assay involving the hydrolysis of nonfluorescent substrate molecules to yield fluorescent resorufin [112, 113]. The assay was carried out with the same concentration of enzyme and substrate as in the bulk, for droplets ranging from 4 to 10 μm in diameter, which corresponds to volumes of 34–523 fL (10^{-15} L).

Based on measurements from drop tensiometry and from reaction rates for β-Gal in larger daughter drops formed in our device (9–10 μm in diameter), which were close to the average bulk rate, we found that nonspecific adsorption of β-Gal enzymes was suppressed at the water–oil interface with the inclusion of a PEG-based surfactant, consistent with reports by Roach et al. [114]. These findings were corroborated by epifluorescence microscopy of drops and plugs containing fluorescently

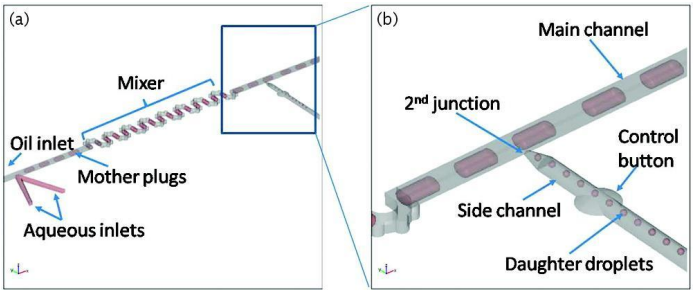

Figure 4.11. (a) Schematic of the microfluidic device used to produce monodisperse, homogeneous water-in-oil droplets with diameters that could be precisely controlled from 2 to 10 μm. (b) Detail of the T-junction used to generate daughter droplets from mother plugs and the control valve used to trap them in the side channel. The main channel was 30 μm wide and 25 μm high with a rectangular profile. The two aqueous inlets were each 20 μm wide and 25 μm high. The side channel was rounded to 30 μm wide and 12 μm high, except for the control button (60 μm wide and 10 μm high) and the T-junction opening (15 μm wide and 5 μm high).

labeled β-Gal enzymes and PEG surfactant generated in the microfluidic device and laser scanning confocal microscopy images of droplets in microemulsions. However, we found a linear decrease in the initial reaction rate for enzyme catalysis from smaller daughter droplets split off from mother plugs at the second T-junction in the device. The reduction scaled with decreasing droplet diameter, from 10 μm, where the average initial rate was only slightly lower than the bulk rate, to 4 μm, which had an initial rate that was four times slower than that in the bulk.

In this article, we propose a mechanism for this decrease in initial reaction rates for confined β-Gal enzymes with decreasing daughter droplet size. A key assumption in our analysis is that nonspecific adsorption of β-Gal enzymes at the water–oil interface results in a reduction of the enzyme's catalytic efficiency, by affecting either K_{M} or k_{cat} in the Michaelis–Menten (MM) mechanism or both. This assumption is supported by an extensive series of control experiments which demonstrated that the decrease in measured reaction rate did not result from substrate depletion, product inhibition, or optical effects in the confined volumes. Nor was it the result of instabilities due to pressure fluctuations in the device or uncertainties in determining droplet diameters, which were measured with high accuracy and precision. We believe that effective passivation against enzyme adsorption at the interface initially present in the larger mother plugs in the main channel of the microfluidic

device decreased during the formation of the smaller daughter droplets in the side channel. This decrease in passivation effectiveness at the interface was the primary cause for the observed decrease in enzyme kinetics in the smaller droplets. Standard methods for characterizing passivation against nonspecific adsorption of biomolecules at surfaces and interfaces such as tensiometry and fluorescence imaging with labeled proteins failed to capture this effect.

We present evidence for loss of enzyme activity during daughter droplet formation in the microfabricated T-junction due to shear-induced changes in interfacial area and, hence, density of surface active molecules, including both PEG surfactant molecules and β-Gal enzymes. This evidence is consistent with reports in the literature characterizing shear-induced effects on surfactant interface distributions during droplet deformation and breakup in multiphase flows at low Reynolds numbers [22, 102, 142]. In particular, our proposed mechanism is similar to that published by Cate and co-workers for describing mixing of crowded biological solutions in water-in-oil plugs, based on interfacial shear stresses generated by microfabricated protrusions of the channel walls in their device [82].

Our results indicate that methods used for forming ultrasmall volumes could have significant effects on kinetics. Traditional methods for characterizing protein adsorption at liquid-liquid interfaces may show negligible adsorption in nanoliter volumes containing thousands of enzymes typically encountered in microfluidics devices, but fail to detect protein adsorption in smaller-volume daughter droplets that results from S/V scaling and mechanical manipulation of the water–oil interface during droplet splitting. These effects will become more prominent as the number of biomolecules at a given concentration in the confined space becomes small. Quantitatively accounting for these effects will be important in characterizing new chemical and biochemical kinetic phenomena in confined nanoenvironments [76, 118].

4.2.2 Experimental Section

β-Gal was purchased from Calbiochem (Gibbstown, NJ), and resorufin-β-D-galactopyranoside (RGP) was obtained from Molecular Probes (Eugene, OR). Alexa568 labeled β-Gal (Alexa568-β-Gal) was obtained using the Protein Labeling Kit (Molecular Probes, Carlsbad, CA). Resorufin was purchased

from Sigma-Aldrich (St. Louis, MO). These were used without further purification for making aqueous solutions with Millipore 18 MΩ water (Billerica, MA) or 100 mM phosphate buffered saline (PBS) containing 1 mM $MgCl_2$ at pH 7.2. Soybean oil (Sigma-Aldrich) used in this experiment was purified of surface-active contaminants (mainly monoglycerides) by gravity filtration through a column packed with a 1:1 mixture of fluorisil and silica gel (100–200 mesh, Sigma-Aldrich) until the equilibrium interfacial tension at the oil–water interface matched that of reported value for purified soybean oil in the literature (31 mN/m) [34]. 4-Nonylphenyl-polyethylene glycol (NP-PEG) surfactant (Sigma-Aldrich) was diluted to 0.1% (v/v) in the purified soybean oil. We had originally tried both silicone oil and perfluorinated oil. We found that the PDMS in our microfluidic devices was swelled by silicone oil. This caused changes in flow rate over time, which made control of flow rate extremely difficult. When perfluorinated oil was used, daughter droplets were not formed at the T-junction reproducibly, due to the higher interfacial tension between the perfluorinated oil and aqueous buffer. These effects had been seen before for on-demand generation of femtoliter droplets by shear [87]. Purified soybean oil with NP-PEG surfactant worked the best in terms of both inertness to PDMS and stability of daughter droplet formation.

The microfluidic devices were fabricated using multilayer soft lithographic techniques (see supporting information for details). Three Teflon jars (Big Science, Huntersville, NC) containing purified soybean oil or aqueous solutions (one jar for enzyme solution, and one for substrate) were connected in parallel to the appropriate inlets on the PDMS device through Tygon (Small Parts, Miramar, FL) and 23-gauge stainless-steel tubing (Technical Innovations, Brazoria, TX). Backing pressures (compressed N_2) for the aqueous and oil reservoirs, ranging from 10 to 25 psi, were controlled by high-precision voltage-to-pressure transducers (Marsh Bellofram, Newell, WV) which forced fluids from the jars into the main flow channel. A Matlab program (Mathworks, Natick, MA) precisely controlled the voltages applied to the transducers, routed through an analog output board (16 bit resolution, 0–10 V range, USB-3103, Measurement Computing, Norton, MA). The backing pressures at the different inlets were optimized independently to achieve stable formation of mother plugs in the main channel and the generation of daughter droplets of desired diameter in the side channel. The control valve reservoir and an osmotic bath in the control layer were filled with 18 MΩ water

to prevent water pervaporation from the droplets [53]. The control valve was deflected downward by compressed N_2 (30 psi) to seal the side channel and stop the movement of daughter droplets on demand in the field of view of an inverted optical microscope (Eclipse TE 300, Nikon Instruments, Melville, NY), operating in epifluorescence mode with a 100× oil-immersion objective (NA 1.4). Bright-field or fluorescence images were captured with a CoolSNAP-HQ CCD camera (Roper Scientific, Tucson, AZ) and analyzed with Metamorph software (Universal Imaging Corp., Downing Town, PA), ImageJ (National Institutes of Health) and custom-made Matlab scripts. A 200 W mercury–xenon arc lamp (Ushio, Japan) acted as the light source in combination with appropriate filter sets (G-2E/C, Nikon Instruments) for the detection of resorufin fluorescence. Photobleaching of resorufin was minimized by utilizing neutral density filter sets (ND8 and ND4) and synchronizing the CCD camera with a Lambda SC smart shutter (Sutter Instrument Company, Novato, CA). Included in the supporting information are detailed descriptions of experiments to characterize the performance of our device for the stable generation and manipulation of well-mixed, monodisperse sub-10 μm water-in-oil droplets, calibration of fluorescence intensities as functions of substrate concentration and droplet diameter, and traditional assays employed for measuring nonspecific interfacial adsorption such as pendant drop tensiometry and laser scanning confocal microscopy of labeled enzymes in microemulsions.

4.2.3 Results and Discussion

Stable generation and trapping of droplets

The device design is similar to those reported by other groups for producing monodisperse, well-mixed water-in-oil plugs [114], with the addition of a second microfabricated T-junction downstream from the plug formation region and the mixing stage to generate smaller daughter droplets from mother plugs. The incorporation of a control valve in the side channel stopped daughter droplets on demand within the field of view of an inverted epifluorescence microscope. The overall scheme of the microfluidic device is depicted in figure 4.11. Two aqueous inlets (rectangular, 20 μm wide × 25 μm high) introduced enzyme and substrate streams independently into the main channel (rectangular,

30 μm wide × 25 μm high), where they formed mother plugs entrained in the oil phase. At the capillary numbers associated with fluid flow in the main channel in our device (0.06), the dynamics associated with plug formation is best described by Stone, Whitesides and co-workers [36], and is composed of periodic blocking of the oil flow by the aqueous streams. Each blocking event generated a slightly higher positive backpressure in the oil channel, which swept the aqueous plug down the main channel, allowing the process to be repeated. Once steady-state conditions were reached, the plug formation frequency and plug volumes were stable for extended times (20–30 min without any adjustments). At this point, minor increases of the backing pressure at the oil inlet resulted in slightly shorter aqueous plugs formed at moderately higher flow rates.

After formation at the oil–aqueous inlets, the mother plugs entered a winding mixing stage, which mixed the contents of the plugs by chaotic advection [114]. This process was facilitated by microfabricated "cavities" along the mixing channel periphery [82]. Fluorescent images of mother plugs formed by mixing Alexa568-β-Gal and buffer solution indicated that mixing was complete within 300 ms. The supporting information includes descriptions of several tests of plug formation stability against pressure fluctuations in the device, as well as careful calibration of the relative rates of injection of the two aqueous streams (enzyme and substrate) into the main channel to ensure that there were always 1:1 mixtures in the mother plugs.

Usually, aqueous plugs formed by entrainment in an immiscible oil phase have widths and heights that match the cross-sectional dimensions of the microchannel and larger lengths [170]. Further reduction of the plug size by increasing shear force is limited by the dimensions of the aqueous inlets at the intersection with the main channel. In addition, reducing the interfacial tension with surfactant tends to destabilize plug formation, resulting in random break up of the plugs [173]. This occurs when the amount of surfactant in the oil lowers the interfacial tension to the point where the capillary number of the system, $Ca = \mu v/\gamma$, where μ is viscosity, v is the average velocity, and γ is the interfacial tension, switches from a "squeezing," pressure-dominated regime ($Ca < \sim 10^{-2}$), necessary for efficient plug formation, to a "dripping," shear-dominated regime ($Ca > \sim 10^{-2}$), where the aqueous streams no longer periodically block the oil inlet channel sufficiently to form isolated plugs [36]. To form a monodisperse distribution of smaller droplets with tunable sizes, we

incorporated a microfabricated T-junction (rounded, 30 μm wide and 12 μm high except at the control button and the T-junction) immediately after the mixing stage, as shown in figure 4.11(b).

Break up processes of monodisperse plugs or droplets in microfluidic flows have been the subject of extensive theoretical and experimental studies [20, 84, 94, 102, 142, 163]. In general, the volume of daughter droplets produced from a microfabricated junction will be dependent on the relative flow resistance of the smaller side channel compared with that of the main channel [84]. The available literature describes only junctions with uniform height. In our design, the height at the opening of the side channel (about 5 μm at the junction) was considerably less than that of the main channel (25 μm), effectively increasing the flow resistance of the side channel without decreasing its width (30 μm). The resulting daughter drops had diameters unconstrained by the side channel width (about 15 μm at the T-junction). Droplets ranging in diameter from 2 to 10 μm were formed reproducibly by increasing the oil flow pressure in the main channel relative to fixed aqueous inlet backing pressures, which corresponds to a change of droplet volume over 2 orders of magnitude. All COV values of the droplet size distributions for our device were less than 3% (supporting information).

The stream of daughter droplets in this device could be stopped instantaneously and trapped in place by applying hydraulic pressure to the control valve (see figure 4.11(b)), which blocked the flow in the side channel without perturbing that in the main channel. In order for the control valve to close the side channel at reasonable pressure (30 psi), the channel was widened to 60 μm at the control point to decrease the local aspect ratio. Negligible vibration of the daughter droplets was observed in the process, in contrast to what has been reported using syringe pumps and sample injection valves [7]. Subsequent daughter droplets could be trapped and interrogated by releasing the valve and closing it again after a short recovery period. Multiple rounds of observation were performed in this manner to collect data from numerous experiments. Trapped droplets were further protected from shrinkage due to water pervaporation by introducing an osmotic bath in the control layer on top of the side channel [53]. The control valve adjacent to the osmotic bath also used water as its working fluid. Prolonged observation on the same droplet could be performed without ambiguity arising from droplet movement, shrinkage, or merging (supporting information).

Initial enzymatic reaction rates decrease with decreasing droplet size

Hydrolysis of the RGP substrate by β-Gal releases fluorescent resorufin, with galactose as a by-product. Enzymatic activity can be followed by monitoring the increase of fluorescence in the droplets as a function of time, due to the accumulation of resorufin in the droplets [112, 113]. Values of $K_{\mathrm{M}} = 128.5$ µM and $V_{\max} = 0.248$ µM/s for the reaction were determined from a Lineweaver–Burk plot of the bulk rate data for β-Gal (0.1 µg/mL) as a function of substrate concentration from 4.86 to 471 µM (supporting information).

Figure 4.12 shows the initial steady-state kinetics for the β-Gal reaction carried out in droplets ranging in diameter from 4.25 to 9.75 µm, in comparison to the average rate from bulk stopped-flow measurements (solid line). The nominal enzyme concentration used for all experiments, both in the droplets and in the bulk, was 1.85 nM (1.0 µg/mL), and the initial concentration of the RGP substrate was 25 µM. Triplicate measurements of the time-dependent product concentrations as functions of time were used to generate the mean and standard deviation for each data point in figure 4.12(a). The error bars for each trace correspond to ± one standard deviation from the mean. Although there were differences in individual reaction rate trajectories from similar-sized droplets in figure 4.12(a) (e.g., the average initial rate from the 9.0 µm droplets was greater than that from 9.5 µm droplets), the trend was the reaction velocity tracked the bulk rate initially and then slowed down significantly after a few seconds. It is important to stress that these fluctuations were not due to pressure fluctuations in the device or uncertainty associated with the measurement of droplet sizes, which were characterized with high precision (supporting information) but came from another source. Enzyme catalysis, in general, appeared to be much slower in smaller droplets.

In fact, when the initial reaction rate is plotted as a function of droplet size, a clear negative trend compared with the bulk rate with decreasing droplet size can be seen that is statistically significant. The mean and standard deviation of the initial enzymatic reaction rate as functions of droplet diameter from 1067 droplets are plotted in figure 4.12(b). The raw data from the 1067 measurements are included in the supporting information. The initial rates were determined within the first four second after forming the droplets. The initial reaction rate in bulk was 0.36 ± 0.06 µM/s (horizontal

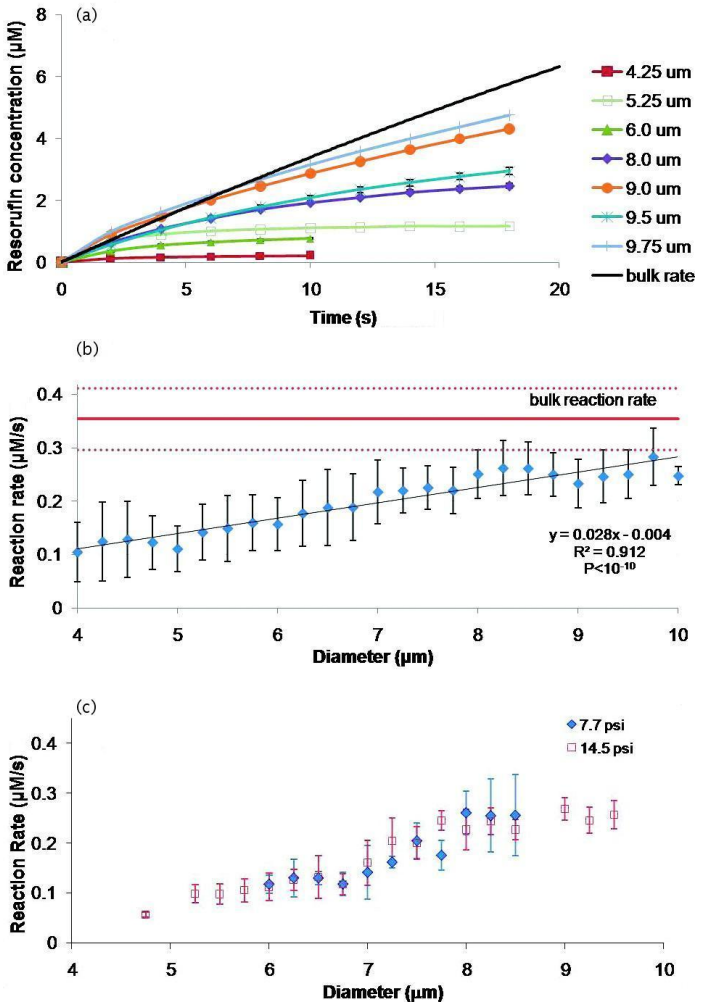

Figure 4.12. Initial reaction rates in femtoliter droplets. (a) Resorufin product concentrations as functions of time for droplets with diameters from 4.25 to 9.75 μm, compared with the bulk reaction. (b) Mean and standard deviations of the initial rate from 1067 droplets. Dashed and dotted horizontal lines represent the mean and ± standard deviation of the initial bulk rate. (c) Subsets of data at two different backing pressures at the oil inlet show similar trends.

solid and dashed lines in figure 4.12(b)), determined from seven independent measurements taken over a 6-month period. The standard deviation in the bulk initial rate reflects the variation in enzyme activity under identical conditions from one lot to the next. (The same vendor had been used for all experiment.) Although there were significant fluctuations in initial reaction rates from the droplets in figure 4.12(a), the trend in figure 4.12(b) was a linear decrease in the average initial reaction rates with decreasing droplet size, from 0.25 ± 0.02 μM/s at the highest value (for 10 μm diameter

droplets) to 0.10 ± 0.05 μM/s at the lowest (for 4 μm diameter droplets). The linear correlation coefficient for the regression of the droplet data (solid line in figure 4.12(b)) was 0.912. The p-value of the null hypothesis was less than 10^{-10} using the Student's t test. The 95% confidence region of the fitted slope in figure 4.12(b) is 0.029 ± 0.004 μM/(s·μm).

We found very similar correlations between the initial reaction rate and droplet size, regardless of the average backing pressures used at the inlets. Figure 4.12(c) shows two subsets of the 1067 total measurements of initial reaction rate versus droplet size, taken at two different backing pressures at the oil inlet (68 droplets at 7.7 psi versus 158 droplets at 14.5 psi; the average backing pressures at the aqueous inlets were about 2 psi lower than the pressures at the oil inlets). Although we did not perform linear regressions on these subsets of measurements, they appear to follow a similar trend as the complete data set in figure 4.12(b).

This result was surprising, given the fact that laser scanning confocal microscopy and epifluorescence microscopy of droplets with labeled β-Gal enzymes, as well as tensiometry measurements, indicated negligible adsorption of β-Gal enzymes to the oil–water interface when 0.1% (v/v) NP-PEG surfactant was used, even for enzyme concentrations two orders of magnitude higher than that (1.85 nM) actually used in the experiments (supporting information). The supporting information includes descriptions of many control experiments performed to eliminate several other possible causes for the decreased reaction rates in smaller droplets. Also included in the supporting information is evidence that the loss of enzyme activity occurred during droplet splitting from the plugs at the second T-junction in the device, not upstream.

Size-dependent interfacial shear redistributes surfactant at oil–water interface in daughter droplets

Detailed examination of the splitting process at the T-junction provides evidence in support of our hypothesis that droplet splitting affects the passivation of the water–oil interface against nonspecific binding and subsequent inactivation of β-Gal enzymes. Figure 4.13 includes bright-field images of daughter droplets being split off from mother plugs at the second T-junction, for two different droplet diameters: 6 μm (figure 4.13(a)–(d)) and 10 μm (figure 4.13(e)–(h)). All of the images were taken at

an average linear flow velocity in the main channel of 1.7 mm/s except for figure 4.13(c), which had an average flow velocity of 6.6 mm/s. The fact that two different flow rates (figure 4.13(c) versus (a), (b), and (d)) resulted in the same droplet diameter (6 μm) is consistent with the correlation plot in figure 4.24 of the supporting information, which showed that droplet diameter was more dependent on the minor but well-controlled pressure difference of the oil inlet relative to the aqueous inlets at steady state than the overall magnitude of the backing pressure and, hence, flow rate in the main channel. This observation has been reported before for water-in-oil droplets in microfluidic devices [160].

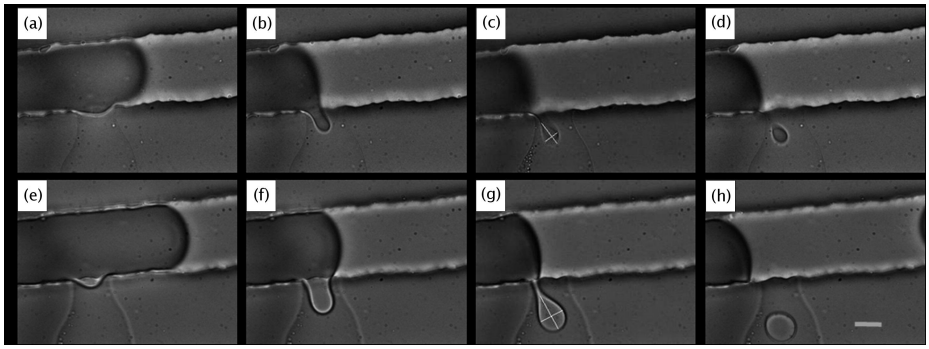

Figure 4.13. Bright-field images of daughter droplets splitting off from mother plugs at the microfabricated T-junction connecting the main and side channels. Plugs are traveling from right to left in the main channel. (a)–(d), 6 μm droplets; (e)–(h), 10 μm droplets. The plug flow rate was 1.7 mm/s for all images except for (c), which was 6.6 mm/s. Scale bar is 10 μm. Overlaid white crosses in (c) and (g) were used for graphical estimation of capillary numbers for budding droplets, which are included in Table 4.1.

It is this minor pressure difference at the intersection between the aqueous and oil phases that controls the length of the mother plug when it is formed, and, hence, the size of the resulting daughter droplet. The plug flow rate was not nearly as important in determining droplet diameter as plug length, which suggests that droplet diameter in our device was primarily controlled by the temporal overlap between a characteristic splitting-off time, determined by the nozzle geometry of the constriction of the T-junction as well as the viscoelastic properties of the fluidic interface, and the time it takes for the mother plug to travel across the opening. For the smaller 6 μm droplets,

the initial budding event occurred closer to the end of the plug in figure 4.13(a), which limited the growth of the nascent daughter droplet before it was split off, compared with the 10 μm droplet in figure 4.13(e). Apparently, the characteristic droplet splitting-off time and the plug transit time across the junction opening have similar relative scaling at higher and lower flow rates (as evidenced by the same droplet size for figure 4.13(c) as (a), (b) and (d)).

The constriction of fluid flow at the nozzlelike orifice of the junction (height 5 μm) generated local extensional and shear stresses responsible for the droplet budding and stretching from the mother plug seen in figure 4.13(a), (b), (e), and (f) [20, 84, 94, 102, 142, 163]. As a daughter droplet passes through the constriction and is deformed by the external flow field, the capillary pressure at the nose of the droplet will be less than that at the neck of the constriction, due to differences in radii of curvature. This pressure gradient results in an interface instability which allows an oil film to grow at the neck of the constriction, eventually splitting off the daughter droplet from the plug [102, 163]. The transient processes that occur during droplet splitting change the distribution of surface-active molecules at the interface, including NP-PEG surfactant, as well as β-Gal enzymes. The locally high fluid velocities and shear forces present at the neck of the constriction in the junction result in changes in the interfacial area of the droplet due to shape distortion effects such as dilation and contraction. These changes in interfacial area result in changes in surfactant density at the interface and, hence, passivation against nonspecific binding of enzymes. In addition, shear-induced convection of surfactants or enzymes to and on the interface can occur. The relative contributions of uniform dilution of surfactant at the interface due to droplet shape distortion and the formation of surfactant density gradients due to forced convection will depend on the relative contributions from local capillary numbers at the junction during droplet splitting and the surfactant Pélet number, which is the dimensionless ratio of surfactant convection to diffusion [102]. A similar mechanism was used by Cate and co-workers to describe the mixing of crowded viscous solutions in water-in-oil plugs, using microscopic bumps fabricated in the channel walls of their serpentine mixing stage to generate oscillating interfacial shear stresses in the plugs [82].

Although we were not able to directly measure the shear forces acting on a budding daughter droplet as it split off from its mother plug, we carried out a semiquantitative analysis based on

Table 4.1. Shear stresses for nascent daughter droplets at the T-junction

mean aqueous inlet pressure (psi)	oil inlet pressure (psi)	droplet diameter (μm)	$Ca \approx (L-B)/(L+B)$	Laplace pressure (psi)	shear stress (kPa)
9.9	11.4	9.3	0.21	3.2	0.68
9.9	11.7	5.2	0.27	5.8	1.6
19.7	21.5	8.8	0.20	3.4	0.68
19.7	22.0	5.7	0.30	5.3	1.6

Taylor's theory of droplet deformation under shear stress [157]. A droplet subjected to shear stress by an external flow field will deviate from a spherical shape. The length (L) and breadth (B) of the deformed droplet can provide a measure of the capillary number $Ca \equiv$ shear stress/Laplace pressure for a stationary droplet (i.e., not moving with the external flow). Specifically, Taylor derived a dimensionless parameter $F \equiv (L-B)/(L+B)$, which is equivalent to the capillary number for a stationary droplet. This condition should be approximately satisfied for a new droplet within the first few milliseconds as it splits from the mother plug, as seen in the images in figure 4.13. Included figure 4.13(c) and (g) are line segments corresponding to measurements of L and B overlaid on images of daughter droplets at the moment where they are almost completely split from their mother plugs. The images used to calculate $F \equiv (L-B)/(L+B) \approx Ca$ for all the entries in Table 4.1 are included in the supporting information.

Table 4.1 summarizes the results of such a calculation for both large and small daughter droplets imaged under different backing pressures. The Laplace pressure was calculated from $2\gamma/r$, where γ is the interfacial tension at the oil–water interface in the presence of the 0.1% (v/v) NP-PEG surfactant (7.5 mN/m) and r is the radius of the imaged droplet. With an estimate for Ca and the Laplace pressure, the shear stress can be calculated.

The results in Table 4.1 show that smaller daughter droplets experienced higher shear stress during their formation, regardless of the magnitude of the average backing pressures applied at the inlets, consistent with the results shown in figure 4.12(c) and by others [160]. Because of the higher shear stress imparted on the smaller droplets as they were split off from their mother plugs, surfactant molecules initially uniformly distributed at the oil–water interface were perturbed, which led to a reduction in the passivation of the interface, and the adsorption and inactivation of enzymes.

Another possible mechanism that could explain the size-dependent reaction rates seen in droplets

would be the deformation or denaturation of β-Gal enzymes directly from shear stresses present in the aqueous interior of the droplets. We have not been able to find a quantitative analysis for shear-induced destabilization of β-Gal enzymes in the literature. However, for urease, a multimeric high molecular weight (480–545 kDa) enzyme similar to β-Gal in complexity, shear-induced decreases in enzyme kinetics were reported only for shear strain histories (shear rate multiplied by exposure time) greater than 10^5 (and only in the presence of propitious metal ions) [161, 162]. Such shear-induced decreases in urease activity were reversible. In our case, the maximum shear rate the enzymes could have experienced in the droplets can be estimated by dividing the shear stresses listed in Table 4.1 by the viscosity of water at 20 ℃ (0.1 cP) to give the range of shear rates: $\sim 10^5$–10^6 s^{-1}. The maximum shear rate multiplied by the splitting-off time of daughter droplets from mother plugs when shear forces were present (2–10 ms, based on the flow rates of plugs in figure 4.13) result in, at most, shear strain histories of only 10^3, two orders of magnitude less than that reported to deactivate urease. On the basis of these considerations, we believe it is more likely that irreversible adsorption at the interface is the predominant mechanism for enzyme deactivation.

The supporting information describes an experiment using soluble PEG molecules as crowding agents in the droplets to confirm an important prediction of our model: the size dependence of the reaction rate decrease would disappear, regardless of the strength of shear stress, if the interface could remain completely passivated during the splitting-off process.

4.2.4 Conclusion

This article is the first report of a microfluidic device design for splitting off daughter droplets from mother water-in-oil plugs where the sizes of the droplets were not limited by the channel width of the device. This design has enabled the controlled initiation and interrogation of catalytic rates for confined enzymes in aqueous droplets down to 4 μm in diameter. This has led to the discovery of shear-induced redistribution of surfactants and enzymes that occurred during the splitting process, which resulted in size-dependent inactivation of some of the initial enzyme population due to non-specific adsorption. We expect to observe similar phenomena as long as small droplets experience high shear forces during their formation, regardless of the details of the device geometry.

The importance of the distribution of surfactants at fluidic interfaces on multiphase fluid flows was first recognized years ago when the terminal velocity of an air bubble in water appeared to be a function of bubble volume [169]. Many authors have worked to characterize the effects that surfactants have on droplet motion and deformation in porous media, in fields such as oil recovery, pollution remediation, and in understanding the rheological properties of polymers [102]. In return, mechanical manipulations of droplet size and shape will change the distribution of surface active molecules at interfaces. These effects were exploited by Cate and co-workers to aid in the mixing of water-in-oil plugs crowded with large macromolecules [82]. However, the same phenomena can also result in driving initially active β-Gal enzymes in the aqueous interior of a droplet to the interface. The consequences for catalysis become proportionately more severe at higher S/V ratios and as the population of enzymes in the confined environment decreases (supporting information). At nanomolar concentrations, the total number of β-Gal enzymes decreases from thousands of molecules in the mother plugs, to hundreds of molecules in 10 μm droplets, and to just tens of molecules in 4 μm droplets. As the degree of confinement increases, S/V effects become increasingly important. A fully quantitative understanding of how these phenomena impact chemical and biochemical kinetics in confined systems would require real-time spatial or spectral imaging of the redistribution of surfactant and proteins as the droplets pass through the junction with laser scanning confocal or total internal reflection microscopy, in conjunction with numerical analyses of the time-dependent convection-diffusion equation relating droplet deformation with surfactant transport, which is beyond the scope of this work.

This knowledge will help in the choice of an appropriate combination of working fluid, device geometry, surfactant concentration, and flow conditions to reduce the effect of surfactant redistribution on the nonspecific adsorption of enzymes. It has been shown recently that either reducing shear force or increasing surfactant concentration or mobility [169] can decrease the extent of surfactant redistribution at the droplet interface. However, splitting-off daughter droplets from mother plugs is a multistep process in our device. The operating parameter space is large, and optimizing a critical parameter for one step can have negative consequences for a previous step. For example, increasing the surfactant concentration to better passivate the droplet interface tends to destabilize plug for-

mation, as described above. By monitoring enzymatic reaction kinetics in femtoliter droplets formed in this manner, we were able to identify a new mechanism for enzyme adsorption and deactivation at ostensibly completely passivated interfaces, with important implications for interpreting kinetic data in microfluidics and nanofluidics systems.

Acknowledgement

C.P.C. acknowledges support from the Center for Nanophase Materials Sciences, which is sponsored by the Division of Scientific User Facilities, Office of Basic Energy Sciences, U.S. Department of Energy. Research is sponsored in part by the Laboratory Directed Research and Development Program of Oak Ridge National Laboratory, managed by UT-Battelle, LLC, for the U.S. Department of Energy under Contract No. DE-AC05-00OR22725. The authors acknowledge assistance from the Micro–Nano Fabrication Laboratory, and the Beckman Institute Molecular Materials Research and Biological Imaging Centers at Caltech.

Supporting information

Mode fabrication

Triple-layer photolithography was used to fabricate a silicon master for fabricating PDMS devices by micromolding. Patterns containing the round control button for the control valve, the side channel, and the main channel were drawn in separate layers in AutoCAD 2004 and imaged at 20,000 dot-per-inch resolution onto optical transparencies (CAD/Art Services, Bandon, OR). To make the control button, a piece of 2-propanol (IPA)-cleaned silicon wafer was spin coated with positive-tone SPR 220-7 photoresist (Shipley Company, L.L.C., Marlborough, MA) at 4000 rpm. After soft baking at 115 ℃ for 90 s, the resist was exposed to UV light under a photomask for 100 s at 14.9 mW/cm^2 on a Karl-Suss MA 6 mask aligner (Suss MicroTec AG, Garching, Germany). MIF-319 developer (Rohm & Haas Electronic Materials, Philadelphia, PA) was used to develop the pattern, followed by rinsing with 18 MΩ water. Overnight baking in an oven at 190 ℃ rounded the feature and stabilized the photoresist. A second layer of AZ 50 positive photoresist (AZ Electronic Materials USA Corp.,

Branchburg, NJ) was spin coated at 4000 rpm onto the wafer to make the side channel. The soft bake consisted of three steps: 2 min at 65 ℃, 5 min at 115 ℃, and 2 min at 65 ℃. After aligning the side channel pattern with the control button, UV exposure at 14.9 mW/cm^2 for 50 s transferred the pattern from the mask to the wafer. A 4:1 (v/v) mixture of water and 2401 developer (Shipley) was used to develop the pattern. Hard baking at 200 ℃ rounded the side channel and stabilized the AZ 50 resist. For the third layer, corresponding to the main channel, SU8-2025 negative-tone photoresist was spin coated onto the wafer at 2500 rpm and soft baked at 65 ℃ for 3 min and 95 ℃ for 6 min. Following careful alignment of the photomask for the main channel and the side channel already on the master, the wafer was exposed to UV illumination for 20 s at 14.9 mW/cm^2. Post exposure baking at 65 ℃ for 1 min and 95 ℃ for 6 min cross-linked the exposed resist; the remaining non-cross-linked residue was removed by immersing the wafer for 1 min in SU8 developer. The master was then hard baked at 150 ℃ for an additional 10 min. The mold for the control valve layer was made by single-layer photolithography using 30 μm thick SU8-2025 resist with the same baking, exposure and development protocol. All the cross-sectional profiles of the patterns were checked with a profilometer (XP2, AmBios Technology, Santa Cruz, CA).

Device fabrication

Multilayer soft lithography was used to make the three-layer PDMS device. The molds for both the flow and control layers were treated in trimethylchlorosilane (Sigma-Aldrich) vapor for 3 minutes to facilitate the separation of cured PDMS from the molds. 40 g PDMS prepolymer (RTV 615, GE Silicones, Wilton, CT) with 5:1 mass ratio of base to curing agent was thoroughly mixed for 1 min, defoamed for 3 min, and then poured into a Petri dish containing the control mold. Dissolved air in the mixture was further removed by vacuum in a desiccator. The PDMS was partially cured in an oven at 80 ℃ for 45 min. For the flow layer, PDMS prepolymer with 20:1 mass ratio of base and curing agent was mixed similarly and spin coated onto the flow mold at 2000 rpm. PDMS of the same composition was also used to spin coat at 8000 rpm an IPA-cleaned # 0 coverslip (Erie Scientific Company, Portsmouth, NH) to form the bottom layer. The flow and bottom layers were cured at 80 ℃ for 40 and 30 min, respectively. The control layer was peeled from its mold, drilled at

preset punch marks, and aligned with the flow layer. These two layers were bonded together at 80 ℃ for 90 min before being peeled away from the flow mold as a monolithic block. Inlet and outlet holes were drilled through the control layer to the main and side channels in the flow layer with 22-gauge blunt-edge needles, and the top two layers were bonded to the PDMS-coated coverslip permanently by heating overnight at 80 ℃.

Inlet and mixing stability tests

It was critical that the relative rates of injection of the two aqueous streams (enzyme and substrate) into the main channel be balanced by tuning the pressure transducers such that there were always 1:1 mixtures in the mother plugs. This would ensure that the relative concentrations of enzyme and substrate were known accurately when comparing the enzymatic reaction rate as a function of droplet size with the bulk value at the same concentration of enzyme and substrate. We found that pressure fluctuations at the three-way intersection of the aqueous and the oil channels, due to changes in radii of curvature of the oil–aqueous interfaces of the plugs, resulted in fluctuations in the position of the boundary line separating the two aqueous streams at the intersection, and, hence, the relative concentrations of enzyme and substrate incorporated in each plug. These fluctuations, however, could be minimized by careful adjustments of the three pressure transducers, which have a guaranteed accuracy of 0.25% (0.1% typical). Figure 4.14 quantifies the stability of the interface between Alexa568-β-Gal solution and nonfluorescent buffer solution at the intersection of the two aqueous channels by plotting the standard deviation of fluorescence intensity at each pixel from a set of 60 images taken at the inlet. If the interface was perfectly stationary, a peak of zero width would appear in figure 4.14. The width of peak in the center indicates that the error in the final reactant concentration due to the interface fluctuations is less than 10%. Uncertainties in the initial concentrations of enzyme and substrate of 10% would lead to errors in the estimation of enzymatic reaction rates in the Michaelis–Menten formulae of, at most, 5%.

As a further test, we injected fluorescently labeled enzymes into one or both of the aqueous inlets and quantified the concentration of labeled enzymes in daughter droplets relative to that

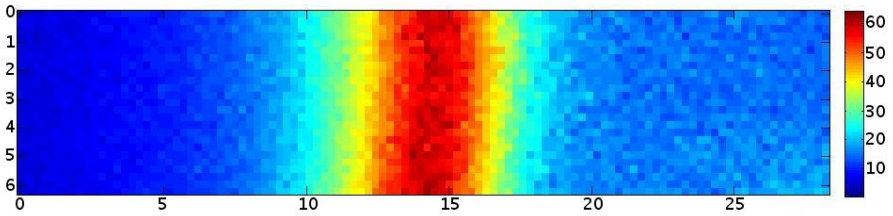

Figure 4.14. Standard deviation of intensity at interface between fluorescent and nonfluorescent streams at aqueous inlet of microfluidic device.

Table 4.2. Mixing tests in daughter droplets with fluorescently labeled β-Gal enzymes

Droplet diameter (μm)	(1) Inject same concentration fluorescent enzymes in both inlets	(2) Inject 50/50 mixture in both inlets	(3) Mix directly on chip
5.00	0.91 ± 0.06	0.5	0.45 ± 0.06
5.25	0.92 ± 0.06	0.5	0.47 ± 0.08
8.00	0.90 ± 0.04	0.5	0.42 ± 0.09
8.50	0.95 ± 0.03	0.5	0.46 ± 0.04

in the aqueous inlet(s) for the following three protocols: (1) Inject same concentration fluorescent Alexa568-β-Gal (13 μg/mL) into both aqueous inlets. (2) Mix 1:1 ratio Alexa568-β-Gal (13 μg/mL) and reaction buffer first, then inject the mixture into both aqueous inlets. (3) Mix 1:1 ratio Alexa568-β-Gal (13 μg/mL) and reaction buffer directly on chip. Table 4.2 shows that the maximum error in labeled enzyme concentration in the daughter droplets for protocol (3) compared with protocol (2) was about 16%, irrespective of droplet diameter, proof that the chip could produce homogeneously mixed daughter droplets throughout the size range from 4 to 10 μm, with reagent compositions identical to that from mixing in the bulk. Protocol (2) was taken as the standard and its intensity was normalized to be 0.5 because it was supposed to give a 1:1 mixing of enzyme and buffer solutions. Protocol (2) should be comparable to (3), which was the on-chip mixture and close to 0.5, within the experimental uncertainty. Solution (1) was enzyme stock only, giving a fluorescence signal about twice that of solution (2).

Plug formation stability

Flow rates of aqueous mother plugs and daughter droplets were determined by analyzing bright-field images from the CCD camera at a specific integration time (1–5 ms). The measured length

of the blur (in micrometer) at the leading or trailing edge of a plug or droplet divided by the integration time yielded the linear flow velocity (in millimeter per second). Averaged results of triplet measurements were recorded. If necessary, flow velocity may be converted to volumetric flow rate (volume/time) using the channel dimensions (see caption to figure 4.11). The same setup also allowed for photon-counting experiments at milliseconds time resolution. These were undertaken to quantify the stability of steady-state plug formation by the device against pressure fluctuations. Fluorescence signal from the steady-state train of plugs containing 0.5 μM resorufin was directed to the side port of the microscope where it was detected by a photon-counting module (PCM 942, Perkin-Elmer, Wiesbaden, Germany) and recorded by a digital counter on a NI PCI-6014 multifunction data acquisition board with two milliseconds bin time (National Instruments, Austin, TX). A Labview (National Instruments, Austin, TX) program was written to control the data acquisition. The stability of mother plug formation right before the T-junction was monitored in this way. Fig 4.15 shows the histogram of detected photon numbers. A superposition of a Poisson distribution, corresponding to the background, and a Gaussian distribution, corresponding to the fluorescence signal from plugs, was used to extract the mean and standard deviation of the signal distribution. A threshold, defined as the mean minus three times the standard deviation of the Gaussian distribution, differentiated the raw data points to be either due to background or fluorescence from the plugs [65].

A typical result is shown in figure 4.16. From more than 4000 peaks, we calculated the peak width to be 18 ± 1 ms and the duration between peaks to be 13 ± 1 ms, which corresponded to a plug length of 95 μm and a head-to-tail plug spacing of 69 μm. These values were corroborated by plug length (100 μm) and plug spacing (63 μm) determined from bright-field images captured under the same flow conditions with the CCD camera. The standard deviation in peak width was smaller than the time resolution (2 ms) in figure 4.16, indicating that plug formation instability due to pressure fluctuations in the system was negligible.

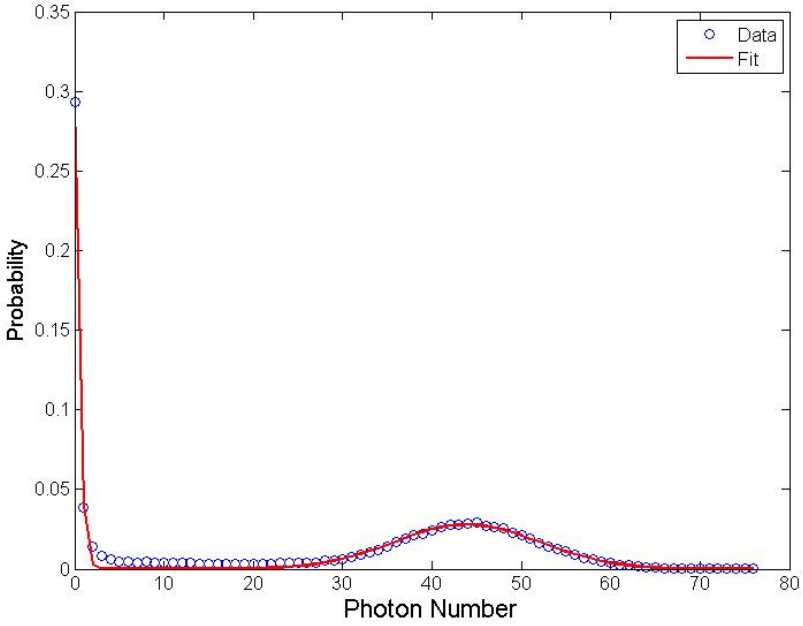

Figure 4.15. The histogram of photon number from a train of plugs containing resorufin. The data (circles) are fitted (line) to a linear superposition of a Poisson and a Gaussian distribution with proper normalization.

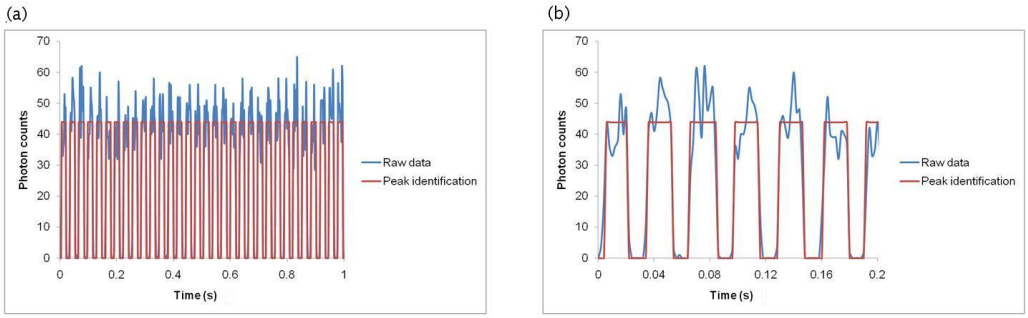

Figure 4.16. Time traces of fluorescent plugs moving in the main channel. Raw photon counts (blue) are assigned as signal from plug or background according to a threshold based on the distribution of the raw data. The result from a peak identification algorithm (red) is shown for comparison. More than 4000 peaks in the full trace of 2 min could be identified without ambiguity. The first 1 s (a) and 0.2 s (b) of the raw data and peak identification are shown.

Droplet size distributions and optical calibration procedures

The optical calibration procedure to determine the concentration of resorufin product as a function of time, and, hence, the rate of reaction in different-sized daughter droplets, consisted of three steps:

(1) bright-field determination of the droplet diameter, (2) determination of the total fluorescence signal from the droplet, and (3) determination of the conversion factors relating resorufin concentration to fluorescence signal from different-sized droplets.

Determination of droplet diameter

Bright-field images of trapped stationary droplets, taken under Köhler illumination conditions, were used to determine droplet diameters according to the following procedure. A bright-field image of an individual droplet was first selected. A rectangular region of interest (ROI) was then drawn about the droplet. Each horizontal line in the ROI was analyzed with a custom made Matlab script to extract the distance between two intensity minima corresponding to a chord length of the droplet. The longest chord length was taken as the diameter of the droplet. The uncertainty in droplet diameter using this method was about one pixel, or 0.25 μm. Figure 4.17 shows the relation between droplet diameter distribution and the backing pressure at the oil inlet. Size distributions are usually characterized by the coefficient of variation (COV = SD/m × 100%, where m and SD are the mean and standard deviation of the distribution, respectively). The COV values of the droplet size distributions for our device were less than 3% for all the data sets reported in figure 4.17 (seven to nine data points for each set).

Determination of total fluorescence signal (I_{tot}) from the droplet

The total fluorescence signal (I_{tot}) from the droplet was calculated on the basis of its diameter, which was determined previously from the bright-field image. A rectangular ROI was drawn around a droplet in the fluorescence image. The location of a tentative droplet center was estimated from the image. The tentative droplet center was moved systematically over a user-specified range in order to maximize the integrated fluorescence signal over the area of a disk with the diameter determined in the previous step. The maximum of the integrated signal was used to define the true center of the droplet. Another region of interest with the same area was then drawn in the vicinity of the droplet to calculate the average background intensity. The maximum of the total signal from the droplet minus the total background signal for the same area defined I_{tot}.

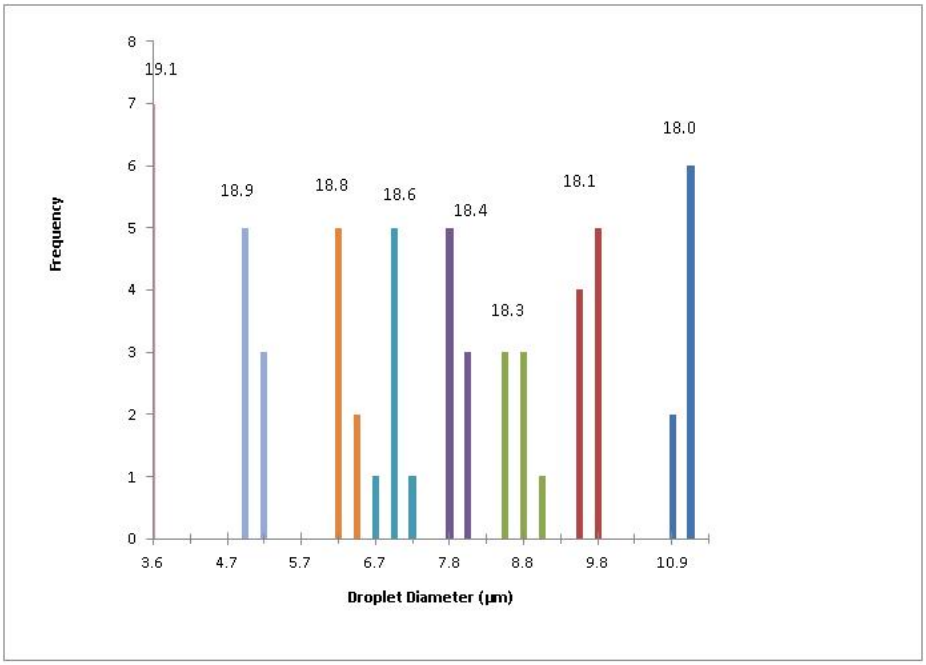

Figure 4.17. Daughter droplet size distributions as functions of backing pressure (labeled in figure in unit of psi) at the oil inlet. The pressures at the two aqueous inlets were held constant at 16.22 and 16.66 psi. Droplets of desired size can be conveniently generated by tuning oil inlet pressure at fixed aqueous inlet pressures.

Conversion between I_{tot} and fluorescent product (resorufin) concentration

I_{tot} was a function of both droplet diameter and resorufin concentration. However, because the fluorescence intensity integrated over the circular area of a selected droplet with measured diameter showed a linear relationship with the concentration of resorufin, we were able to determine the resorufin concentration as a function of time in each droplet from a time-lapse series of images. This was used to calculate the rate of resorufin concentration increase with time due to enzymatic reactions in droplets. For droplets of the same diameter, I_{tot} was proportional to concentration c, so the conversion factor for droplets of the same size was given by I_{tot}/c. The concentration in μM was determined from the absorbance of resorufin at 571 nm, using a molar extinction coefficient of 58,000 M^{-1} cm^{-1} [95]. Solutions with resorufin concentrations ranging from 0 to 4 μM were prepared by serial dilution from a standard solution at 100 μM, and introduced in both aqueous channels of the microfluidic device to generate fluorescence and bright-field images of droplets of

different diameters. In addition to correlating the fluorescence intensity with droplet size, bright-field images of the droplets also ensured that the fluorescence images were focused properly. The average I_{tot} for droplets as a function of size could then be calculated. The absolute concentration of resorufin in the standard solution was determined with a UV/Vis spectrometer (Uvikon 933, Research Instruments International, San Diego, CA). The linear proportionality coefficients used in the calibration of the enzymatic rate data were I_{tot}/c, which varied for different-sized droplets.

Trapped droplet stability

Figure 4.18 compares bright-field images (a)–(c) and fluorescence images (d)–(f) of trapped droplets at different times; no changes in size or position of the droplets were detected after ten minutes. The slight difference between droplets in figure 4.18(b) and (c) was due to minor drift in the focus of the microscope objective for the boundary of the channel in the two images also appeared to change slightly. Prolonged observation on the same droplet could be performed without ambiguity arising from droplet movement, shrinkage, or merging. An alternative process to measure kinetics on a drop by drop basis would be to identify and track a specific moving droplet in real time for sufficiently long times to obtain reliable kinetic information from that droplet. We believe our method is far easier and more amenable for generating large data sets consisting of numerous measurements of different-sized droplets.

Bulk kinetics and Lineweaver–Burk plot

The kinetics of β-Gal–RGP reactions in bulk solution was monitored with a stopped-flow instrument (SX.18MV, Applied Photophysics, Surrey, UK) by measuring the fluorescence increase due to the enzymatic generation of resorufin. Figure 4.19 is a Lineweaver–Burk (LB) plot [19] from bulk reaction rate data for β-Gal (0.1 μg/mL or 1.85 nM), yielding values of $\mathrm{K_M}$ = 128.5 μM and $\mathrm{V_{max}}$ = 0.248 μM/s. The absolute concentration of RGP substrate for each data point in figure 4.19 was checked with the UV–Vis spectrometer ($\epsilon = 18,000\ \mathrm{M^{-1}\ cm^{-1}}$ at 470 nm).

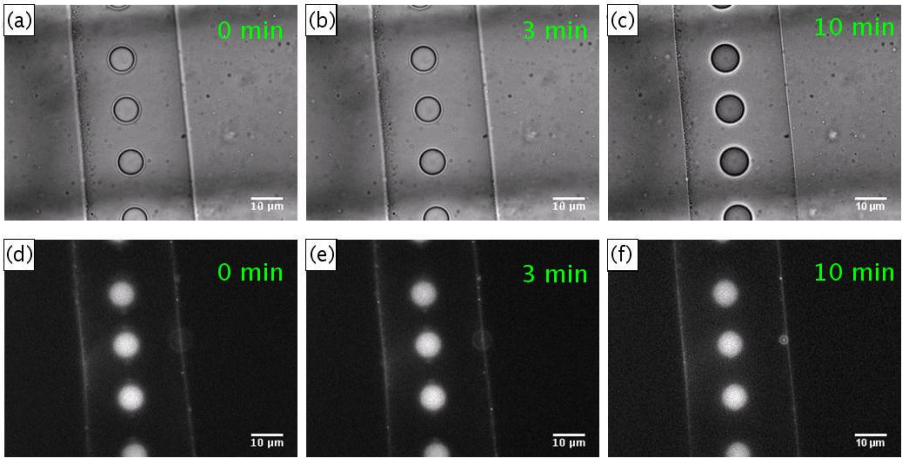

Figure 4.18. Droplet stability after being trapped in the side channel by the control valve. Bright-field [(a)–(c)] and fluorescence [(d)–(f)] images taken when control valve first closed [(a) and (d)], three minutes later [(b) and (e)] and 10 minutes later [(c) and (f)].

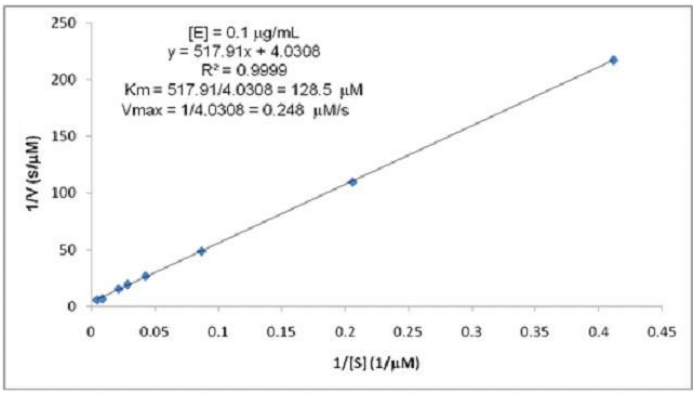

Figure 4.19. Lineweaver–Burk plot for β-Gal enzymes, determined from bulk stopped-flow fluorescence measurements.

Control experiments for kinetic data from droplets in figure 4.12

Many control experiments were performed to eliminate several other possible causes for the decreased reaction rates in smaller droplets observed in figure 4.12 of the manuscript. Consideration of figure 4.12(a) indicates that substrate depletion can be ruled out because the time at which the average bulk rate (0.36 µM/sec) and the fastest droplet rate (from 9.5 µm droplets) diverge, roughly two seconds, corresponds to, at most, the consumption of just 0.7 µM substrate, or roughly three percent of the initial substrate concentration. Bulk absorbance measurements performed both before

and after mixing of aqueous solutions containing 50 μM RGP substrate with soybean oil containing NP-PEG surfactant did not show evidence for substrate incorporation in the oil. Inner-filter effects, due to absorption of emitted light from fluorescent resorufin molecules by other product molecules in the droplets, can be ruled out from the calibration curves of fluorescence intensity versus resorufin concentration, which were linear over the concentration range 0–4 μM for all droplet sizes.

Product inhibition of β-Gal by galactose

To test whether galactose, a by-product of the hydrolysis reaction of the RGP substrate by β-Gal, can act as a product inhibitor, we carried out a bulk assay of initial enzymatic reaction rates using 10 pM β-Gal and 87.5 μM RGP in phosphate buffer, with increasing amounts of added galactose (up to 10 mM). The series of reaction rates was used to generate a dose-response curve and determine the IC_{50} value for galactose inhibition of the reaction [19]. The dose-response plot in figure 4.20 suggests an IC_{50} value for 50% galactose inhibition that is well above the maximum concentration of 10 mM used, orders of magnitude beyond what could have been generated by enzymatic hydrolysis of RGP in the microfluidic experiments.

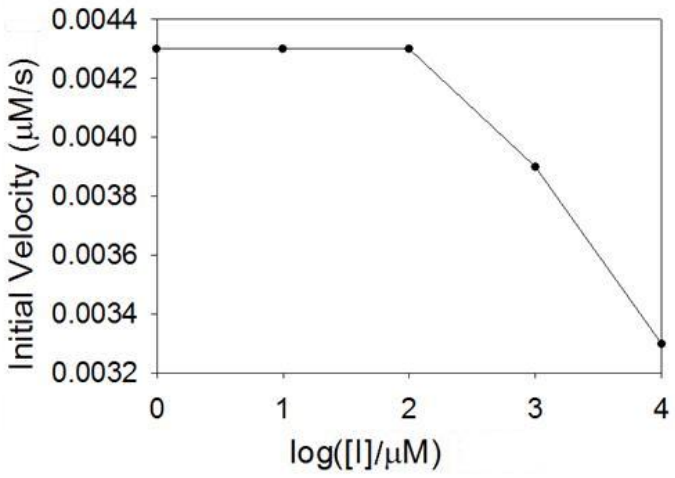

Figure 4.20. Dose-response plot of enzyme initial rate as a function of galactose concentration. Enzyme concentration was 10 pM, and RGP concentration was 87.5 μM, both in phosphate buffer. From this plot, the IC_{50} value for galactose is greater than 10 mM.

Photoreactions involving singlet oxygen

Figure 4.21(a) and (b) are fluorescence plots of 100 µM RGP substrate alone, and 100 µM substrate with 200 nM resorufin, contained in 5 µm diameter chambers (∼100 fL) formed by micromolding in PDMS [68], under the same illumination conditions as the femtoliter droplet experiments carried out in the microfluidic devices as described in the paper. If there was autohydrolysis of RGP due to reaction with singlet oxygen species generated from the photobleaching of resorufin, we would expect to see significant differences in the relative increases in fluorescence in figure 4.21(b) versus (a) over the time course of five minutes.

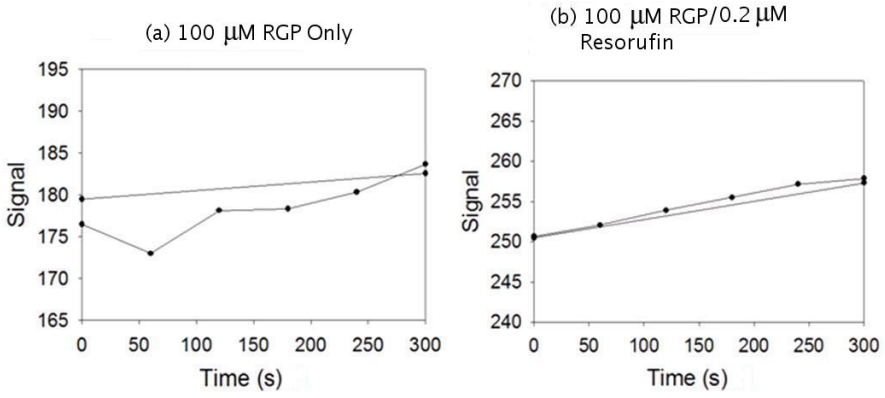

Figure 4.21. Fluorescence increases over five minutes measured with CCD camera in 5 µm diameter chambers defined in PDMS containing (a) RGP substrate only, and (b) a mixture of RGP and resorufin. Illumination conditions were the same as for the droplet experiments in the microfluidic devices.

Photobleaching

Figure 4.22 shows the decrease in resorufin fluorescence due to photobleaching from a 9.5 µm drop (figure 4.22(a)) and from a 6 µm drop (figure 4.22(b)), under the same illumination conditions as used during the experimental determination of enzymatic reaction rates. The fitted first-order decay constants (k_{bleach} was 0.015 s^{-1} for 9.5 µm droplets and 0.029 s^{-1} for 6.0 µm droplets) were incorporated as an additional decay channel in the Michaelis–Menten formulae,

$$\frac{dP(t)}{dt} = \frac{V_{\max} S(t)}{K_{\text{M}} + S(t)} - k_{\text{bleach}} P(t),$$

and then integrated numerically with an ODE solver (MathCAD) using the values of K_M and V_{max} determined from the bulk Lineweaver–Burk plot to simulate the net bulk product concentration as a function of time from competition between product formation due to enzymatic catalysis and loss of fluorescence due to photobleaching. Figure 4.22(c) and (d) show that the effects of photobleaching in the droplets on the reaction rate are not sufficient to account for the measured decreases in reaction rate for droplets of either size.

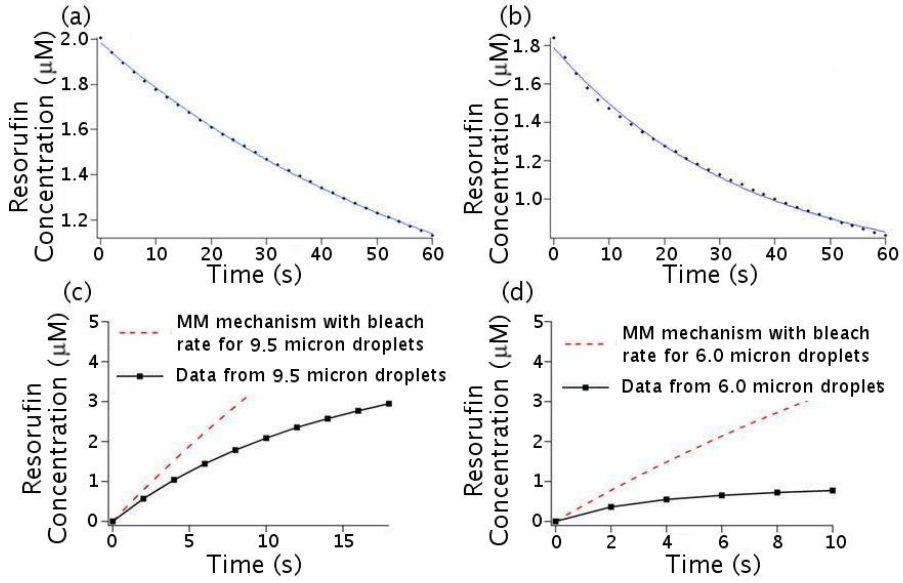

Figure 4.22. (a) and (b), Plots of fluorescence decay (dot) due to photobleaching in daughter droplets 9.5 μm (a) and 6.5 μm (b) in diameter were fitted with an exponential function (line) to get k_{bleach} reported in text; (c) and (d), Plots of simulated enzymatic reaction rates when first-order photobleaching decay constants were included in the bulk Michaelis–Menten mechanism, compared with data from the droplets.

Loss of ions at the interface

Additional controls were performed using confocal laser scanning microscopy of water-in-oil microemulsions with droplet sizes in the same range as those generated in the microfluidic devices. Figure 4.23 shows that inclusion of Magnesium Green dye indicated negligible loss of Mg^{2+} ions in the aqueous droplet interior due to sequestration by PEG groups at the interface [24], which would negatively affect enzyme activity. Similarly, SNARF-5F 5-(and-6)-carboxylic acid (pKa 7.2) and

resorufin (pKa 6.4) dyes indicated the pH did not change in the droplets from their values in the reaction buffer used to prepare the aqueous streams (pH = 7.2) due to loss of hydronium ions at the interface. 1 mg/ml aliquots of these indicators were stored in a −20 ℃ freezer or 4 ℃ cold room. Before use, these aliquots were thawed and diluted in reaction buffer (100 mM phosphate buffer with 1 mM $MgCl_2$, pH 7.2) to the appropriate concentration. 100 µL purified soybean oil was mixed and stirred with 50 µL buffer which contained the indicator dyes or fluorescent proteins.

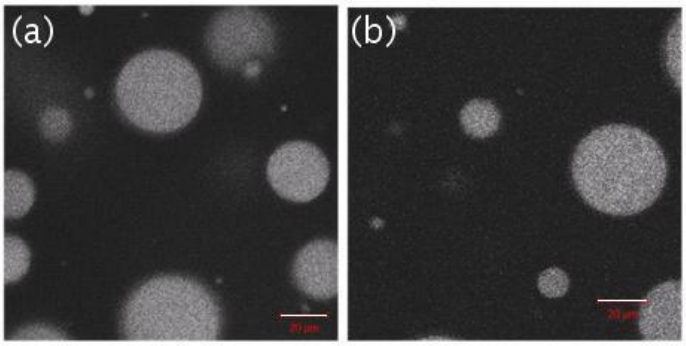

Figure 4.23. Fluorescent indicators used to visualize distribution of ions in water–oil microemulsions containing 0.1% (v/v) NP-PEG: (a) Magnesium Green; (b) SNARF-5F. Scale bar: 20 µm.

Correlation plots of enzyme kinetics, plug length and droplet diameter with backing pressure

Figure 4.24(a) is a plot of the average fluorescence intensity (background subtracted) versus inverse flow rate in the main channel due to the enzymatic production of resorufin in mother plugs, captured with the CCD camera just before a daughter droplet is splitting at the second T-junction. All experimental conditions, including the initial concentrations of enzyme and substrate, and the mixing and initiation of the reaction in the plugs, were the same as those used for the measurements of reaction rates in the daughter droplets described in the manuscript. The data can be grouped into three families classified by the average backing pressures applied at the aqueous inlets (approximately 20, 15, and 10 psi). Within each family, mother plugs and daughter droplets of different sizes were intentionally generated by fine tuning the backing pressure at the oil inlet relative to the fixed backing pressures used at the aqueous inlets. For example, in figure 4.24(a), the three data points

within the "10 psi" ellipse correspond to oil backing pressures of 11.3, 11.5, and 11.6 psi. Tuning the oil backing pressure relative to the fixed aqueous pressures within each family (ellipse) also changed the flow rates of plugs and daughter droplets.

The reciprocal of the flow velocity in figure 4.24(a) multiplied by the distance the plugs travelled from the inlet region to the focal point of the microscope in the main channel (2.3 mm) is simply the reaction time (mixing time) for the β-Gal-catalyzed hydrolysis of RGP substrate to give product (roughly 300 to 900 ms, depending on flow velocity). Figure 4.24(b) and (c) are plots of the correlations between flow velocity and average mother plug length in the main channel and average daughter droplet diameter in the side channel, respectively, determined from bright-field images. Importantly, these plots show that the full range of mother plug lengths (roughly 70 to 90 μm) and daughter droplet diameters (4 to 10 μm) were observed in *each* family (ellipse), which indicates that the size of the plugs and droplets was determined primarily by the minor differences in backing pressures applied at the oil inlet relative to the two aqueous inlets at steady state, and was relatively independent of the magnitude of the average value of the backing pressures. This observation has been reported before for water-in-oil droplets in microfluidic devices [160].

These correlations in turn indicate that the fluorescence increases in figure 4.24(a) were far more dependent on the reaction time in the plugs before they encountered the second T-junction (which depended on the flow velocity through the mixer) than on the sizes of plugs (or the resulting daughter droplets after splitting at the junction). Although we were not able to convert fluorescence intensity in figure 4.24(a) to absolute resorufin concentrations directly due to the low signal-to-background ratio from the rapidly moving plugs, the fluorescence increase with transit time should be linearly proportional to the initial enzymatic reaction rate in the plugs, assuming that none of the nominal population of enzymes in the plugs was inactivated. Figure 4.24(a) shows that this rate, in fact, was relatively insensitive to changes in plug length, whereas the reaction rate in the daughter droplets slowed down as a function of their size by as a much as a factor of 4 compared with the bulk rate, as was shown in figure 4.12. We consider this to be strong evidence that the loss of enzyme activity occurred predominately during droplet splitting from the plugs at the second T-junction in the

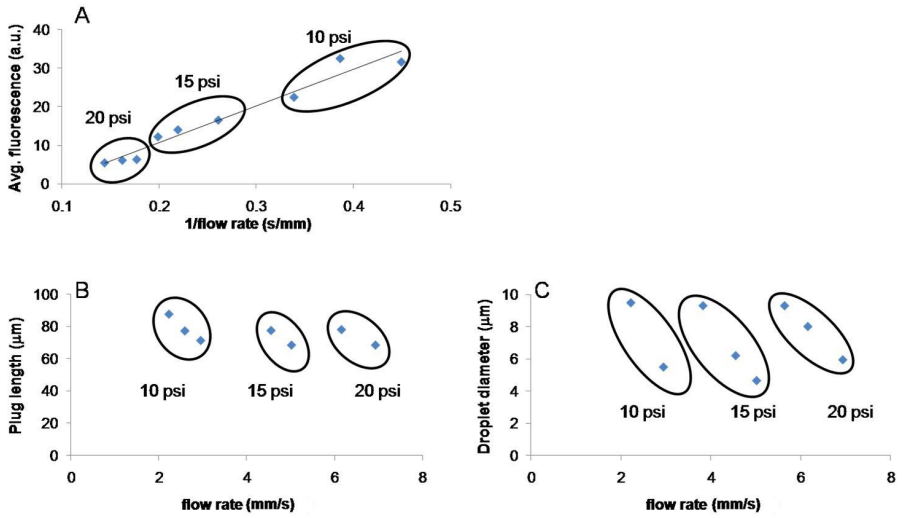

Figure 4.24. (a) Average fluorescence intensity versus inverse flow rate from mother plugs in the main channel measured just before the splitting of daughter droplets. The data are grouped into three families, classified in the figure by the average backing pressure applied at the aqueous inlets. Plug lengths (b) and droplet diameters (c) versus flow rate, using the same classification scheme as for (a). The full range of mother plug lengths and daughter droplet diameters were possible in each family of average backing pressure.

device, and not upstream.

Estimation of shear stress based on the geometry of deformed droplet

See Table 4.3.

Testing role of interface with inclusion of aqueous PEG 600 as crowding agent in droplets

An important prediction of our model is that the size dependence of the reaction rate decrease in femtoliter droplets would disappear, regardless of the strength of shear stress at the oil–water interface, if the interface could be completely passivated by a high enough concentration of NP-PEG surfactant. However, we could not test this prediction directly by increasing the amount of NP-PEG (or other surface active molecules, such as blocking proteins like BSA) because increased concentrations

Table 4.3. Determination of shear stresses for nascent daughter droplets at T-junction

Mean aqueous inlet pressure (psi)	Oil inlet pressure (psi)	Droplet diameter (μm)	Droplet image	$Ca \approx \frac{L-B}{L+B}$	Laplace pressure (kPa)	Shear stress (kPa)
9.9	11.4	9.3	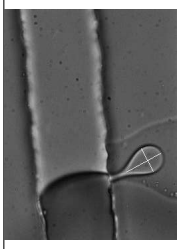	0.21	3.2	0.68
	11.7	5.2	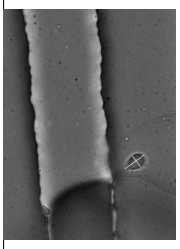	0.27	5.8	1.6
19.7	21.5	8.8	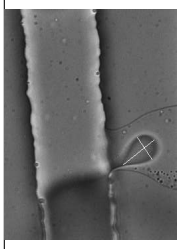	0.20	3.4	0.68
	22.0	5.7	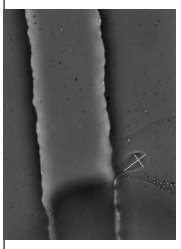	0.30	5.3	1.6

resulted in premature breakup of mother plugs at the device inlets, as described earlier. Instead, we used high concentrations (up to 100 mg/mL) of soluble polyethylene glycol 600 (PEG 600) in the aqueous phase as a crowding agent to help passivate the interface against nonspecific adsorption of β-Gal enzymes. Although PEG 600 is not surface active, at the high concentrations used, we expect

the interface would be occupied primarily by PEG 600 molecules due to excluded volume effects and reduced diffusion coefficients [174]. In addition, PEG 600 can form extended hydrogen-bonded networks with the NP-PEG surfactant molecules already present at the interface [167].

It is well known that molecular crowding affects reaction rates, however, these effects should depend primarily on the concentration of crowders in the aqueous environment, not on the size of the reaction vessel (droplet) itself, and should therefore be the same (within experimental uncertainty) for large and small droplets, as well as the bulk, as long as the concentration of crowders is the same [99, 121]. The inclusion of crowding agent thus serves as a test for the importance of the oil–water interface in the size-dependent kinetics we observed (in figure 4.12) by limiting the importance of enzyme adsorption at the interface in affecting reaction rates. We first tested the efficiency of the mixing stage of the device for mixing the more viscous solutions containing up to 100 mg/mL PEG 600 using Alexa568-β-Gal enzymes, and found the mixing efficiency to be comparable to that without the crowding agent included in the plugs.

Figure 4.25 shows that with crowding agent present, the reaction rates in the droplets were comparable to the bulk rate for all droplet sizes. All other experimental conditions were the same as for the data presented in figure 4.12. Although not attempting to characterize the mechanisms responsible for lowering enzyme activities with the addition of crowding agents, which have been the subject of many reports in the literature, here we note simply that the addition of the crowding agent has apparently masked the effects that the decrease in passivation at the interface with increasing S/V ratio of the droplets had on enzyme activity. Thus, this experiment serves as an additional control indicating that the decreases in initial enzymatic rates in femtoliter droplets with decreasing diameters seen in figure 4.12 (i.e., without crowding agent) were in fact due to progressive inactivation of enzymes resulting from nonspecific adsorption at the oil–water interface.

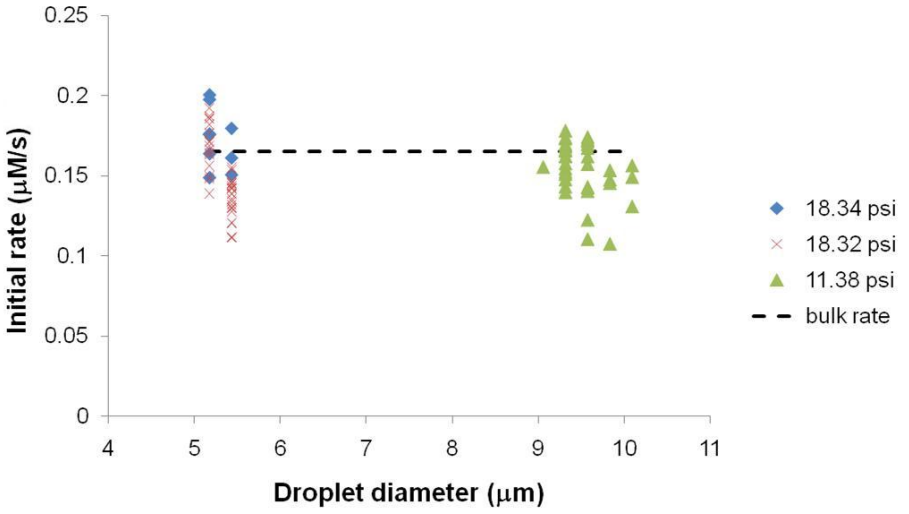

Figure 4.25. Initial enzyme reaction rate in large and small daughter droplets, and in the bulk, with inclusion of 100 mg/mL soluble PEG 600 as crowding agent at different backing pressures at the oil inlet.

Comparison of droplet kinetics with traditional assays for detecting nonspecific adsorption

Control of nonspecific interfacial enzyme adsorption in water–oil systems has been demonstrated from interfacial tension measurements with surfactant in the oil phase and proteins in the aqueous phase, and in nanoliter water-in-oil plugs in a microfluidic device by fluorescence microscopy and measurements of enzyme kinetics [114]. Nonspecific adsorption of β-Gal enzymes without the inclusion of NP-PEG surfactants at the interface was readily apparent from fluorescence images of labeled proteins in emulsion droplets and in mother plugs generated in our microfluidic device, and from interfacial tension measurements using the pendant drop technique. However, there was no evidence for nonspecific adsorption using either fluorescence or tensiometry when 0.1% (v/v) NP-PEG surfactant was included in the oil, even for enzyme concentrations up to two to three orders of magnitude greater than those used in the droplet experiments on chip (1.85 nM). Initial reaction rates for β-Gal in larger daughter drops formed in our device (9–10 μm diameter) were close to the average bulk rate. Our observation of minimal change in enzyme activity due to interfacial adsorption in mother plugs and the largest daughter droplets from the average bulk rate is consistent with

previous reports in the literature describing well-passivated aqueous–oil interfaces in microfluidic devices [114]. What, then, is different about the splitting-off process described in this paper for forming daughter droplets in the second T-junction from the more established assays for detecting nonspecific enzyme adsorption? How can we rationalize why the NP-PEG surfactant appears to passivate the oil–water interface adequately only for the larger size droplets and plugs?

First, for interfacial tension measurements using the pendant drop technique, drops were formed by slowly extruding aqueous solution into a quiescent oil phase, so there was little shear stress exerted on a growing drop due to the gradient of the flow field compared with the shear stress experienced by daughter droplets at the second T-junction in our microfluidic device.

Second, it is not possible to quantitatively compare the stresses present during the formation of the microemulsion droplets used in the laser scanning confocal images with the daughter droplets generated on chip. The emulsions were prepared by rapidly mixing buffer and oil in a micropipet tip, which likely involved turbulent conditions that were difficult to compare meaningfully with simple shear generated in the microfluidic device. However, assuming the same density of β-Gal enzymes in the aqueous interior as at the water–oil interface, on the basis of the homogeneous intensity profiles from laser scanning confocal images of emulsion droplets containing fluorescently labeled enzymes shown below, scaling the S/V ratio corresponding to decreasing daughter droplet diameters in our device results in a higher relative percentage of adsorbed enzymes, based purely on geometrical considerations (see below). This effect is inversely proportional to the cubic root of enzyme concentration in the drops, being ten times greater at nanomolar concentrations than at micromolar concentrations. The concentration of labeled β-Gal enzymes in the emulsion was 1.06 μM, whereas for the droplet experiments in the microfluidic device the enzyme concentration was 1.85 nM. Because of the inherent amplification involved with the use of fluorogenic substrates in enzymatic reactions, monitoring kinetics in droplets was a more sensitive way to detect enzyme adsorption than confocal images of emulsions containing labeled proteins.

Third, intensity profiles from epifluorescence images of Alexa568-β-Gal proteins in the daughter droplets generated on chip were homogeneous, with no evidence for interface adsorption, similar to the laser scanning confocal images of droplets in microemulsions. However, the decreased spatial

resolution and increased contributions to the measured intensity in those images from the greater excitation volume compared with laser scanning confocal microscopy lowers the sensitivity for detecting gradients in fluorescent enzyme density across the drop.

Interfacial tension measurements from pendant drops

For interfacial tension measurements, a contact angle goniometer (Ramé-Hart Instruments, Netcong, NJ) with micrometer syringe (Barnant, Barrington, IL) was coupled to a microscope-eyepiece digital camera (EM-500M, Big Catch, Torrance, CA) to capture the images of the pendant drops. All glassware and blunt-tip metal needles (Hamilton, Reno, NV) were cleaned in warm (45–50 ℃) RBS 35 detergent solution (Pierce, Rockford, IL) for two hours and rinsed with Millipore water thoroughly before drying at 80 ℃ overnight in an oven. Because the density of the aqueous solution was greater than that of soybean oil, aqueous pendant droplets were formed in the oil phase. A quartz cuvette (Hellma, Plainview, NY) containing 700 μL soybean oil, purified by passage through a fluorisil column, was placed on the 3-axis stage of the goniometer. The glass micrometer syringe, containing aqueous solution, with the luer-lock metal needle attached, was carefully lowered into the cuvette until the blunt tip of the needle was immersed a few millimeters into the oil. After focusing the camera on the tip of the needle, 2–4 μL aqueous solution from the syringe was carefully extruded into the oil phase to form a droplet at the needle tip. Images were captured at 10 s intervals starting immediately after the formation of the droplet. These images were processed with ImageJ software and fitted with an axisymmetric drop shape analysis program to get a numerical solution for the interfacial tension from the Young–Laplace equation [13]. For each set of conditions (e.g., varying the concentration of NP-PEG surfactant in the oil phase), three to five identical measurements were made in order to obtain reliable statistics. The effective aspect ratio and magnification of the imaging setup was calibrated by imaging a 0.125 inch steel ball bearing affixed to the end of a blunt metal needle with epoxy and immersed in the oil-filled cuvette. The interfacial tension of aqueous pendant drops in purified oil including NP-PEG surfactant at the concentration used in the microfluidic experiments (0.1% v/v) was 7.5 mN/m. As a check, the surface tension from a droplet of 18 MΩ water in air was determined to be 72.8 mN/m, which agreed with literature [83].

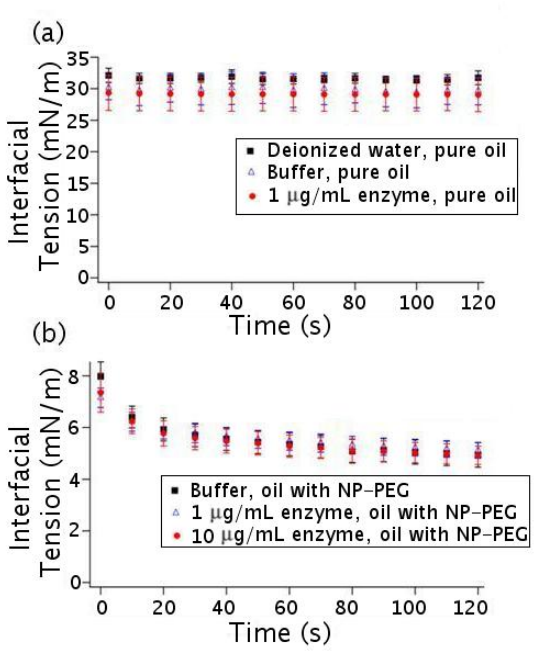

Figure 4.26. Interfacial tension (IFT) measurements from pendant aqueous drops suspended in oil phase. IFT data without (a) and with (b) 0.1% (v/v) NP-PEG surfactant included in the oil.

Figure 4.26(a) and (b) are plots of the interfacial tension (IFT) from microliter aqueous pendant drops suspended in the oil phase, with and without NP-PEG surfactant, respectively. Even in the absence of NP-PEG in the oil phase (figure 4.26(a)), differences in the IFT values due to protein adsorption could not be detected beyond the measurement uncertainty (standard deviation) for droplets containing 1.0 µg/mL β-Gal enzymes compared to droplets containing only reaction buffer. With 0.1% (v/v) NP-PEG included in the oil, the minimum protein concentration needed to detect a change in measured IFT was 100 µg/mL, two orders of magnitude greater than that used for the on-chip experiments.

Laser scanning confocal microscopy images of microemulsions

To study nonspecific adsorption of enzymes at the water–oil interface, β-Gal was labeled by Alexa Fluor 568 using the Protein Labeling Kit (Molecular Probes, Carlsbad, CA). Microemulsions were formed by mixing in a micropipet tip aqueous buffer containing labeled proteins with purified soybean oil containing 0.1% (v/v) NP-PEG surfactant. The emulsion was delivered to a # 0 glass coverslip and images were taken on an Axiovert 100 M inverted microscope, configured for confocal

laser scanning microscopy (LSM 5 PASCAL, Zeiss), and equipped with a Plan-Neofluar 63× objective lens (1.25 NA). The pinhole was set to 120 µm (2.0 Airy units), and detector gains were set at 800 V for both red and green channels. The images were recorded as 16-bit tiff files and processed using the Metamorph version 7.0r2 (Universal Imaging Corp, Downington, PA) and ImageJ software.

Figuer 4.27(a) and (b) are confocal images of 20 µm diameter droplets in water-in-oil microemulsions containing 570 µg/mL (1.06 µM) fluorescently labeled Alexa568-β-Gal enzymes, without (a) and with (b) the presence of 0.1% (v/v) NP-PEG surfactant in the oil phase. Because the images in figure 4.27 were from individual z-slices, we assumed that there were negligible contributions to the measured intensities from voxels that were out of the focal plane. The lack of discernible fluorescence contrast at the periphery of the droplet in figure 4.27(b) when NP-PEG surfactant is present indicates effective passivation of the interface with NP-PEG.

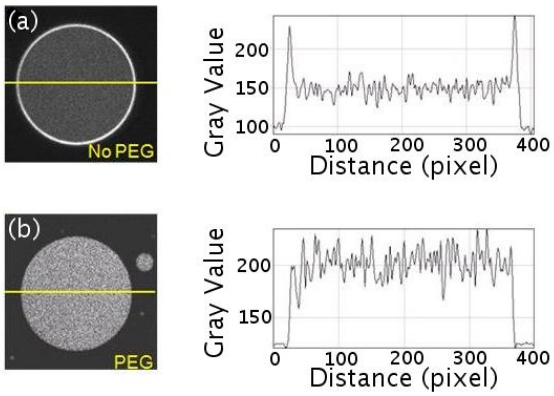

Figure 4.27. Laser scanning confocal fluorescence images of water–oil microemulsions containing 1.06 µM Alexa568-β-Gal enzymes without (a) and with (b) 0.1% (v/v) NP-PEG surfactant in the oil phase. Droplet diameters are 20 µm.

S/V scaling of enzyme densities in droplets

We used the confocal image of fluorescently labeled β-Gal enzymes in figure 4.27(b) as a starting point for estimating how increasing the S/V ratio in water-in-oil droplets would change the relative percentage of proteins nonspecifically adsorbed at an interface, assuming the density (mol/m^2) of enzymes at the interface and in the interior of the droplet remained equal. This assumption places an upper bound for the number of Alexa568-β-Gal enzymes that could be adsorbed at the interface

relative to that in the aqueous interior and still result in a uniform line profile of fluorescence intensity observed in figure 4.27(b). The concentration of Alexa568-β-Gal enzymes used was 1.06 μM, which translates to 6.02×10^{20} enzymes/m^3. The equivalent territorial volume per enzyme is the inverse of this number, 1.66×10^{-21} m^3/enzyme, with radius 73.5 nm. The corresponding territorial area per enzyme at the interface is 1.70×10^{-14} m^2/enzyme, which results in a molar surface density (Γ) at the interface of 9.80×10^{-11} mol/m^2. The number of enzymes at the interface in moles is this number multiplied by the surface area of the droplet (e.g., 4.19×10^{-10} m^2 for the 20 μm diameter droplet used in figure 4.27(b)). Thus, the maximum percentage of enzymes at the interface (4.10×10^{-20} moles) relative to the total (4.19×10^{-18} moles), was slightly less than 1% for the droplet shown in figure 4.27(b).

By simple scaling of these numbers with an increasing S/V ratio, the relative percentage of interface-bound enzymes increases. Figure 4.28(a) plots this relative percentage as a function of increasing S/V ratio for four different nominal enzyme concentrations (10^{-6} to 10^{-9} M). The lowest S/V ratio for figure 4.28(a) and (b) (10^5 m^2/m^3) corresponds to the 20 μm spherical drops imaged in figure 4.27, and roughly to the aqueous mother plugs in the main channel of the microfluidic device (30 μm width and height, with lengths varying from 70 to 90 μm, depending on flow rate). The highest value of the S/V ratio corresponds to 4 μm diameter daughter droplets generated on chip.

Increasing the S/V ratio by a factor of five results in increasing the relative percentage of interface-bound enzymes by a factor of five as well, for each concentration plotted in figure 4.28(a). However, a much higher proportion of the total enzyme population would be interface bound at nanomolar concentrations than at micromolar concentrations, for all S/V ratios. This is because the ratio of the number of interface molecules to the total number of molecules is equal to $\frac{Sc^{2/3}}{Vc} = \frac{S}{V}c^{-1/3}$, where S is the surface area of the interface, V is droplet volume, and c is concentration. Hence, the relative percentage of interface-bound enzymes increases by a factor of ten in going from micromolar to nanomolar concentrations. At nanomolar concentration, almost half of the total enzyme population for a 4.0 μm diameter droplet would be bound to the interface, when the enzymes in the interior and the interface are at the same density.

The top trace in figure 4.28(b) is an estimate of how the concentration of β-Gal enzymes remaining

in the aqueous interior of a daughter droplet, presumed to be the only enzymes that are catalytically active, decreases with increasing S/V ratio, assuming a nominal starting concentration of 1.85 nM (1 μg/mL). For comparison, the bottom trace is the effective concentration of active enzymes that would result in the initial rate data presented in figure 4.12(b), estimated by solving for $[E]_0$ from the Michaelis–Menten formulae,

$$[E]_0 \approx \left[\frac{K_\mathrm{M} + [S]_0}{[S]_0}\right] \frac{V}{k_\mathrm{cat}},$$

with $K_\mathrm{M} = 128.5$ μM and $k_\mathrm{cat} = 1341$ s^{-1}. V is the initial reaction rate data from figure 4.12(b), and the approximation $[S](t) \approx [S]_0 = 25$ μM should be valid at early times. Comparison of the two traces indicates that S/V scaling alone does not fully explain the 4-fold loss of enzyme activity in daughter droplets compared with the bulk initial rate. It does, however, offer a partial explanation for why the larger droplet in figure 4.27(b), with a higher concentration of labeled enzymes, was not as sensitive an assay for protein adsorption at the interface than the reaction rate data from the smaller daughter droplets generated by shear in the T-junction of the microfluidic device.

Epifluorescence images of daughter droplets containing labeled enzymes

Figure 4.29 shows that the fluorescence intensity profiles from Alexa568-β-Gal proteins in the daughter droplets were homogeneous, with no evidence for interface adsorption, similar to the laser scanning confocal image in figure 4.27(b). However, the decreased spatial resolution and increased contributions to the measured intensity in the image from the greater excitation volume with epi-fluorescence microscopy compared with laser scanning confocal microscopy lowers the sensitivity for detecting gradients in fluorescent enzyme density across the drop in figure 4.29.

Calculation of *p*-value using Student's *t* test in figure 4.12(b)

In figure 4.12(b), the reaction rate was fitted to a linear function of daughter droplet diameter using Matlab, and the p-value using Student's t test was obtained by the built-in Matlab function "regstat."

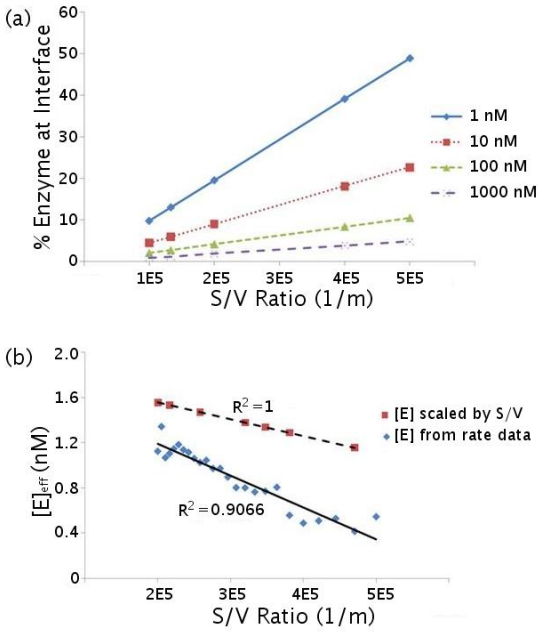

Figure 4.28. (a) Relative percentage of total enzyme population adsorbed at the interface, as a function of S/V ratio and concentration, assuming the same density of enzymes (mol/m^2) throughout droplet. (b) Effective concentrations of active enzymes left in aqueous interior of droplet after interface adsorption (1.85 nM nominal concentration), using S/V scaling (dashed line), and initial reaction rate data from figure 4.12 (solid line).

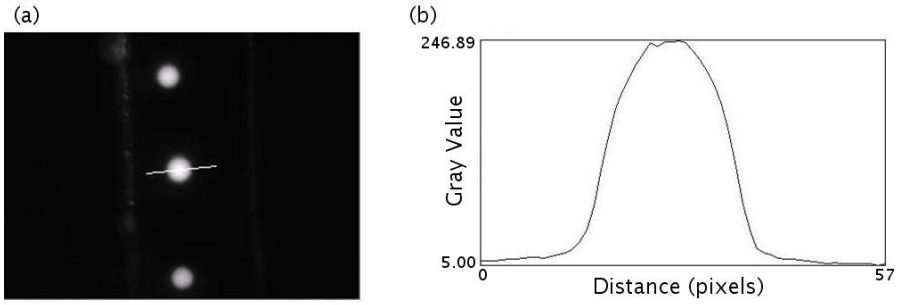

Figure 4.29. Epifluorescence microscope image (a) and line scan (b) of 5 µm daughter droplets containing 13 µg/mL Alexa568-β-Gal enzymes in the side channel.

Raw data for figure 4.12(b)

Raw data for figure 4.12(b) is available free of charge via the Internet at `http://pubs.acs.org`.

Chapter 5

Conclusion and Future Directions

This thesis analyzed the difference between traditional biochemical assays and real cellular environment, and identified three important differences: molecular crowding, low copy number, and spatial confinement. To reconcile these discrepancies, special treatment is needed in both theoretical and experimental works. On one hand, it is instructive to incorporate these features into the model of biochemical reaction networks to anticipate their influence. On the other hand, it is beneficial to be able to reconstruct the essential features of cellular systems in an in vitro study.

Chapter 2 discussed the implication of low copy number and spatial confinement using model systems. Both numerical and analytical approaches were employed. All the case studies in this chapter were motivated by realistic problems, and it would be interesting to directly test the predictions in experiments. Chapter 3 and 4 then described two microfluidic devices which may prove useful for this purpose. They enabled easy control of molecular crowding, copy number, and spatial confinement. As such, it is more biologically relevant to study the interaction among biomolecules using these devices. In addition, the devices reported here can be employed in the detection of biomolecules with less time consumption.

The experiments in chapter 4 also revealed the importance of shearing force in the redistribution of surfactant molecules and the resulting partial loss of interface protection. This in turn led to the inactivation of enzymes due to nonspecific adsorption to the interface. This influence was more significant when the droplet size was small because of higher shear stress applied as well as higher surface-to-volume ratio. Special attention is thus required to correctly interpret experimental observations in droplet-based microfluidic devices as their characteristic dimension is decreased. Future

work may involve direct recording of the transient process of surfactant convection and enzyme adsorption, and the quantitative analysis of the interaction among shear force, mass transport, and interfacial tension.

Bibliography

[1] B. Alberts. The cell as a collection of protein machines: Preparing the next generation of molecular biologists. *Cell*, 92:291–294, 1998.

[2] B. Alberts, A. Johnson, J. Lewis, M. Raff, K. Roberts, and P. Walter. *Molecular Biology of the Cell*. Garland Science: New York, 2007.

[3] S. S. Andrews. Serial rebinding of ligands to clustered receptors as exemplified by bacterial chemotaxis. *Phys. Biol.*, 2:111–122, 2005.

[4] S. S. Andrews and D. Bray. Stochastic simulation of chemical reactions with spatial resolution and single molecule detail. *Phys. Biol.*, 1:137–151, 2004.

[5] A. Arkin and J. Ross. Computational functions in biochemical reaction networks. *Biophys. J.*, 67:560–578, 1994.

[6] A. Arkin, J. Ross, and H. H. McAdams. Stochastic kinetic analysis of developmental pathway bifurcation in phage lamda-infected *Escherichia coli* cells. *Genetics*, 149:1633–1648, 1998.

[7] N. R. Beer, B. J. Hindson, E. K. Wheeler, S. B. Hall, K. A. Rose, I. M. Kennedy, and B. W. Colston. On-chip, real-time, single-copy polymerase chain reaction in picoliter droplets. *Anal. Chem.*, 79:8471–8475, 2007.

[8] B. P. Belousov. A periodic reaction and its mechanism. *Compil. Abstr. Radiat. Med.*, 147:145, 1959.

[9] D. Bensen and A. Scheeline. Reduction of dimension of a chemically realistic model for the peroxidase–oxidase oscillator. *J. Phys. Chem.*, 100:18911–18915, 1996.

[10] A. L. Borovinskiy and A. Y. Grosberg. Design of toy proteins capable of rearranging conformations in a mechnical fashion. *J. Chem. Phys.*, 118:5201–5212, 2003.

[11] T. V. Bronnikova, V. R. Fed'kina, W. M. Schaffer, and L. F. Olsen. Period-doubling bifurcations and chaos in a detailed model of the peroxidase–oxidase reaction. *J. Phys. Chem.*, 23: 9309–9312, 1995.

[12] T. V. Bronnikova, W. M. Schaffer, and L. F. Olsen. Nonlinear dynamics of the peroxidase–oxidase reaction: I. bistability and bursting oscillations at low enzyme concentrations. *J. Phys. Chem. B*, 105:310–321, 2001.

[13] L. Busoni, M. Carlà, and L. Lanzi. Algorithms for fast axisymmetric drop shape analysis measurements by a charge coupled device video camera and simulation procedure for test and evaluation. *Rev. Sci. Instrum.*, 72:2784–2791, 2001.

[14] V. Casagrande, Y. Togashi, and A. S. Mikhailov. Molecular synchronization waves in arrays of allosterically regulated enzymes. *Phys. Rev. Lett.*, 99:048301, 2007.

[15] D. Chiu, C. Wilson, A. Karlsson, A. Danielsson, A. Lundqvist, A. Stromberg, F. Ryttsen, M. Davidson, S. Nordholm, O. Orwar, and R. Zare. Manipulating the biochemical nanoenvironment around single molecules contained within vesicles. *Chem. Phys.*, 247:133–139, 1999.

[16] D. T. Chiu, C. F. Wilson, F. Ryttsén, A. Strömberg, C. Farre, A. Karlsson, S. Nordholm, A. Gaggar, B. P. Modi, A. Moscho, R. A. Garza-López, O. Orwar, and R. N. Zare. Chemical transformations in individual ultrasmall biomimetic containers. *Science*, 283:1892–1895, 1999.

[17] P. B. Chock and E. R. Stadtman. Superiority of interconvertible enzyme cascades in metabolic regulation: Analysis of multicyclic systems. *Proc. Natl. Acad. Sci. U.S.A.*, 74:2766–2770, 1977.

[18] H. P. Chou, M. A. Unger, and S. R. Quake. A microfabricated rotary pump. *Biomed. Microdevices*, 3:323–330, 2001.

[19] R. A. Copeland. *Enzymes: A Practical Introduction to Structure, Mechanism, and Data Analysis*. Wiley-VCH, 1996.

[20] V. Cristini and Y.-C. Tan. Theory and numerical simulation of droplet dynamics in complex flows—a review. *Lab Chip*, 4:257–264, 2004.

[21] M. De Menech. Modeling of droplet breakup in a microfluidic T-shaped junction with a phase-field model. *Phys. Rev. E*, 73:031505, 2006.

[22] M. De Menech, P. Garstecki, F. Jousse, and H. A. Stone. Transition from squeezing to dripping in a microfluidic T-shaped junction. *J. Fluid Mech.*, 595:141–161, 2008.

[23] A. J. deMello. Control and detection of chemical reactions in microfluidic systems. *Nature*, 442:394–402, 2006.

[24] V. Di Noto, S. Lavina, D. Longo, and M. Vidali. A novel electrolytic complex based on δ-$MgCl_2$ and poly(ethylene glycol) 400. *Electrochim. Acta*, 43:1225–1237, 1998.

[25] R. E. Dolmetsch, K. L. Xu, and R. S. Lewis. Calcium oscillations increase the efficiency and specificity of gene expression. *Nature*, 392:933–936, 1998.

[26] B. P. English, W. Min, A. M. van Oijen, K. T. Lee, G. B. Luo, H. Y. Sun, B. J. Cherayil, S. C. Kou, and X. S. Xie. Ever-fluctuating single enzyme molecules: Michaelis–Menten equation revisited. *Nat. Chem. Bio.*, 2:87–94, 2006.

[27] R. Erban and S. J. Chapman. Stochastic modelling of reaction–diffusion processes: Algorithms for biomolecular reactions, 2009. http://arxiv.org/abs/0903.1298v1.

[28] J. E. Ferrel Jr. and C.-Y. F. Huang. Ultrasensitivity in the mitogen-activated protein kinase cascade. *Proc. Natl. Acad. Sci. U.S.A.*, 93:10078–10083, 1988.

[29] J. E. Ferrell Jr. and E. M. Machleder. The biochemical basis of an all-or-none cell fate switch in *Xenopus* oocytes. *Science*, 280:895–898, 1998.

[30] K. Funakoshi, H. Suzuki, and S. Takeuchi. Formation of giant lipid vesiclelike compartments from a planar lipid membrane by a pulsed jet flow. *J. Am. Chem. Soc.*, 129:12608–12609, 2007.

[31] E. Fung, W. W. Wong, J. K. Suen, T. Bulter, S. G. Lee, and J. C. Liao. A synthetic gene-metabolic oscillator. *Nature*, 435:118–122, 2005.

[32] L. Gammaitoni, P. Hänggi, P. Jung, and F. Marchesoni. Stochastic resonance. *Rev. Mod. Phys.*, 70:223–287, 1998.

[33] F. Gao, E. Mei, M. Lim, and R. M. Hochstrasser. Probing lipid vesicles by bimolecular association and dissociation trajectories of single molecules. *J. Am. Chem. Soc.*, 128:4814–4822, 2006.

[34] A. G. Gaonkar and R. P. Borwankar. Adsorption behavior of monoglycerides at the vegetable oil/water interface. *J. Colloid Interface Sci.*, 146:525–532, 1991.

[35] J. Garcia-Ojalvo, M. B. Elowitz, and S. H. Strogatz. Modeling a synthetic multicellular clock: Repressilators coupled by quorum sensing. *Proc. Natl. Acad. Sci. U.S.A.*, 101:10955–10960, 2004.

[36] P. Garstecki, M. J. Fuerstman, H. A. Stone, and G. M. Whitesides. Formation of droplets and bubbles in a microfluidic T-junction—scaling and mechanism of break-up. *Lab Chip*, 6: 437–446, 2006.

[37] P. Gaspard. The correlation time of mesoscopic chemical clocks. *J. Chem. Phys.*, 117:8905–8916, 2002.

[38] P. Gaspard. Trace formula for noisy flows. *J. Stat. Phys.*, 106:57–96, 2002.

[39] D. Gillespie. The chemical Langevin equation. *J. Chem. Phys.*, 113:297–306, 2000.

[40] D. T. Gillespie. Exact stochastic simulation of coupled chemical reactions. *J. Phys. Chem.*, 81:2340–2361, 1977.

[41] D. T. Gillespie, S. Lampoudi, and L. R. Petzold. Effect of reactant size on discrete stochastic chemical kinetics. *J. Chem. Phys.*, 126, 2007.

[42] B. T. Ginn, B. Steinbock, M. Kahveci, and O. Steinbock. Microfluidic systems for the Belousov–Zhabotinsky reaction. *J. Phys. Chem. A*, 108:1325–1332, 2004.

[43] B. T. Ginn and O. Steinbock. Quantized spiral tip motion in excitable systems with periodic heterogeneities. *Phys. Rev. Lett.*, 93:158301, 2004.

[44] B. T. Ginn and O. Steinbock. Front aggregation in multiarmed excitation vortices. *Phys. Rev. E*, 72:046109, 2005.

[45] A. Goldbeter. *Biochemical Oscillations and Cellular Rhythms: The Molecular Bases of Periodic and Chaotic Behaviour*. Cambridge University Press: Cambridge, U.K., 1996.

[46] A. Goldbeter and D. E. Koshland Jr. An amplified sensitivity arising from covalent modification in biological systems. *Proc. Natl. Acad. Sci. U.S.A.*, 78:6840–6844, 1981.

[47] D. Gonze, J. Halloy, and P. Gaspard. Biochemical clocks and molecular noise: Theoretical study of robustness factors. *J. Chem. Phys.*, 116:10997–11010, 2002.

[48] H. H. Gorris and D. R. Walt. Mechanistic aspects of horseradish peroxidase elucidated through single-molecule studies. *J. Am. Chem. Soc.*, 131:6277–6282, 2009.

[49] H. Gruler and D. Müller-Enoch. Slaving the cytochrome P-450 dependent monooxygenase system by periodically applied light pulses. *Eur. Biophys. J.*, 19:217–219, 1991.

[50] W. Häberle, H. Gruler, P. Dutkowski, and D. Müller-Enoch. Light-induced activation and synchronization of the cytochrome P-450 dependent monooxygenase ystem. *Z. Naturforsch.*, 45:273–279, 1990.

[51] A. E. Hac, H. M. Seeger, M. Fidorra, and T. Heimburg. Diffusion in two-component lipid membranes—a fluorescence correlation spectroscopy and Monte Carlo simulation study. *Biophys. J.*, 88:317–333, 2005.

[52] S. E. Halford and J. F. Marko. How do site-specific DNA-binding proteins find their targets? *Nucleic Acids Res.*, 32:3040–3052, 2004.

[53] C. L. Hansen, S. Classen, J. M. Berger, and S. R. Quake. A microfluidic device for kinetic optimization of protein crystallization and in situ structure determination. *J. Am. Chem. Soc.*, 128:3142–3143, 2006.

[54] A. Hassibi, T. H. Lee, R. W. Davis, and N. Pourmand. Bioluminescence regenerative cycle (BRC) system for nucleic acid quantification assays. *Proc. SPIE*, 4966:65–75, 2003.

[55] J. Hattne, D. Fange, and J. Elf. Stochastic reaction–diffusion simulation with MesoRD. *Bioinformatics*, 21:2923–2924, 2005.

[56] M. J. B. Hauser, U. Kummer, A. Z. Larsen, and L. F. Olsen. Oscillatory dynamics protect enzymes and possibly cells against toxic substances. *Faraday Discuss.*, 120:215–227, 2001.

[57] B. Hess and A. Mikhailov. Self-organization in living cells. *Ber. Bunsenges. Phys. Chem.*, 98: 1198–1201, 1994.

[58] B. Hess and A. S. Mikhailov. Microscopic self-organization in living cells: A study of time matching. *J. Theor. Biol.*, 176:181–184, 1995.

[59] Z. H. Hou, T. J. Xiao, and H. W. Xin. Internal noise coherent resonance for mesoscopic chemical oscillatons: A fundamental study. *ChemPhysChem*, 7:1520–1524, 2006.

[60] Z. H. Hou and H. W. Xin. Internal noise stochastic resonance in a circadian clock system. *J. Chem. Phys.*, 119:11508–11512, 2003.

[61] Z. H. Hou and H. W. Xin. Optimal system size for mesoscopic chemical oscillation. *ChemPhysChem*, 5:407–410, 2004.

[62] Z. H. Hou, J. Q. Zhang, and H. W. Xin. Two system-size-resonance behaviors for calcium signaling: For optimal cell size and for optimal network size. *Phys. Rev. E*, 74:031901, 2006.

[63] T.-M. Hsin and E. S. Yeung. Single-molecule reactions in liposomes. *Angew. Chem. Int. Ed.*, 46:8032–8035, 2007.

[64] G. Hu, T. Ditzinger, C. Z. Ning, and H. Haken. Stochastic resonance without external periodic force. *Phys. Rev. Lett.*, 71:807–810, 1993.

[65] A. Huebner, M. Srisa-Art, D. Holt, C. Abell, F. Hollfelder, A. J. deMello, and J. B. Edel. Quantitative detection of protein expression in single cells using droplet microfluidics. *Chem. Commun.*, pages 1218–1220, 2007.

[66] D. Janasek, J. Franzke, and A. Manz. Scaling and the design of miniaturized chemical-analysis systems. *Nature*, 442:374–380, 2006.

[67] H. Jung, R. Kulkarni, and C. P. Collier. Dip-pen nanolithography of reactive alkoxysilanes on glass. *J. Am. Chem. Soc.*, 125:12096–12097, 2003.

[68] S.-Y. Jung, Y. Liu, and C. P. Collier. Fast mixing and reaction initiation control of single-enzyme kinetics in confined volumes. *Langmuir*, 24:4439–4442, 2008.

[69] A. Karlsson, R. Karlsson, M. Karlsson, A. S. Cans, A. Stromberg, F. Ryttsen, and O. O. Molecular engineering: Networks of nanotubes and containers. *Nature*, 409:150–152, 2001.

[70] A. Karlsson, K. Sott, M. Markström, M. Davidson, Z. Konkoli, and O. Orwar. Controlled initiation of enzymatic reactions in micrometer-sized biomimetic compartments. *J. Phys. Chem. B*, 2005:1609–1617, 2005.

[71] M. Karlsson, M. Davidson, R. Karlsson, A. Karlsson, J. Bergenholtz, Z. Konkoli, A. Jesorka, T. Lobovkina, J. Hurtig, M. Voinove, and O. Orwar. Biomimetic nanoscale reactors and networks. *Annu. Rev. Phys. Chem.*, 55:613–649, 2004.

[72] K. H. Kim, H. Qian, and H. M. Sauro. Sensitivity regulation based on noise propagation in stochastic reaction networks, 2008. http://arxiv.org/abs/0805.4455v2.

[73] I. Z. Kiss, Y. M. Zhai, and J. L. Hudson. Emerging coherence in a population of chemical oscillators. *Science*, 296:1676–1678, 2002.

[74] M. Kiss, L. Ortoleva-Donnelly, N. Beer, J. Warner, C. Bailey, B. Colston, J. Rothberg, D. Link, and J. Leamon. High-throughput quantitative polymerase chain reaction in picoliter droplets. *Anal. Chem.*, 2008.

[75] P. D. Koninck and H. Schulman. Sensitivity of CaM kinase II to the frequency of Ca^{2+} oscillations. *Science*, 279:227, 1998.

[76] R. Kopelman. Fractal reaction kinetics. *Science*, 241:1620–1626, 1988.

[77] M. Krishnan, D. T. Burke, and M. A. Burns. Polymerase chain reaction in high surface-to-volume ratio SiO_2 microstructures. *Anal. Chem.*, 76:6588–6593, 2004.

[78] E. V. Kuzmenkina, C. D. Heyes, and G. U. Nienhaus. Single-molecule FRET study of denaturant induced unfolding of RNase H. *J. Mol. Biol.*, 357:313–324, 2006.

[79] H. P. Lerch, A. S. Mikhailov, and B. Hess. Conformational-relaxation models of sigle-enzyme kinetics. *Proc. Natl. Acad. Sci. U.S.A.*, 99:15410–15415, 2002.

[80] H. P. Lerch, P. Stange, A. S. Mikhailov, and B. Hess. Mutual synchronization of molecular turnover cycles in allosteric enzymes III. Intramolecular cooperativity. *J. Phys. Chem. B*, 106: 3237–3247, 2002.

[81] M. J. Levene, J. Korlach, S. W. Turner, M. Foquet, H. G. Craighead, and W. W. Webb. Zero-mode waveguides for single-molecule analysis at high concentrations. *Science*, 299:682–686, 2003.

[82] A. Liau, R. Karnik, A. Majumdar, and J. H. D. Cate. Mixing crowded biological solutions in milliseconds. *Anal. Chem.*, 77:7618–7625, 2005.

[83] D. R. Lide, editor. *CRC Handbook of Chemistry and Physics*. CRC Press: Boca Raton, FL, 1998.

[84] D. R. Link, S. L. Anna, D. A. Weitz, and H. A. Stone. Geometrically mediated breakup of drops in microfluidic devices. *Phys. Rev. Lett.*, 92:054503, 2004.

[85] J. E. Lisman. A mechanism for memory storage insensitive to molecular turnover: A bistable autophosphorylating kinase. *Proc. Natl. Acad. Sci. U.S.A.*, 82:3055–3057, 1985.

[86] J. E. Lisman and M. A. Goldring. Feasibility of long-term storage of graded information by the Ca^{2+}/calmodulin-dependent protein kinase molecules of the postsynaptic density. *Proc. Natl. Acad. Sci. U.S.A.*, 85:5320–5324, 1988.

[87] R. M. Lorenz, J. S. Edgar, G. D. M. Jeffries, and D. T. Chiu. Microfluidic and optical systems

for the on-demand generation and manipulation of single femtoliter-volume aqueous droplets. *Anal. Chem.*, 78:6433–6439, 2006.

[88] H. P. Lu, L. Y. Xun, and X. S. Xie. Single-molecule enzymatic dynamics. *Science*, 282: 1877–1882, 1998.

[89] N. Maheshri and E. K. O'Shea. Living with noisy genes: How cells function reliably with inherent variability in gene expression. *Annu. Rev. Biophys. Biomol. Struct.*, 36:413–434, 2007.

[90] N. Manz, B. T. Ginn, and O. Steinbock. Meandering spiral waves in the 1,4-cyclohexanedione Belousov–Zhabotinsky system catalyzed by $Fe[batho(SO_3)_2]_3^{4-/3-}$. *J. Phys. Chem. A*, 107: 11008–11012, 2003.

[91] J. S. Marcus, W. F. Anderson, and S. R. Quake. Parallel picoliter RT-PCR assays using microfluidics. *Anal. Chem.*, 78:956–958, 2006.

[92] H. M. McConnell and M. Vrljic. Liquid-liquid immiscibility in membranes. *Annu. Rev. Biophys. Biomol. Struct.*, 32:469–492, 2003.

[93] J. Melin and S. R. Quake. Microfluidic large-scale integration: The evolution of design rules for biological automation. *Annu. Rev. Biophys. Biomol. Struct.*, 36:213–231, 2007.

[94] L. Ménétrier-Deremble and P. Tabeling. Droplet breakup in microfluidic junctions of arbitrary angles. *Phys. Rev. E*, 74:035303, 2006.

[95] Y. Meng, K. High, J. Antonello, M. W. Washabaugh, and Q. Zhao. Enhanced sensitivity and precision in an enzyme-linked immunosorbent assay with fluorogenic substrates compared with commonly used chromogenic substrates. *Anal. Biochem.*, 345:227–236, 2005.

[96] A. Mikhailov and B. Hess. Microscopic self-organization of enzymic reactions in small volumes. *J. Phys. Chem.*, 100:19059–19065, 1996.

[97] A. S. Mikhailov and D. H. Zanette. Mutual synchronization in ensembles of globally coupled neural networks. *Phys. Rev. E*, 58:872–875, 1998.

[98] A. S. Mikhailov, D. H. Zanette, Y. M. Zhai, I. Z. Kiss, and J. L. Hudson. Cooperative action of coherent groups in broadly heterogeneous populations of interacting chemical oscillators. *Proc. Natl. Acad. Sci. U.S.A.*, 101:10890–10894, 2004.

[99] A. P. Minton. The influence of macromolecular crowding and macromolecular confinement on biochemical reactions in physiological media. *J. Biol. Chem.*, 276:10577–10580, 2001.

[100] W. E. Moerner. New directions in single-molecule imaging and analysis. *Proc. Natl. Acad. Sci. U.S.A.*, 104:12596–12602, 2007.

[101] S. H. Northrup and H. P. Erickson. Kinetics of protein–protein association explained by Brownian dynamics computer simulation. *Proc. Natl. Acad. Sci. U.S.A.*, 89:3338–3342, 1992.

[102] W. Olbricht. Pore-scale prototypes of multiphase flow in porous media. *Annu. Rev. Fluid Mech.*, 28:187–213, 1996.

[103] L. F. Olsen. An enzyme reaction with a strange attractor. *Phys. Lett. A*, 94A:454–457, 1983.

[104] D. L. Olson, E. P. Williksen, and A. Scheeline. An experimentally based model of the peroxidase–NADH biochemical oscillator: An enzyme-mediated chemical switch. *J. Am. Chem. Soc.*, 117:2–15, 1995.

[105] J. Paulsson, O. G. Berg, and M. Ehrenberg. Stochastic focusing: Fluctuation-enhanced sensitivity of intracellular regulation. *Proc. Natl. Acad. Sci. U.S.A.*, 97:7148–7153, 2000.

[106] R. Phillips, J. Kondev, and J. Theriot. *Physical Biology of the Cell.* Garland Science: New York, 2008.

[107] W. H. Press, S. A. Teukolsky, W. T. Vetterling, and B. P. Flannery. *Numerical Recipes in C: The Art of Scientific Computing*, chapter 19, page 849. Cambridge University Press: Cambridge, U.K., 1992.

[108] J. Puchalka and A. M. Kierzek. Bridging the gap between stochastic and deterministic regimes in the kinetic simulations of the biochemical reaction networks. *Biophys. J.*, 86:1357–1372, 2004.

[109] S. Ramsey, D. Orrell, and H. Bolouri. Dizzy: Stochastic simulation of large-scale genetic regulatory networks. *J. Bioinform. Comput. Biol.*, 3:415–36, 2005.

[110] C. V. Rao, D. M. Wolf, and A. P. Arkin. Control, exploitation and tolerance of intracellular noise. *Nature*, 420:231–237, 2002.

[111] S. Redner. *A Guide to First-Passage Processes.* Cambridge University Press: Cambridge, U.K., 2001.

[112] D. M. Rissin and D. R. Walt. Digital concentration readout of single enzyme molecules using femtoliter arrays and Poisson statistics. *Nano Lett.*, 6:520–523, 2006.

[113] D. M. Rissin and D. R. Walt. Digital readout of target binding with attomole detection limits via enzyme amplification in femtoliter arrays. *J. Am. Chem. Soc.*, 4:6286–6287, 2006.

[114] L. S. Roach, H. Song, and R. F. Ismagilov. Controlling nonspecific protein adsorption in a plug-based microfluidic system by controlling interfacial chemistry using fluorous-phase surfactants. *Anal. Chem.*, 77:785–796, 2005.

[115] K. T. Rodolfa, A. Bruckbauer, D. Zhou, A. I. Schevchuk, Y. E. Korchev, and D. Klenerman. Nanoscale pipetting for controlled chemistry in small arrayed water droplets using a double-barrel pipet. *Nano Lett.*, 6:252–257, 2006.

[116] Y. Rondelez, G. Tresset, K. V. Tabata, H. Arata, H. Fujita, S. Takeuchi, and H. Noji. Microfabricated arrays of femtoliter chambers allow single molecule enzymology. *Nat. Biotechnol.*, 23:361–365, 2005.

[117] M. S. Samoilov and A. P. Arkin. Deviant effects in molecular reaction pathways. *Nat. Biotechnol.*, 24:1235–1240, 2006.

[118] M. A. Savageau. Michaelis–Menten mechanism reconsidered: Implications of fractal kinetics. *J. Theor. Biol.*, 176:115–124, 1995.

[119] W. M. Schaffer, T. V. Bronnikova, and L. F. Olsen. Nonlinear dynamics of the peroxidase–oxidase reaction. II. Compatibility of an extended model with previously reported model-data correspondences. *J. Phys. Chem. B*, 105:5331–5340, 2001.

[120] G. Schmid, I. Goychuk, and P. Hänggi. Stochastic resonance as a collective property of ion channel assemblies. *Europhys. Lett.*, 56:22–28, 2001.

[121] S. Schnell and T. E. Turner. Reaction kinetics in intracellular environments with macromolecular crowding: Simulations and rate laws. *Prog. Biophys. Mol. Bio.*, 85:235–260, 2004.

[122] G. Schreiber, G. Haran, and H.-X. Zhou. Fundamental aspects of protein-protein association kinetics. *Chem. Rev.*, 2009.

[123] E. Shacter, P. B. Chock, and E. R. Stadtman. Regulation through phosphorylation/dephosphorylation cascade systems. *J. Biol. Chem.*, 259:12252–12259, 1984.

[124] J.-U. Shim, G. Cristobal, D. R. Link, T. Thorsen, Y. Jia, K. Piattelli, and S. Fraden. Control and measurement of the phase behavior of aqueous solutions using microfluidics. *J. Am. Chem. Soc.*, 129:8825–8835, 2007.

[125] J. W. Shuai and P. Jung. Optimal intracelluar calcium signaling. *Phys. Rev. Lett.*, 88:068102, 2002.

[126] J. W. Shuai and P. Jung. Optimal ion channel clustering for intracellular calcium signaling. *Proc. Natl. Acad. Sci. U.S.A.*, 100:506–510, 2003.

[127] C. Simonnet and A. Groisman. Chaotic mixing in a steady flow in a microchannel. *Phys. Rev. Lett.*, 94:134501, 2005.

[128] H. Song, M. R. Bringer, J. D. Tice, C. J. Gerdts, and R. F. Ismagilov. Experimental test of scaling of mixing by chaotic advection in droplets moving through microfluidic channels. *Appl. Phys. Lett.*, 83:4664–4666, 2003.

[129] H. Song, D. L. Chen, and R. F. Ismagilov. Reactions in droplets in microfluidic channels. *Angew. Chem. Int. Ed.*, 45:7336–7356, 2006.

[130] H. Song and R. F. Ismagilov. Millisecond kinetics on a microfluidic chip using nanoliters of reagents. *J. Am. Chem. Soc.*, 125:14613–14619, 2003.

[131] K. Sott, T. Lobovkina, L. Lizana, M. Tokarz, B. Bauer, Z. Konkoli, and O. Orwar. Controlling enzymatic reactions by geometry in a biomimetic nanoscale network. *Nano Lett.*, 6:209–214, 2006.

[132] D. Sprinzak and M. B. Elowitz. Reconstruction of genetic circuits. *Nature*, 438:443–448, 2005.

[133] T. M. Squires and S. R. Quake. Microfluidics: Fluid physics at the nanoliter scale. *Rev. Mod. Phys.*, 77:977–1026, 2005.

[134] M. Srisa-Art, A. J. deMello, and J. B. Edel. High-throughput DNA droplet assays using picoliter reactor volumes. *Anal. Chem.*, 79:6682–6689, 2007.

[135] E. R. Stadtman and P. B. Chock. Superiority of interconvertible enzyme cascades in metabolic regulation: Analysis of monocyclic systems. *Proc. Natl. Acad. Sci. U.S.A.*, 74:2761–2765, 1977.

[136] P. Stange, A. Mikhailov, and B. Hess. Mutual synchronization of molecular turnover cycles in allosteric enzymes. *J. Phys. Chem. B*, 102:6273–6289, 1998.

[137] P. Stange, A. S. Mikhailov, and B. Hess. Mutual synchronizatin of molecular turnover cycles in allosteric enzymes II. Product inhibition. *J. Phys. Chem. B*, 103:6111–6120, 1999.

[138] P. Stange, A. S. Mikhailov, and B. Hess. Coherent intramolecular dynamics of enzymic reaction loops in small volumes. *J. Phys. Chem. B*, 104:1844–1853, 2000.

[139] P. Stange, D. Zanette, A. Mikhailov, and B. Hess. Self-organizing molecular networks. *Biophs. Chem.*, 72:73–85, 1998.

[140] J. R. Stiles and T. M. Bartol. *Computational Neuroscience: Realistic Modeling for Experimentalists*, chapter 4, pages 87–127. CRC Press: Boca Raton, FL, 2001.

[141] H. A. Stone. Dynamics of drop deformation and breakup in viscous fluids. *Annu. Rev. Fluid Mech.*, 26:65–102, 1994.

[142] H. A. Stone and L. G. Leal. The effects of surfactants on drop deformation and breakup. *J. Fluid Mech.*, 220:161–186, 1990.

[143] S. H. Strogatz. From Kuramoto to Crawford: Exploring the onset of synchronization in populations of coupled oscillators. *Physica D*, 143:1–20, 2000.

[144] A. D. Stroock, S. K. Dertinger, G. M. Whitesides, and A. Ajdari. Patterning flows using grooved surfaces. *Anal. Chem.*, 74:5306–5312, 2002.

[145] A. D. Stroock, S. K. W. Dertinger, A. Ajdari, I. Mezic, H. A. Stone, and G. M. Whitesides. Chaotic mixer for microchannels. *Science*, 295:647–651, 2002.

[146] A. P. Sudarsan and V. M. Ugza. Multivortex micromixing. *Proc. Natl. Acad. Sci. U.S.A.*, 103: 7228–7233, 2006.

[147] K. Sun and Q. Ouyang. Microscopic self-organization in networks. *Phys. Rev. E*, 64:026111, 2001.

[148] I. Szalai and E. Körös. The 1,4-cyclohexanedione–bromate–acid oscillatory system. 3. Detailed mechanism. *J. Phys. Chem. A.*, 102:6892–6897, 1998.

[149] I. Szalai, E. Körös, and L. Györgyi. 1,4-cyclohexanedione–bromate–acid oscillatory system. 4. Reduced models. *J. Phys. Chem. A*, 103:243–249, 1999.

[150] I. Szalai, K. Kurin-Csörgei, I. R. Epstein, and M. Orbán. Dynamics and mechanism of bromate oscillators with 1,4-cyclohexanedione. *J. Phys. Chem. A*, 107:10074–10081, 2003.

[151] I. Szalai, K. Kurin-Csörgei, and M. Orbán. Mechanistic studies on the bromate–1,4-cyclohexanedione–ferroin oscillatory system. *Phys. Chem. Chem. Phys.*, 4:1271–1275, 2002.

[152] S. Takeuchi, W. R. DiLuzio, D. B. Weibel, and G. M. Whitesides. Controlling the shape of filamentous cells of *Escherichia coli*. *Nano. Lett.*, 5:1819–1823, 2005.

[153] W. H. Tan and E. S. Yeung. Monitoring the reactions of single enzyme molecules and single metal ions. *Anal. Chem.*, 69:4242–4248, 1997.

[154] Y.-C. Tan, J. S. Fisher, A. I. Lee, V. Cristini, and A. P. Lee. Design of microfluidic channel geometries for the control of droplet volume, chemical concentration, and sorting. *Lab Chip*, 4:292–298, 2004.

[155] Y.-C. Tan, K. Hettiarachchi, M. Siu, Y.-R. Pan, and A. P. Lee. Controlled microfluidic encapsulation of cells, proteins, and microbeads in lipid vesicles. *J. Am. Chem. Soc.*, 128: 5656–5658, 2006.

[156] G. I. Taylor. The viscosity of a fluid containing small drops of another fluid. *Proc. R. Soc. London, Ser. A*, 138:41–48, 1932.

[157] G. I. Taylor. The formation of emulsions in definable fields of flow. *Proc. R. Soc. London, Ser. A*, 146:501–523, 1934.

[158] M. Thattai and A. van Oudenaarden. Attenuation of noise in ultrasensitive signaling cascades. *Biophys. J.*, 82:2943–2950, 2002.

[159] T. Thorsen, S. J. Maerkl, and S. R. Quake. Microfluidic large-scale integration. *Science*, 298: 580–584, 2002.

[160] T. Thorsen, R. W. Roberts, F. H. Arnold, and S. R. Quake. Dynamic pattern formation in a vesicle-generating microfluidic device. *Phys. Rev. Lett.*, 86:4163–4166, 2001.

[161] M. Tirrell and S. Middelman. Shear modification of enzyme kinetics. *Biotechnol. Bioeng.*, 17: 299–303, 1975.

[162] M. Tirrell and S. Middleman. Shear deformation effects in enzyme catalysis. Metal ion effect in the shear inactivation of urease. *Biophys. J.*, 23:121–128, 1978.

[163] T. M. Tsai and M. J. Miksis. Dynamics of a drop in a constricted capillary tube. *J. Fluid Mech.*, 274:197–217, 1994.

[164] M. A. Unger, H. P. Chou, T. Thorsen, A. Scherer, and S. R. Quake. Monolithic microfabricated valves and pumps by multilayer soft lithography. *Science*, 288:113–116, 2000.

[165] P. P. Valkó and J. Abate. Comparison of sequence accelerators for the Gaver method of numerical Laplace transform inversion. *Comput. Math. Appl.*, 48:629–636, 2004.

[166] N. G. Van Kampen. *Stochastic Processes in Physics and Chemistry*. North Holland: Amsterdam, 2007.

[167] A. Vergara, L. Paduano, G. D'Errico, and R. Sartorio. Network formation in polyethyleneglycol solutions. An intradiffusion study. *Phys. Chem. Chem. Phys.*, 1:4875–4879, 1999.

[168] H. L. Wang, Q. Ouyang, and Y. A. Lei. Microscopic self-organization in biochemical reactions: A lattice model. *J. Phys. Chem. B*, 105:7099–7103, 2001.

[169] K. Wang, Y. C. Lu, J. H. Xu, and G. S. Luo. Determination of dynamic interfacial tension and its effect on droplet formation in the T-shaped microdispersion process. *Langmuir*, 25: 2153–2158, 2009.

[170] M. Yamada, S. Doi, H. Maenaka, M. Yasuda, and M. Seki. Hydrodynamic control of droplet division in bifurcating microchannel and its application to particle synthesis. *J. Colloid Interface Sci.*, 321:401–407, 2008.

[171] J. Q. Zhang, Z. H. Hou, and H. W. Xin. System-size biresonance for intracellular calcium signaling. *ChemPhysChem*, 5:1041–1045, 2004.

[172] B. Zhao and J. C. Wang. Stirring-controlled bifurcations in the 1,4-cyclohexanedione–bromate reaction. *J. Phys. Chem. A*, 109:3647–3651, 2005.

[173] B. Zheng, J. D. Tice, and R. F. Ismagilov. Formation of droplets of alternating composition in microfluidic channels and applications to indexing of concentrations in droplet-based assays. *Anal. Chem.*, 76:4977–4982, 2004.

[174] H.-X. Zhou, G. Rivas, and A. P. Minton. Macromolecular crowding and confinement: Biochemical, biophysical, and potential physiological consequences. *Annu. Rev. Biophys.*, 37: 375–397, 2008.